NANOSCALE PATTERNING OF LIQUID CRYSTAL-AQUEOUS INTERFACES

A THESIS SUBMITTED TO
THE GRADUATE SCHOOL OF NATURAL AND APPLIED SCIENCES
OF
MIDDLE EAST TECHNICAL UNIVERSITY

BY

ALİ AKMAN

IN PARTIAL FULFILLMENT OF THE REQUIREMENTS
FOR
THE DEGREE OF MASTER OF SCIENCE
IN
CHEMICAL ENGINEERING

JUNE 2023

Approval of the thesis:

NANOSCALE PATTERNING OF LIQUID CRYSTAL-AQUEOUS INTERFACE

submitted by **ALİ AKMAN** in partial fulfillment of the requirements for the degree of **Master of Science** i**n Chemical Engineering, Middle East Technical University** by,

Prof. Dr. Halil Kalıpçılar
Dean, Graduate School of **Natural and Applied Sciences** _____

Prof. Dr. Pınar Çalık
Head of the Department, **Chemical Engineering** _____

Assoc. Prof. Dr. Emre Büküşoğlu
Supervisor, **Chemical Engineering, METU** _____

Examining Committee Members:

Prof. Dr. Deniz Üner
Chemical Engineering, METU _____

Assoc. Prof. Dr. Emre Büküşoğlu
Chemical Engineering, METU _____

Prof. Dr. Nihal Aydoğan
Chemical Engineering, Hacettepe University _____

Assoc. Prof. Dr. Simge Çınar Aygün
Metallurgical and Materials Eng., METU _____

Assist. Prof. Dr. Necip Berker Üner
Chemical Engineering., METU _____

Date: 13.06.2023

I hereby declare that all information in this document has been obtained and presented in accordance with academic rules and ethical conduct. I also declare that, as required by these rules and conduct, I have fully cited and referenced all material and results that are not original to this work.

Name Last name : Ali Akman

Signature :

ABSTRACT

NANOSCALE PATTERNING OF LIQUID CRYSTAL-AQUEOUS INTERFACES

Akman Ali
Master of Science, Chemical Engineering
Supervisor : Assoc. Prof. Dr. Emre Büküşoğlu

June 2023, 110 pages

Assembled colloidal structures have gained significant interest in scientific and technological advances. We experimentally investigated the self-assembly of the colloids at fluidic interfaces that mediate elastic interactions. Whereas past studies have reported the assembly of the micrometer- or molecular-sized species at aqueous interfaces of liquid crystals (LCs), herein we study the assembly of the intermediate-sized nanoparticles. Specifically, the surface-modified silica nanoparticles (50 to 500 nm-sized) were adsorbed at LC-water interfaces (either nematic or cholesteric droplets with a range of configurations) and their positioning was investigated using electron microscopy after polymerization of the LCs. Experiments and modeling of the interparticle interactions revealed that the electric double-layer forces and the elastic forces caused by LC strain are dominant in the assembly and their contributions can be tuned to direct the self-assembly of the nanoparticles to maintain textures patterned by the sub-interface symmetry of confined cholesteric LCs. At high ionic strengths, we observed a strong localization at the defects, whereas intermediate ionic strengths resulted in a partial enrichment of the nanoparticles into cholesteric fingerprint patterns with interaction energy estimated as $\approx 3\ k_B T$. This result was comparable with the calculations based on the strength of the binary

interactions of the nanoparticles. The findings also support the role of ion partitioning at the LC-aqueous interfaces on the formation of the assemblies. The experimental findings on the formation of rich assemblies of nanoparticles with elastic interactions can be utilized for applications in sensors, microelectronics, and photonic devices.

Keywords: Liquid crystals, cholesterics, nanoparticle assembly, patterning, elasticity

ÖZ

SIVI KRİSTAL-SU ARAYÜZÜNÜN NANO ÖLÇEKTE ÖRÜNTÜLENMESİ

Akman,Ali
Yüksek Lisans, Kimya Mühendisliği
Tez Yöneticisi: Doç. Dr. Emre Büküşoğlu

Haziran 2023, 110 sayfa

Kendiliğinden toplanan koloid yapılar geçtiğimiz senelerde bilimsel ve teknolojik gelişmelerde büyük ilgi topladı. Çalışmamızda akışkan arayüzlerde elastik etkileşimlerden doalyı ortaya çıkan nanoparçacık kendiliğinden toplanma davranışları deneysel olarak incelenmiştir. Daha önceki çalışmalar, micrometre ya da moleküler boyutlardaki yapıların sıvı kristal arayüzlerindeki kendiliğinden toplanma davranışlarını incelese de, bu çalışmada ara boyut nanometre seviyesindeki parçacıkların etkileşimleri incelenmiştir.50-500 nm arası boyutlara sahip olan yüzeyleri fonksiyonlanmış silika nanoparçacıkları, sıvıkristal arayüzeyine adsorplandı ve sıvıkristale karıştırılmış reaktif mezojenlerin polirmerleştirilmesi sonrası nanoparçacıkların pozisyonları elektron mikroskopu ile incelendi. Deneysel ve modelleme sonucu elde edilen sonuçlar ışığında anlaşıldı ki bu boyut aralıklarında nanoparçacıkların elektrik çift katmanı sonucu oluşan elektrostatik etkileşimler, ve sıvı kristal üzerinde oluşan deformasyon sonucu ortaya çıkan elastik etkileşimler kendiliğinden toplanma prosesindeki dominant kuvvetlerdir ve bu kuvvetlerin modifikasyonu ile nanoparçacıklar hapsedilmiş kolesterik sıvı kristallerin arayüz altı simetrileri üzerinde kendiliğinden toplanma için yönlendirilebilir. Yüksek iyonik kuvvetli ortamlarda nanoparçacıkların sıvı kristal kusurlarında kuvvetli bir şekilde

lokalize olduğu gözlemlenirken, orta seviye iyonik kuvvetlerde nanoparçacıkların kolesterik parmakizi desenlerini kısmi olarak doldurduğu gözlemlendi. Gözlemler sonucu parçacıklar arası etkileşim enerjisinin ≈3 $k_B T$ olduğu hesaplanırken, bu enerji değerinin parçacıklar arası ikili etkileşimler üzerinden yapılan modelden elde edilen sonuca yakın olduğu görüldü. Sonuçlar aynı zamanda nanoparçacıklar arası etkileşimlerde sıvı kristal-su ara yüzünde gözlemlenen iyon ayrılması olayının etkisinin rolünü de desteklemektedir. Bu çalışmada yapılan nanoparçacıkların sıvı kristal-su ara yüzündeki elastik etkileşimler sonucu kendiliğinden toplanma olayı üzerindeki sonuçlarının mikro elektronik, sensor ve fotonik alanlarında kullanılabilir.

Anahtar Kelimeler: Sıvı Kristal, Kolesterik, Nanoparçacık Toplanması, Örüntüleme, Elastisite

ACKNOWLEDGMENTS

I would like to begin by expressing my heartfelt appreciation to my esteemed advisor, Assoc. Prof. Dr. Emre Büküşoğlu, whose unwavering support, invaluable guidance, and immense patience have been instrumental throughout the course of this study. In the initial stages of my academic journey, Dr. Büküşoğlu emerged as a profoundly influential figure, assuming a pivotal role in shaping my development. His mentorship extended far beyond the confines of scholarly pursuits, encompassing a holistic approach to life itself. From our very first encounter, I was met with undivided attention and unwavering encouragement, fostering an environment in which my aspirations could thrive. Moreover, Dr. Büküşoğlu instilled within me the crucial essence of academic rigor and unyielding discipline. While acknowledging that there is much more for me to learn, I firmly believe that the knowledge and wisdom acquired over the past three years under his tutelage have not only transformed me into a more proficient researcher but have also contributed significantly to my personal growth. The privilege of working alongside him has been an extraordinary experience, etched indelibly in my memory. I am equally indebted to Prof. Dr. Deniz Üner for her invaluable guidance, extending far beyond the confines of academia and permeating the very fabric of my existence. Throughout my career, Prof. Dr. Üner has been one of the few individuals capable of truly comprehending the depths of my being, at times surpassing my own self-awareness. She possesses an innate ability to discern my strengths and weaknesses, unfailingly providing unwavering support as I navigate through them. Engaging in conversations and discussions with her has been profoundly fulfilling, allowing for both intellectual growth and sheer enjoyment. One conversation in particular, held at the outset of my Master's Degree, remains etched in my memory, and I wish to express my heartfelt gratitude once again for her belief in me during that critical period. Without her profound influence, I would not be the person I am today.

Furthermore, I extend my deepest appreciation to the members of the Soft and Functional Materials Laboratory Group: Özge Batır, Aslı Karausta, Elif Kurt, Elif Erçelik, R. Umut Dinç, Selin Şengül, Ceren Kocaman, Dr. Pınar Beyazkılıç Ayas, Dr. Selda Sezer, Gülce İlhan, Ayşe Nurcan Özşahin, each of whom holds a special place in my heart. Foremost among them, I wish to express my profound gratitude to Özge Batır, whose immeasurable impact on the bonds of friendship within our group is irrefutable. Merely stating that she has been a remarkable friend would fall short of capturing her true essence. May the unbreakable bond we share endure throughout our lives, and I extend my heartfelt thanks for standing by me during both triumphs and tribulations. I will forever cherish the long nights and weekends spent in the laboratory with Aslı, whose presence brought true pleasure to my time there. Thank you for being by my side, quite literally, and for infusing the laboratory experience with a sense of joy and camaraderie. I will sincerely miss our infectious laughter. My gratitude also extends to my long-standing friend in the department, Elif Kurt, whose presence facilitated my seamless integration into our circle of friends. Even in the darkest of days, you consistently brightened my life, and I will miss the simple act of knocking on your door just to see your face. I express my heartfelt appreciation to Elif Erçelik for embodying the true essence of friendship, an unwavering source of reliability upon whom I could always depend. I could not have endured without you. I extend my gratitude to Umut Dinç, not only for being a remarkable friend but also for serving as an exemplar worthy of admiration. I have gleaned invaluable lessons from your wisdom. Furthermore, I would like to express my gratitude to Ceren Kocaman for serving as an inspirational figure in my life. You are not only a dear friend but also a profoundly accomplished individual. I extend my deepest thanks to Selin for being an exceptional teacher, enabling me to learn and embrace my research with unwavering passion. Through your patient and nurturing demeanor, I swiftly embraced and developed an affinity for my research topic. I am grateful to Gülce İlhan for her unwavering honesty, a virtue I consider among the most essential qualities a person can possess. Although our time together in the laboratory was brief, I could discern your exceptional character, and I firmly

believe that you will accomplish great feats in the future. I want to take a moment to express my heartfelt gratitude to Nurcan, who has been the dearest student and an amazing friend. Your unwavering compassion and kindness have touched me deeply. Even though our time together was unfortunately short, it felt like we had known each other forever. I truly regret not having more moments to share and deepen our friendship. You have become an irreplaceable part of my life, and I am forever grateful for the joy and warmth you bring. Thank you for being such a wonderful presence in my journey. My appreciation extends to our esteemed post-doctoral researchers, Pınar and Selda. Your mentorship and warm-hearted nature have imparted invaluable wisdom, significantly enriching my academic journey. Lastly, I must express my heartfelt thanks to Enes Akyıldız. We embarked upon this journey together, surmounting numerous obstacles along the way, and you have consistently provided unwavering support. As we now approach the culmination of this shared voyage and prepare to embark on a new chapter together on the other side of the world, I am deeply grateful for your enduring presence.

I reserve my utmost appreciation for my family, whose unwavering patience, support, understanding, and trust have been unwavering throughout my educational journey. To Cem, Aliye, and Zeynep, I extend my deepest thanks for being a constant presence in my life, standing steadfastly by my side. The people I've met during my nine-year journey at METU have made it the most incredible period of my life. It's difficult to express just how much I'll miss this place. The experiences, friendships, and personal growth I've gained here have shaped me profoundly. Leaving behind this vibrant and nurturing environment fills me with gratitude, appreciation, and a tinge of sadness. As I move forward, I carry with me the immeasurable impact and cherished connections from my time at METU.

This work was supported by the Scientific and Technological Council of Turkey (TÜBİTAK) under award number 219M068.

To my Family

TABLE OF CONTENTS

LIST OF TABLES

TABLES

LIST OF FIGURES

FIGURES

CHAPTER 1

INTRODUCTION

Assembled structures of the colloidal size-ranged species have gained significant value in scientific and technological advancements. Most recent examples of applications involving such structures include sensors[1], photonics[2], and electronics[3] among others[4–6]. Although much demanded, the ability to control the structuring of the colloids, especially in two-dimensional geometries, remains a significant challenge because it requires a clear identification of the governing interactions between species for controlled assembly and significant establishment of the influence of the nanoscopic environments on such interactions of the colloids. Employment of the fluid-fluid interfaces to facilitate the interaction of the colloidal species has gathered critical interest for such purposes as they offer species exchange with the interfaces and the bulk, and a soft and deformable medium that provides significant mobility for rapid reorganization towards targeted assemblies.[7–9]

A fluidic medium that adds significant flexibility in controlling the colloidal assemblies is the liquid crystals (LCs). LCs are complex fluidic phases of matter that are stable between crystalline solids and isotropic liquids which are characterized by the long-range ordering of their constituent molecules (**Figure 1. 1**).[10] Because of their unique elastic and optical properties, LCs are heavily used in sensors[11–14] or optics[15–17] applications whereas past studies investigate their potential in directing colloidal self-assembly.[18–31] The main advantages of the use of LCs in such applications can be considered as the three additional key concepts compared to their isotropic counterparts, namely the surface anchoring (surface alignment that arises from the interactions of mesogens with the contacting surfaces), elasticity (arises from the long-range ordering) and the formation of the topological defects (local disorders due to the interplay of the elasticity and surface anchoring).[10,18] Thus, the

interfaces of LCs carry significant potential in the directed assembly of the colloidal species as they combine such additional properties of the LCs and the advantages of the fluidic interfaces.

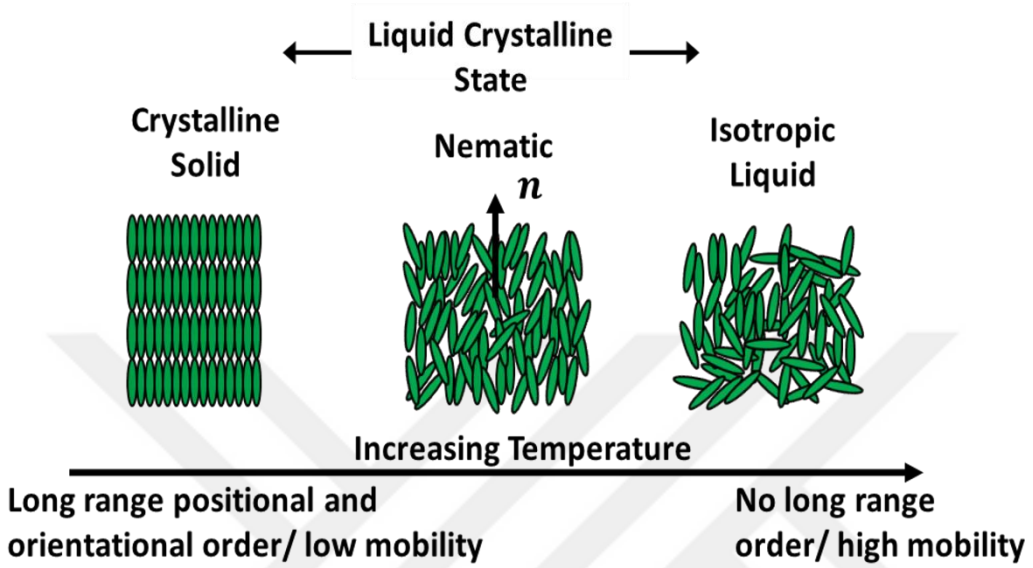

Figure 1. 1 a) Schematic representation of phase behavior of temperature-dependent (thermotropic) liquid crystals. b) Molecular structure of 4-cyano-4'-pentylbiphenyl (5CB).

The surface anchoring is the surface-induced ordering of the LC mesogens due to the interactions between the LC mesogens and the molecules of the medium confining the LC. The term easy axis is the orientation of the LC director (the average orientation of LC mesogens) when no external energy field is present. In the presence of an energy field, the director of the LC deviates from the easy axis and the free energy at the surface increases depending on the orientation of the LC. The change in the free energy is given as:[10]

$$F_s = F_0 + \frac{1}{2} W_a \sin^2(\theta_s - \theta_e)$$

In this equation θ_s and θ_e represent the angles of the surface director and the easy axis respectively, W_a is the anchoring energy which is usually in the range of 10^{-3} – 10^{-2} mJ/m^2, F_0 is the interfacial free energy corresponding to the easy axis and F_s is the free energy at the interface(**Figure 1. 2 a**).

The elastic properties of the LCs are a result of the long-range orientational ordering of the LC mesogens. Due to these elastic properties, three modes of strain arise in LCs, though not all the modes of strain can occur in all LCs. These three modes of strain are the so-called twist, bend, and splay modes. The strains are described by the Frank-Oseen equation for the free density:[10]

$$F_e = \frac{1}{2} K_1 \left(\nabla . \underline{n}\right)^2 + \frac{1}{2} K_2 \left(\nabla . \underline{n} \times \underline{n}\right)^2 + \frac{1}{2} K_3 \left(\underline{n} \times (\nabla \times \underline{n})\right)^2$$

Where the K_1, K_2, and K_3 are the splay, bend, and twist elastic constants respectively, and are in the order of 10^{-11} N (**Figure 1. 2b**).

Topological defects of the LC arise when LC is confined to a finite geometry. In this case, LC cannot preserve its surface-induced orientation through a continuous strain and locally melt at the regions of LC where the strain is high enough. Even though they macroscopically correspond to singularities in the long-range ordering of the LCs, under closer look, the cores of the defects are nanoscale regions of LC without orientational ordering(**Figure 1. 2c)**. The energy required for the formation of defects is given as:[10]

$$F_d = \int f_d dV_d \sim \frac{4}{3} \pi r_d^3 \epsilon_d$$

ϵ_d is the free energy density associated with the local melting of the nematic phase, r_d is the estimated radius of the defect core which is approximately 5 nm. Since the defect occurs when it is energetically more favorable to locally melt instead of keeping the local orientation, the size of the defect core can be estimated to the ratio

between, the elastic constant of the LC (K) to the free energy density as: $r_d = \sqrt{\frac{K}{\epsilon_d}}$.[10]

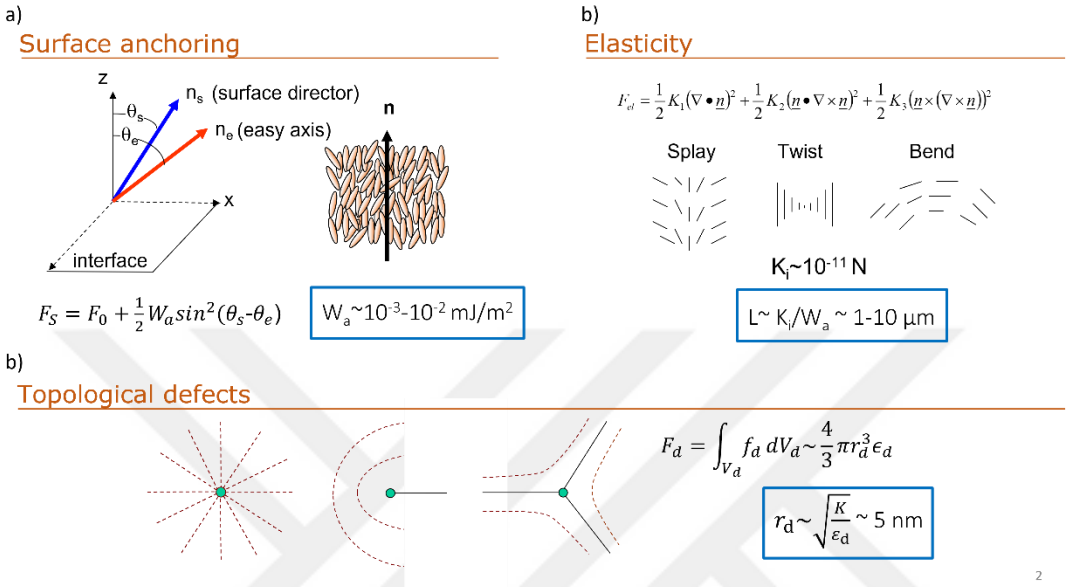

Figure 1. 2 Schematic illustrations of liquid crystal key concepts a) Surface ordering (Anchoring) and LC director. b) Liquid Crystal elasticity and three modes of elastic strain. c) Topological defects and example defect structures.

Cholesteric LCs (CLCs) are the phases where the helical twist orthogonal to the director of the individual mesogens is present (**Figure 1. 3**). The length of the twist to complete a 2π turn is called the pitch length. Introducing a boundary condition to CLCs gives rise to useful structures. Especially, when confined into spherical emulsion droplets, CLCs form multiple unique droplet structures with well-defined internal director profiles and line defects (disclinations).[32–42] Past studies have shown that the ratio of the droplet diameter to half of the pitch length (called the chiral confinement coefficient, *N*) is an important parameter determining the probability distribution of the droplet structures. For the CLC droplets with planar anchoring, three structures are more stable compared to the others depending on *N*, and such structures are characterized by their bulk configurations and the positioning of the

point defects at their aqueous interfaces.[32,33] The distribution of micrometer-sized colloids on planar CLC droplets done previously showed localization of the colloids at such point defects of the droplets.[33,34] Recent studies showed that the number of possible configurations increases remarkably for the droplets with homeotropic anchoring.[35–42] Among these structures are the ones that possess sub-interface line disclinations called the Periodic Loop (PLS) and Concentric Loop Structures (CLS) that carry a significant potential in the formation of the controlled interfacial colloidal assemblies. As the disclinations are close to the interfaces and carry excess elastic free energy density due to the significant straining of the director profiles, they provide a "heterogenous energy landscape" at the droplet interfaces that are potentially useful for directing the interfacial self-assembly of nanoscopic species.[43–45]

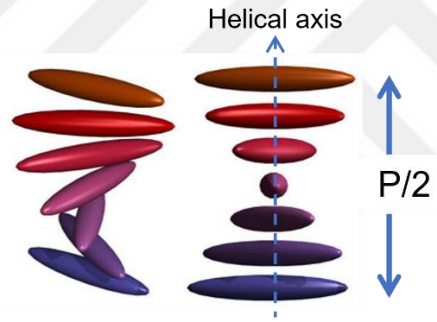

Figure 1. 3 Schematic representation of director orientation of cholesteric liquid crystals.

The studies to date have shown that an interplay of the surface anchoring and elastic energy penalties existing in the interactions of the colloidal species with size R where the elastic deformations (scales with $\sim KR$, K is the elastic constant $\sim 10^{-11}$ N) become comparable with the surface anchoring energy (scales with $\sim WR^2$, W is the surface anchoring energy $\sim 10^{-6}$ Nm^{-1}) around R = 1-10 μm.[10] Above this size range is the regime where the elastic interactions play a dominant role in determining the overall interactions of the colloidal inclusions. However, below this size range is the regime where the influence of the elasticity becomes less pronounced and that is usually

open to surprising characteristics of the positioning of colloidal species.[12,31,46]Previous studies regarding the assembling of nanoparticles at the interfaces of CLC droplets and shells have shown that, by tuning the wettability of the nanoparticles, anchoring strength, and bulk elastic properties of the CLC, it is possible to position the nanoparticles at the disclinations of CLCs. A recent work signified the importance of surfactants for either to make the nanoparticles more hydrophobic or increasing the anchoring strength at the interface to make them more homeotropic and more favorable for the adsorption of nanoparticles.[43,44] However, arguments exist as the surfactants interacting with both the CLC and the nanoparticles modify their properties which makes it harder to understand the mechanism underlying the pattern formation. [43,44] Thus, the characteristics of the positioning of nanoparticles, their interactions, and the symmetry of the colloidal assemblies at the interfaces that facilitate elastic interactions are yet to be investigated to understand the influence of the elasticity and the surface properties in their directed self-assembly.

In this study, we investigate the formation characteristics of the nanoparticle assemblies at the interfaces formed by LCs and aqueous phases. We hypothesize that the topological defects in LCs can be used to pattern nanoparticles to form long and complex assemblies of concentrated particles without using surfactants, which makes the conceptualization of interparticle interactions simply possible and allows modeling. The system we investigate is the nanoparticles adsorbed at the interfaces of the LC droplets dispersed in an aqueous phase. Such a system is one of the more complex ones, where the LC (either cholesteric or nematic) is confined with multiple boundary conditions, and the colloids differ in surface functionality to study the influence of surface chemistry on their assembly. The adsorption characteristics of the colloids in this divergent energy landscape were also investigated. We used a thermotropic, oily LC mixture of mesogen 4-cyano-4’-pentylbiphenyl (5CB), chiral dopant 4-(1-methylheptyloxycarbonyl)phenyl-4-hexyloxybenzoate (S811), and a photoreactive mesogen 4-(3-acryloyoxy-propyloxy) benzoic acid 2-methyl-1,4-

phenylene ester (RM257). RM257 mesogens influence the elastic and surface anchoring properties[47] of the LCs and enable the synthesis of cholesteric disclinations without using additives to satisfy the anchoring conditions. Also, the photoreactive mesogens can be polymerized to form polymers templated from the CLCs and help characterize the positioning of individual colloids at their interfaces through electron microscopy. In this study, we investigated the interplay between the elastic and electrical double-layer interactions for the formation of the nanoparticle-rich assemblies and define strategies to finely tune the interparticle interactions to form well-defined fingerprint assemblies of the nanoparticles using LC-aqueous interfaces

CHAPTER 2

LITERATURE REVIEW

Colloidal assembling of particles is an important field of science that has many applications, especially in electronics, optics, and sensing. Directing the particles to form desired assemblies is a challenge since the scale of these systems is very small. Interparticular interactions play a large role to tune the assemblies; hence, liquid mediums, where it is easy to tune these interactions, are favorable systems for directed assembly. Liquid crystals are an especially important liquid medium since it provides another interaction between particles due to their ordered structure. Particles in the bulk or interface of the liquid crystals distort the liquid crystal orders, and generate an energy penalty on LC mesogens, to minimize this energy penalty, it is more favorable for particles to localize specifically, which generates attractive or repulsive forces between particles. Moreover, the defects of liquid crystals are also favorable positions for particles to locate and minimize the energy associated with the defects. Much research had been done to better understand interparticular interactions and assembling of the particles at the interface or in the bulk of the LC medium.

One of the more important studies done on the interparticular interactions inside bulk nematic liquid crystals is done by Muševic et al.[22] In their work micrometer-size silica nanoparticles are dispersed inside rubbed glass slides. The thickness of the cell changes along the rubbing orientation from one to several microns. The surfaces of glass slides are functionalized so that they induce planar anchoring whereas the silica particles are functionalized so that they induce homeotropic anchoring. The reverse anchoring conditions between the surfaces act as a repulsive force that stabilizes the particles into the LC film. The director profile around the defect is effected by the cell thickness, which varies the elastic distortion occurring around the colloids. On

the thinner regions, a quadrupolar distortion is formed around the colloids whereas on the thicker regions, a dipolar distortion is observed. For dipolar droplets, a single hyperbolic hedgehog defect is observed along the rubbing direction, which can be seen in **Figure 2. 1a** as a black dot above the droplet. The representative illustration of the dipolar symmetry and the defect is shown in **Figure 2. 1b**. Because of the elastic strain, the particles spontaneously assemble into chain structures inside the LC bulk (**Figure 2. 1**c). At thinner regions, a quadrupolar symmetry occurs around the particles. A single closed loop line defect is generated around the particle which is called a Saturn Ring. The optical microscope image of the defect can be seen as two black dots around the particle can be seen in **Figure 2. 1d** and the representative illustrations of the defect and the quadrupolar symmetry in **Figure 2. 1e.** Because of the quadrupolar symmetry surrounding them, these particles spontaneously assemble into kinked chains that are perpendicular to the rubbing orientation.

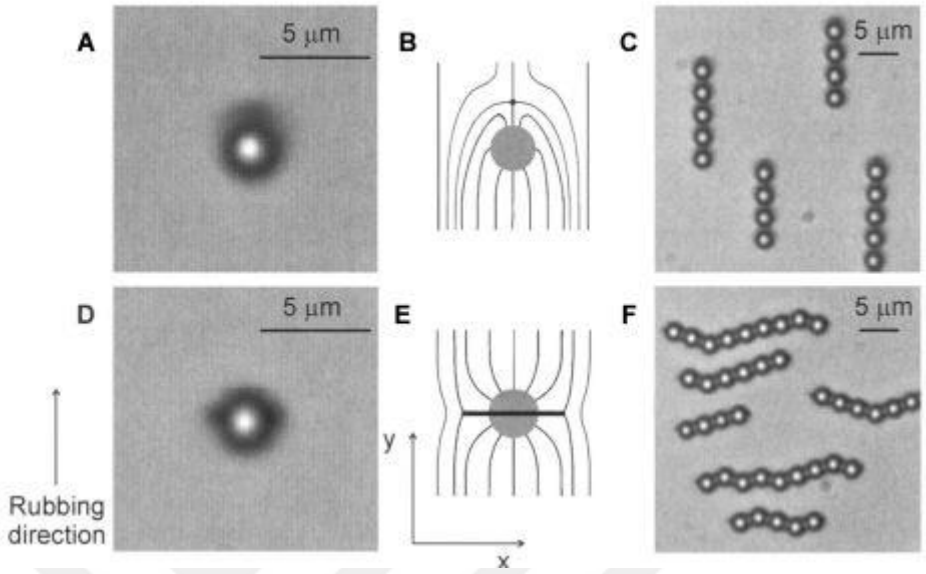

Figure 2. 1 a) 2.3 μm silica nanoparticle inside 5 μm thick layer affected by dipolar distortion and forming a hyperbolic hedgehog defect. b) Illustration showing the director with dipolar symmetry around the colloid. c) Chain formation occurs because of dipolar symmetry. d) 2.3 μm silica nanoparticle inside 2 μm thick layer affected by dipolar distortion and forming a Saturn ring disclination. b) Illustration showing the director with quadrupolar symmetry around the colloid. c) Chain formation occurs because of dipolar symmetry.[22] From Muševič, I., Škarabot, M., Tkalec, U., Ravnik, M. & Žumer, S. Two-dimensional nematic colloidal crystals self-assembled by topological defects. *Science (1979)* **313**, 954–958 (2006). Reprinted with permission from AAAS

Using laser tweezers particles are located close to each other. The time scale imaging of the particles showed that in close proximity they first assemble into kinked chains and then into 2D crystal structures (**Figure 2. 2a-e)**. Even the particles that are several micrometers away from the structures are attracted to the assemblies which, according to the authors, evidences the long-range nature of the elastic interactions.[22] The interaction energy for a particle to assemble at the end of a chain is calculated

to be ~ 800 k_BT, whereas the attraction to the sides of the chains is much weaker (~ 120 k_BT).[22]

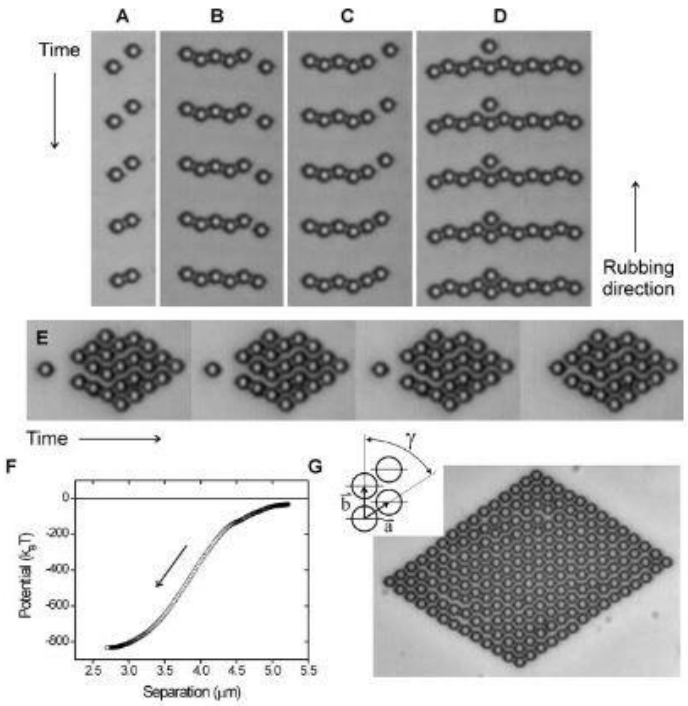

Figure 2. 2 Time sequence optical microscope imaging of the particles with quadrupolar symmetry in time sequences. a) initial imaging of individual particles b,c) after 0.8 s and d) after 2.2 s. e) Directed assembling of assemblies into 2D structures in 5s. f) Elastic energy measurement of the colloid with respect to its position to the vacancy in 2D crystal. g) A 2D crystalline structure formed by the directed assembly of the particles. From Muševič, I., Škarabot, M., Tkalec, U., Ravnik, M. & Žumer, S. Two-dimensional nematic colloidal crystals self-assembled by topological defects. *Science (1979)* **313**, 954–958 (2006). Reprinted with permission from AAAS

Figure 2. 3 Shows the directed assembling of a particle with dipolar symmetry. The calculated binding energy of these particles along the rubbing direction is much stronger (~ 4500 k_BT) from particles with quadrupolar as well as binding from the sides (~3000 k_BT) at ~ 1 μm. **Figure 2. 3a,b** shows time scale optical microscopy

imaging of two different cases. In **Figure 2. 3a,** the orientation of the dipole is parallel to the orientation of the dipole of the chain (shown in the top illustration of **Figure 2. 3**c). In this case the interaction between the colloid and the chain is repulsive. However, if the orientations are antiparallel, the interactions are attractive (**Figure 2. 3**). The attraction and repulsion are due to the interplay between the elastic strain and elastic defect respectively. Using these interactions it is possible to grow 2D crystalline structures from colloids with dipolar symmetry as can be seen in **Figure 2. 3d**.

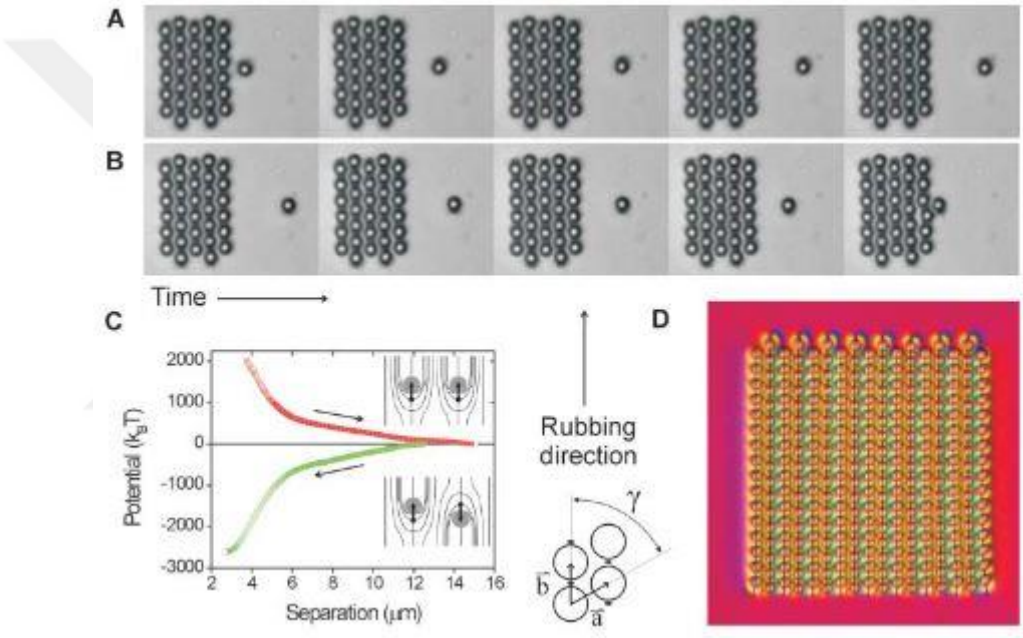

Figure 2. 3 Time sequence optical microscopy imaging of colloids with dipolar symmetry. a) The interaction is repulsive if the dipole of the single particle is parallel to the dipole of the chain and b) it is attractive if it is antiparallel. Time span is 4s. c) Calculation of the attractive and repulsive energies with respect to the particle's distance to the assemblies. d) 2D crystalline assemblies of colloids with dipolar symmetries. From Muševič, I., Škarabot, M., Tkalec, U., Ravnik, M. & Žumer, S. Two-dimensional nematic colloidal crystals self-assembled by topological defects. *Science (1979)* **313**, 954–958 (2006). Reprinted with permission from AAAS

The bulk elasticity of the liquid crystals is essential for LC-mediated interparticular interactions and hence, assembling. Working at the aqueous interfaces instead of bulk liquid crystals gives important control over the system. The interfacial properties of the liquid crystals (mainly its anchoring) can be tuned by the adsorption of surfactants or lipids. Changing the anchoring of the liquid crystals changes the elastic strain thus the interparticular interactions. Moreover, electrolytes can be used to screen the electric double layer of particles at the interface to change the electrostatic interactions. This means that different assemblies can be generated, erased, or switched between using additives. Another study by Koening et al. investigated the decoration of aqueous interfaces of nematic liquid crystal interfaces with microparticles.[48] In this study DMOAP functionalized 2 μm sized Silica particles adsorbed on nematic LC in a metal specimen grid supported on an OTS functionalized glass microscope slide. Both DMOAP and OTS induce homeotropic (perpendicular to the interface) anchoring on LC mesogens. Initially, LC film is placed into UP water where the LC anchoring is planar (parallel to the interface) at the top and homeotropic at the bottom due to the OTS functionalized glass. After the adsorption of nanoparticles to the LC-water interface, water-soluble surfactant SDS is added to water to induce a homeotropic interface at the top interface of LC. A representative schematic of the system is given in **Figure 2. 4a,b**. At the 5CB-aqueous interface with different anchoring, the director of liquid crystal surrounding a single particle microparticle change significantly, which changes the strain profile around the microparticles. Polarized optical microscopy images and representative illustrations of the director field derived from these observations are given in **Figure 2. 4b-e** for particles adsorbed at the planar interface and **g-j** for particles adsorbed at the homeotropic interface. At planar anchoring, two sides of the particle two bright lobes (regions where LC ordering is distorted from planar), and a single point defect (boojum) are generated at the interface due to the distortion created by the microparticle which can be seen as a dark point left to the particle in **Figure 2. 4c.** As the director orientation at the interface changes from parallel to perpendicular, the defect position is shifted from the interface to the bottom of the particle.

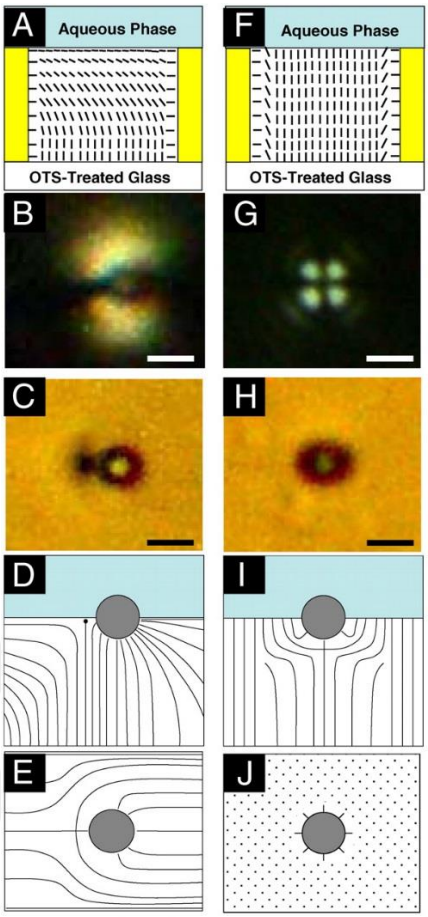

Figure 2. 4 a) Schematic representation of the system when the anchoring at the 5CB-aqueous interface is homeotropic. b) Polarized and c) brightfield image of a DMOAP functionalized particle at a homeotropic 5CB-aqueous interface. Schematic representation of the d) side view and e) top view of the director field of LC surrounding a DMOAP functionalized particle at a homeotropic 5CB-aqueous interface.[48] Copyright (2023) National Academy of Sciences

At planar interfaces, the dipolar symmetry (and the point defect) of the LC orientation around the microparticle leads to an attractive interparticular interaction between the nanoparticles. The interactions arising due to the LC elastic energy is estimated as $U = 4\pi KCa^4(1 - 3\cos^2\theta)/R^3$.[48] K is the elastic constant, a is the center-to-center separation distance between to particles, θ is the angle between the center-to-center separation plane and the the nematic director, and R is the radii of

the particles. When the LC anchoring is planar interface, it is observed that the DMOAP functionalized microparticles form chain-like assemblies that grow into branched structures as the particle concentration increase (**Figure 2. 5a**)**.** The origin of the chain-like structures are the attractive forces between nanoparticles originated from the dipolar symmetry of the LC mesogens. Upon addition of 1.3 mM SDS to UP water, the dipolar symmetry rotates and interparticular interactions change from attractive to repulsive, leading to the dismantling of the branched structures (**Figure 2. 5b)**. The formation of assemblies is reversible. As the attractive forces are changed to repulsive upon adsorption of SDS to the interface, when SDS molecules are desorbed from the interface, it is observed that the branched structures are reformed.

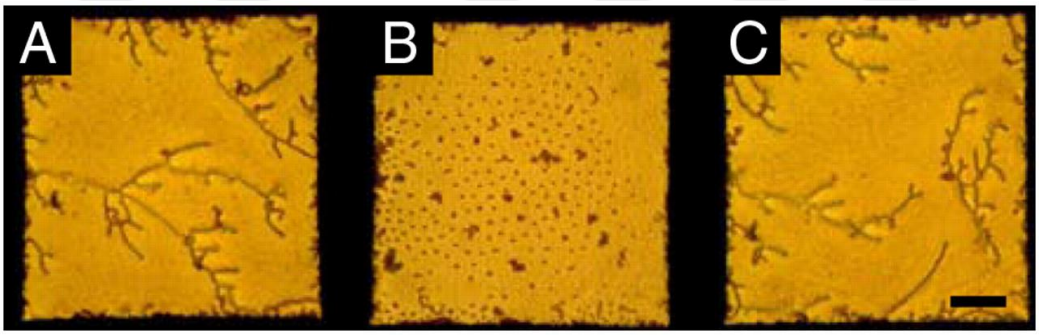

Figure 2. 5 a) Chain-like assemblies formed by DMOAP functionalized microparticles at the planar 5CB-aqueous interfaces. b) As 1.3 mM SDS is added to the chains are dismantled and random positioning of the microparticles is observed. c) Concentration of SDS is decreased back to below 0.5 mM.[48] Copyright (2023) National Academy of Sciences

Deformation induced by the colloids dispersed in liquid crystals is affected by the size of the colloid. Loudet et al worked on silicone oil droplets dispersed in bulk liquid crystal films to show the significance of the size of the dispersed phase mediating the elastic interactions.[49] First of all, liquid crystal E7 is mixed with isotropic silicon oil and injected into between two PVA-rubbed glass slides. The system is thermally quenched to 55 °C and back to room temperature. After thermal quenching, it is observed that the silicon oil is phase-separated into small droplets as

can be seen in **Figure 2. 6a**. It is observed that these small diffuse rapidly and coalesce with others to form larger droplets (**Figure 2. 6b**). When the droplets reach a critical size (~ 2 μm), the merging of the droplets stops and instead, small chains of silicon droplets start to form (**Figure 2. 6c**). As more droplets reach the critical size, the chains start to grow (**Figure 2. 6d**). Coalescence or chaining of the droplets is dependent on the droplet size, or more accurately competition between the energy required for the liquid crystals to maintain its orientational ordering (Ka, K is the elastic constant and a is the droplet diameter) and the silicon oil induced anchoring energy of the droplets (Wa^2, W is the surface anchoring energy). Silicon oil induces homeotropic anchoring on the LC mesogens. For smaller droplets, the anchoring energy is smaller than the elastic energy of the mesogens. Hence, instead of satisfying the homeotropic anchoring boundary condition, mesogens preserve their orientational ordering. In this case, not much distortion around the droplets was observed. In these droplets, instead of positioning normally to the interface, the LC mesogens assume a random orientation at the interface (**Figure 2. 6e**). Due to the lower strain around them, these droplets freely diffuse in the LC bulk and merge upon colliding. When the droplets reach the critical size, that is a > K/W, mesogens assume their perpendicular orientation around the droplets. This distorts the orientational ordering of the mesogens and generates a large strain around the droplet and a single hedgehog defect near it. Similar to solid particles in **Figure 2. 1b**, the dipolar symmetry of the mesogens results in attractive elastic interparticular forces. To minimize the elastic energy penalty induced on the mesogens by the large strains, the droplets are drawn to each other and form chain-like assemblies.

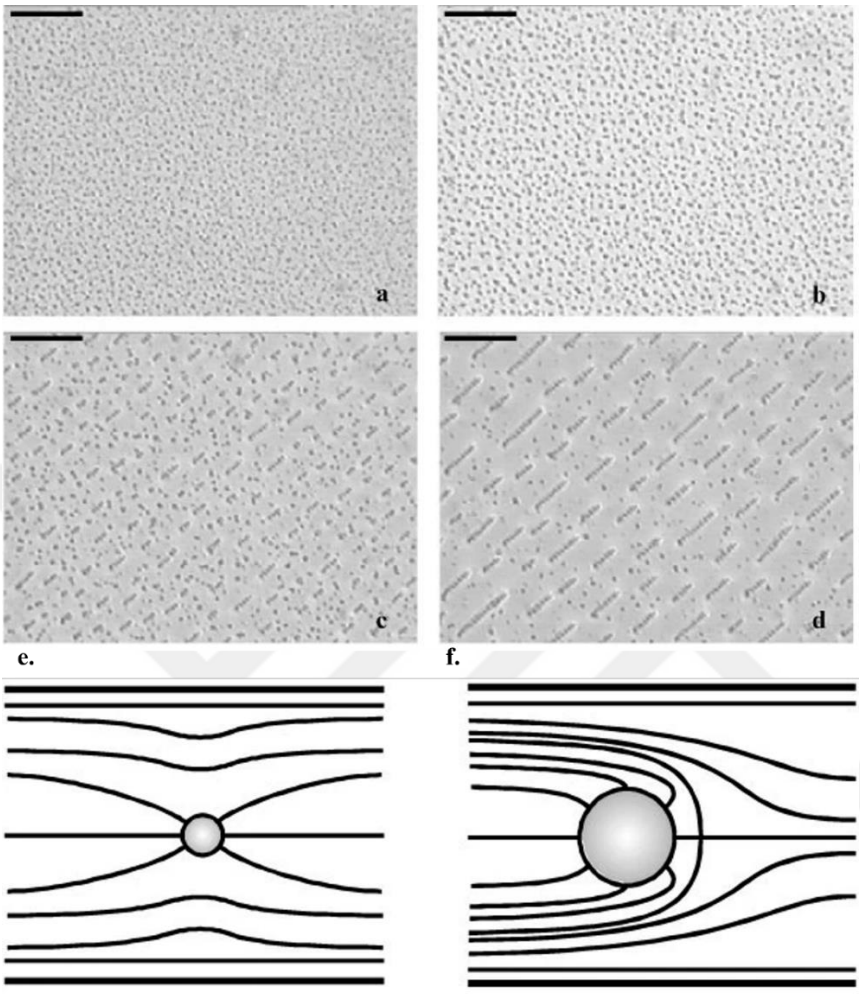

Figure 2. 6 Optical microscopy imaging of silicon oil droplets dispersed in liquid crystal. a) At first small droplets with a diameter a < 2 μm is formed (t = 20 s). b) Small droplets diffuse and merge with each other to form larger droplets. c) Larger droplets assemble into chain-like structures (t= 55s). d) Chains grow as time passes (t=120). Representative illustration of the deformation induced by the silicon oil droplets. Dark lines represent the director of the LC mesogens. e) Deformation induced by the small droplets. f) Deformation induced by larger droplets. [49] Reproduced with permission from Springer Nature

Assembling of particles at the LC-aqueous interfaces is not limited to films. Another geometry that is subjected to high interest is liquid crystals in spherical confinement. The emulsion of LC droplets can relax into different stable or meta-stable structures with different types of defects and director profiles depending on the boundary conditions. Mondiot et al. studied the adsorption of low-concentration micrometer-sized polystyrene particles (1 or 2 particles per droplet) at the aqueous interfaces of nematic LC droplets.[50] In the research, they used a mixture of 5CB with reactive mesogen to polymerize the LC droplets to form polymeric materials chemical patches. Firstly, LC droplets are emulsified into 10 v% glycerol solution. Glycerol is used to induce planar anchoring to the mesogen and also to increase the viscosity of the medium so that the imaging of particle adsorption can be done easily. The solution also contains fluorescent labeled polystyrene particles with a size of 1 μm. The system is imaged with combined FL-polarized microscopy. **Figure 2. 7a,b** shows the polarized and brightfield images of a droplet with a diameter 10 μm. Two-point defects (also known as "boojums") at each pole of the droplet signify that the structure is so-called Bipolar structure and confirms the planar anchoring boundary condition (**Figure 2. 7c,d)**. FL imaging of the droplet showed that PS particles were positioned specifically at one of the poles of the droplet, where the point defect resides. Similarly, **Figure 2. 7e,f** shows the polarized and brightfield images of a droplet with bipolar configuration. FL imaging showed that most of the particles are positioned at each pole of the droplet with a separation angle of 180 °. However, it is also observed that some particles are adsorbed on the same pole. It is noted by the authors that DMOAP functionalized silica nanoparticles (that induce homeotropic anchoring) give similar results. This suggests that the attraction to the defects has little dependence on the surface chemistry of the particle.

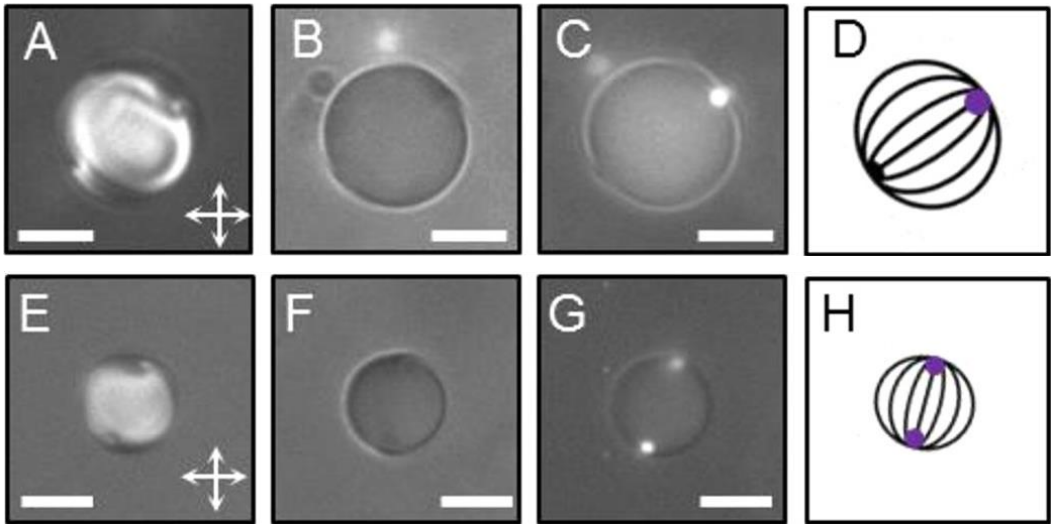

Figure 2. 7 a) Polarized b) brightfield image of a planar LC droplet with bipolar configuration. Droplet diameter 10 μm. Single FL polystyrene particle with a diameter of 1 μm is adsorbed at the interface d) Illustration of the particle droplet structure. e) Polarized and f) brightfield Combined fluorescent and polarized optical microscopy image of a planar LC droplet with bipolar configuration. g) Droplet diameter 6.5 μm. Two FL polystyrene particle with a diameter of 1 μm is adsorbed at the interface h) Illustration of the particle droplet structure.[50] Reprinted (adapted) with permission from Mondiot, F., Wang, X., De Pablo, J. J. & Abbott, N. L. Liquid crystal-based emulsions for the synthesis of spherical and non-spherical particles with chemical patches. *J Am Chem Soc* **135**, 9972–9975 (2013). Copyright (2023) American Chemical Society

Interactions of multiple colloidal particles at the curved interfaces of LCs give rise to complex arrangements of colloids that are not seen at the interfaces of LC films. Wang et al. showed that the interplay between the surface defects, elastic interactions, and spherical confinement gives rise to 32 distinct assemblies of 1 μm polystyrene particles at the aqueous interfaces of 7-20 μm nematic LC droplets.[51] The assemblies are imaged with fluorescent microscopy, however, they are also imaged with polarized optical microscopy to confirm that assemblies are formed at the defects. To characterize the different arrangements, they measured the center-to-

center angle between droplet assemblies and mapped them into a hexagonal lattice. First, they observed the minimum number of particles that can form an assembly which is two. They stated that the in this form they only take into account the particles that are located in the same boojum. They observed that only a single type of assembly occurs when two particles are located in a single defect, which can be seen in **Figure 2. 8a**. With increasing colloid number, the number of packings also increased with different probabilities of arrangements. **Figure 2. 8** shows the twenty-one different arrangements observed in droplets with five particles adsorbed. They also observed that the hexagonal assemblies did not form when LC geometry is a film inside up water, where no surface defects are present (**Figure 2. 8d**). In this case a repulsion between particles is observed which is suppressed when a high concentration of NaCl salt is added to the system. This suggests that the repulsion is due to the electrostatic forces. To better understand the difference between assemblies in LC films and droplets, a model is prepared that calculates the interparticular interactions between nanoparticles at different LC interfaces. The model showed that an electrostatic energy barrier is present for LC films in water that separates the particles. The attraction of the defect overcomes this elastic barrier allowing the particles to assemble into different structures.(**Figure 2. 8d**)

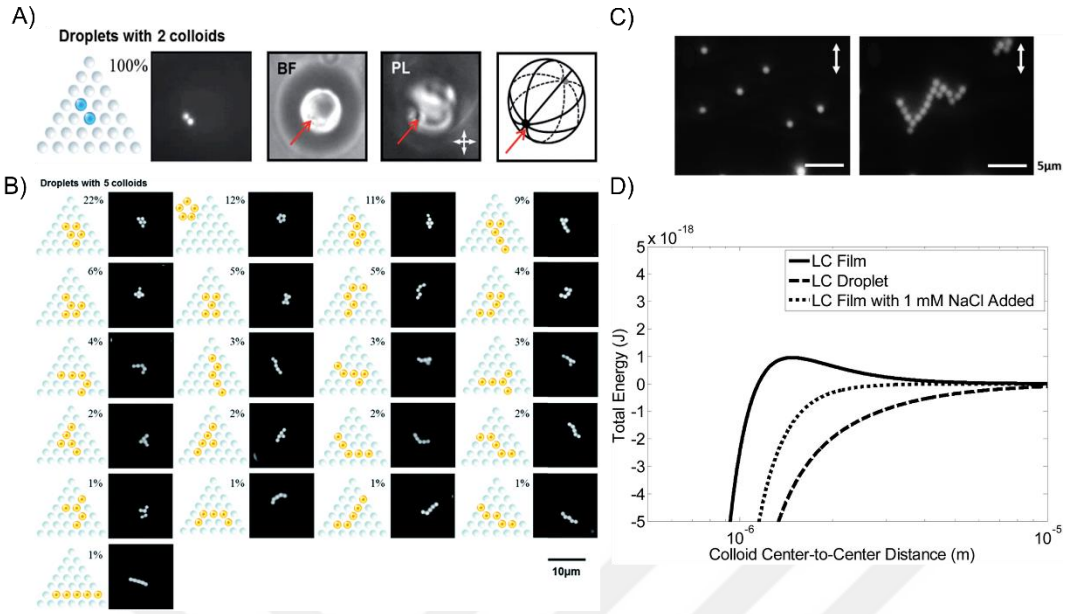

Figure 2. 8 Positioning of multiple 1 μm polystyrene colloids at the interface 5CB droplets. a) Positioning of two polystyrene particles. b) Adsorption of five polystyrene particles and probability distribution of the arrangements. c) 1 μm FL particles at the 5CB film-UP water interface (left), and at the 5CB film-UP water interface. d) Comparison of calculated interparticular interaction between two colloids in different interfaces.[51] Used with permission of Royal Society of Chemistry, from Organized assemblies of colloids formed at the poles of micrometer-sized droplets of liquid crystal, Wang, Xiaoguang; Miller, Daniel S.; de Pablo, Juan J.; Abbott, Nicholas L., 10, 44 2023; permission conveyed through Copyright Clearance Center, Inc

More recently, Tran et al. investigated the nanoparticle assemblies at the aqueous interfaces of Cholesteric Liquid Crystal with moderate homeotropic anchoring.[44] To achieve this chiral dopant CB15 doped 5CB droplets are emulsified inside an aqueous medium. Inside the medium cationic trimethyl alkylammonium bromide (C_8TAB) is added in different concentrations to stabilize the cholesteric liquid crystal droplets and induce homeotropic anchoring. According to the study, at moderate

anchoring strength, cholesteric liquid crystal mesogens cannot twist and retain their homeotropic anchoring boundary condition at the same time and instead sequential homeotropic and planar regions are generated at the interface with a periodicity ≈ p.[52] In this work, the surfactants at the interfaces plays a crucial role. They are used to not only induce the heterogenous hybrid anchoring boundary condition on the surface but also selectively adsorbed on the functionalized nanoparticle surfaces to alter their hydrophobicity, preventing aggregation. Moreover, surfactant adsorption on the CLC interface is also affected by the chirality of the droplets. As the surfactants adsorbed at the interface and alter the anchoring from homotropic to planar, an interface with heterogenous anchoring is generated. For the surfactants, it is more favorable to be adsorbed on the already homeotropic regions than the planar regions. This results in the segregation of surfactants at the interface of the droplets, which is called preferential adsorption of surfactants and lipids. Three key factors are highlighted in this work, to accomplish directed particle adsorption at the stripes of CLC droplets with hybrid anchoring. First of all, the degree of hydrophobicity of the nanoparticles is important. Surfactant concentration and surfactant tail length must be carefully selected. Surfactants with shorter tails enable better particle stability and prevent aggregation. For this reason, C_8TAB with eight carbon tails is chosen for the patterning of bare-silica nanoparticles. Increasing the surfactant concentration is another way to increase the hydrophobicity of the droplets. The size of the nanoparticles is another important factor affecting patterning. Larger particles are more prone to aggregation compared to the smaller ones. In their experiments, 200 nm amine-functionalized silica nanoparticles also formed assemblies, but in these assemblies, it is observed that they also form large aggregates that decrease the order in patterning. Hence, smaller 30 nm bare silica nanoparticles have been chosen for the rest of the experiments. Finally, the pH of the solution is also tuned, since it alters the zeta potential of nanoparticles and increases the adsorption of surfactants to the surfaces of nanoparticles. Thus, HCl in different concentrations is added to the system. As it can be seen from **Figure 2. 9** at low surfactant concentrations patterning is not achieved. When C_8TAB concentration is between 0.1-1 mM, no nanoparticles

are observed at the CLC interface. Silanol groups are negatively charged in pure water which means they are electrostatically repulsed by the electric charge of the CLC. Increasing the HCl concentration on the system, enables surfactant adsorption to the surfaces of the nanoparticles, increasing their hydrophobicity. This enables shifting from no adsorption to particle assembling (from red regions to green). Particles start to aggregate when the pH is further decreased. In this range (indicated by yellow regions) no patterns are observed. At higher surfactant concentrations (5-10 mM), the system is already hydrophobic, where the particles are located randomly at the CLC interface. Decreasing the pH enables the formation of chiral patterns but when the pH is too low a total coverage of a surfactant double layer will form on the surfaces of nanoparticles making them hydrophilic. In this case, no surface attachment, nor patterning is observed.

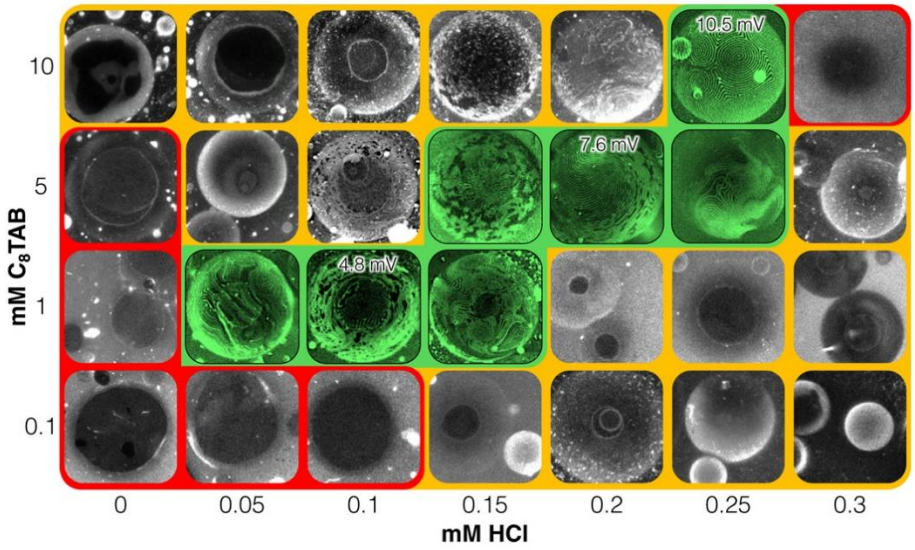

Figure 2. 9 Patterning of 30-nm Bare Silica Nanoparticles at the chiral focal conic domains of CLC droplets. Images in red regions indicate droplets with no particle adsorption. In yellow regions, particles are adsorbed at the interface but patterning is not observed. Green regions indicate the surfactant and acid concentrations at which the assemblies at conic focal domains are achieved. [44] From Tran, L. *et al.* Shaping nanoparticle fingerprints at the interface of cholesteric droplets. *Sci Adv* **4**, 8597 (2018). Reprinted with permission from AAAS

When the assemblies are formed at the CLC droplet interface, it is possible to tune the width of the assemblies by changing the chiral characteristics of the droplets. In **Figure 2. 10a,d**, the C_8TAB concentration in the system slightly increased from 7-15 mM. With increasing surfactant concentration, the width of the stripes increased but also they've become less ordered because of the increasing homeotropic anchoring strength frustrating the chiral twist even more. It is also possible to tune the stripe width by changing the chiral dopant concentration in CLC droplets (**Figure 2. 10b,c**). Increasing the chiral dopant shortens the length of the chiral pitch which in turn, decreases the width of the stripes. The width of the surface stripes is equal to the half-pitch of the cholesteric helix. Measurements showed that the length of the chiral pitch of the 5CB doped with 3 wt% CB15 is ~ 5μm. Measurements done by using fluorescent microscopy images showed that the stripe patterns for these droplets are close to the length of the half-pitch which is ~ 2.5 μm. Increasing the chiral dopant concentration to 7 wt% decreases the pitch length to ~ 1 μm, which in turn gives rise to the stripe width of ~ 600 nm. By further, increasing the dopant concentration to 10 wt% no assemblies are observed since the chiral pitch is decreased below 600 nm. The possible explanations given by the authors are that the fluorescent microscopy resolution is not high enough or switching of the unfrustrated hybrid anchoring to a frustrated cholesteric double twist.

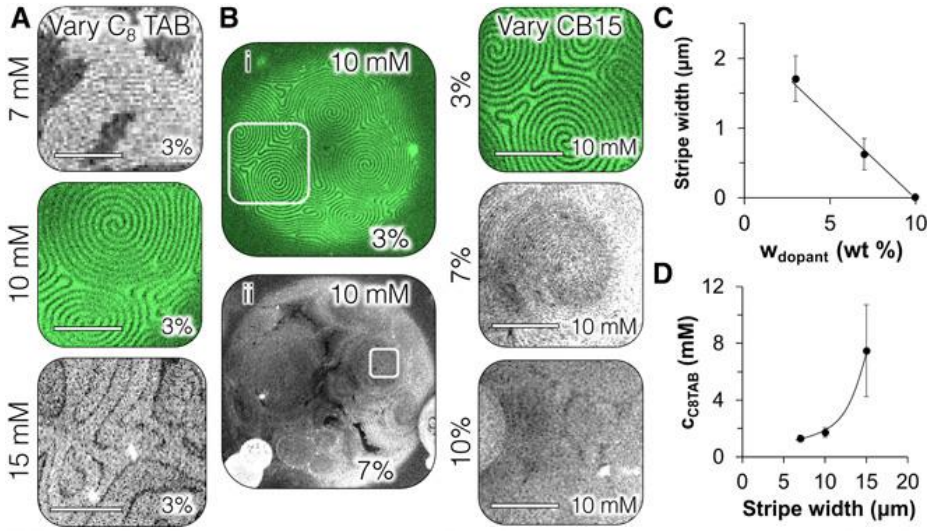

Figure 2. 10 a,d) Increasing the surfactant concentration increases the width of the stripe patterns. b,c) The stripe patterns can also be tuned by changing the chiral pitch of the CLC droplet. Increasing the amount of chiral dopant decreases the length of the chiral pitch, hence the width of the assemblies.[44] From Tran, L. *et al.* Shaping nanoparticle fingerprints at the interface of cholesteric droplets. *Sci Adv* **4**, 8597 (2018). Reprinted with permission from AAAS

The structures of interest in our work have been theoretically studied by Seč et al[36]. In their work, a variety of complex topologic defect structures are investigated computationally and separated under two different structure categories. The results of their thermal quenching experiments showed that when the droplets reach an equilibrium state and stable disclinations formed with the deformation of the chiral twist. These structures are comprised of metastable loops, links, and knots of defect lines. The defect lines are nematic disclinations with -1/2 winding. However, unlike nematic disclinations, where it is energetically unfavorable to maintain long isotropic regions, these disclinations do not minimize their length since it is prevented by a cholesteric helix. The metastable states depend on the size of the confining droplet and the length of the chiral helix. The ratio of these parameters is defined as the chirality parameter (N=4R/p). The complexity of the structures increases with increasing N. Example meta stable structures of links and knots are given in **Figure**

2. 11, however, it is important to note that these structures are only main representatives of most possible structures and apart from the limited disclination length there are no restrictions on their form for a disclination knot. Yet, the disclinations also increase the strain around the surrounding LC director and as the complexity increases it is more likely to find loops near the interface of the droplet.

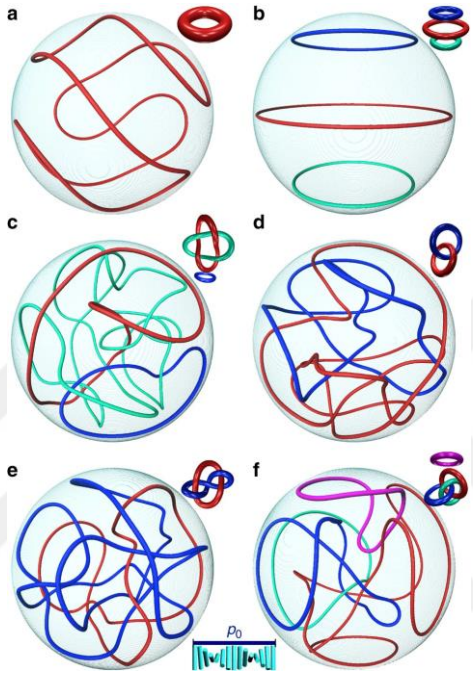

Figure 2. 11 Example Link and Knot Structures obtained for N=5. a) Single Loop Structure b) Three Loops without links c) a single loop in the bottom and a Solomon Link d) Hopf Link e) Whitehead Link d) Link with three components. Simplified versions of the structures are given in the top right corner of the illustration.[36] Reproduced with permission from Springer Nature

Increasing N over 6, disclinations are further pushed towards the interface where they are positioned a few director layers by the strong homeotropic interface. In these droplets line defects form a smectic-like quasi-2D layer that screens the effects of frustrated homeotropic boundary conditions from the bulk of the droplet. Inside the droplets, mesogen forms a layered structure with very high order. These structures are exclusively positioned at the smectic-like layer and the bulk is free of defects. In

its most stable form, a single line defect just below the interface entwines the droplet. (**Figure 2. 12a**) Further increasing the N to the limits of stable cholesteric phases result in kinked disclinations. In this form, it is stated that the bulk cholesteric ordering is non-uniform. (**Figure 2. 12b)** Since these disclinations act as smectic ones, the same rules for smectic disclination on droplets can be used to interpret the length of the disclinations which is determined as L~ 2πRN

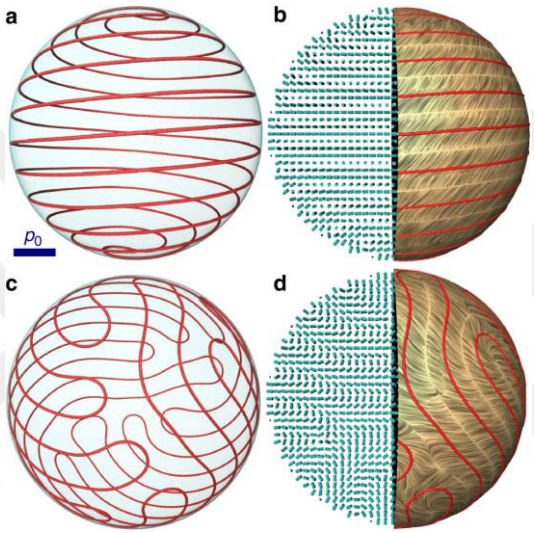

Figure 2. 12 CLC droplets with smectic-like subsurface layers and periodic loop structures. a) Disclination and b) bulk ordering of a droplet with N=12. c) Disclination and d) bulk ordering of a droplet with kinked defects. Reproduced with permission from Springer Nature

As it is described in this chapter, interactions between colloids and liquid crystals have been extensively studied. Past studies show that it is possible to assemble particles in complex structures by utilizing the three key concepts of liquid crystals. Moreover, these assemblies can be modified by changing the properties of the nanoparticles or the confining geometry of the LC. In our work we employ, the complex yet ordered line defects of cholesteric liquid crystal droplets as templates

for assembling. By using small particles localized at the interface, we can tune the assemblies to position the defects or diffuse freely at the interface.

CHAPTER 3

MATERIALS AND METHODS

3.1 Materials

4-cyano-4'-penthylbiphenyl (5CB), 4-(1-methylheptyloxycarbonyl)phenyl-4-hexyloxybenzoate (S811), 4-(3-acryloyoxy-propyloxy)benzoic acid 2-methyl-1,4-phenylene ester (RM257) were obtained from Jiangsu Hecheng Display Technology Co. Ltd. 2-dimethoxy-2-phenyl acetophenone (DMPAP), polyvinyl alcohol (PVA, 87-90% hydrolyzed, average mol wt 30 kDa), sodium dodecyl sulfate (SDS), tetraethoxysilane (TEOS), ammonium hydroxide (25-30%), dimethyloctadecyl[3-(trimethoxysilyl) propyl] ammonium chloride (DMOAP), (3-aminopropyl)triethoxysilane (APTES), succinic anhydride, dimethylformamide (DMF), and toluene were purchased from Sigma-Aldrich (St. Louis, USA). Absolute ethanol was purchased from Isolab (Germany).

3.2 Preparation of Cholesteric Liquid Crystal Mixtures and LC Emulsions

5CB was doped with chiral dopant S811 to induce a cholesteric structure. 5CB, S811, and toluene (co-solvent) were mixed thoroughly to ensure a homogenous mixture. Then, toluene was evaporated to obtain the cholesteric mixture. For emulsions, 3 μL of LC (either CLC or nematic phase) mixture was emulsified in 1 mL of an aqueous phase *via* a vortex mixer at 3000 rpm for 4 minutes. SDS was used to maintain tilted or homeotropic anchoring of LCs at aqueous interfaces.

3.3 Silica Nanoparticle Synthesis and Surface Functionalization

Silica nanoparticles were synthesized by the Stöber Method.[53] Absolute ethanol (60 mL) was mixed with ammonium hydroxide solution (3.6 mL) by a magnetic stirrer at room temperature for at least 30 mins. Then, TEOS (1.8 mL) was added to the mixture rapidly and the solution was mixed for another 24 h. After the synthesis, the particles are precipitated by centrifugation and rinsed with absolute ethanol at least 3 times. The rinsing procedure comprises the precipitation of particles by centrifugation at 10000 rpm for ten minutes, replacing the supernatant with the fresh continuous phase, and redispersing the particles in that phase with mixing and ultrasonication.

The size of the nanoparticles was determined by reaction medium compositions.[54] Finally, nanoparticle surfaces were functionalized to induce the intended LC anchoring.

To induce homeotropic anchoring, silica nanoparticles were functionalized with DMOAP. 1 vol% DMOAP was introduced into the aqueous suspension of nanoparticles and mixed inside an ultrasonic bath for 15 min with continuous sonication. DMOAP functionalized silica nanoparticles were rinsed with pure water at least ten times to ensure that free DMOAP molecules are extracted from the medium.

To induce planar anchoring and charging, silica nanoparticles were functionalized with carboxyl-terminated silane groups. First, the silica nanoparticles were functionalized with APTES molecules. APTES (138 μL) was added in nanoparticle suspension (25 mL) inside absolute ethanol and mixed with a magnetic stirrer overnight. The mixture was rinsed at least three times. After rinsing with absolute ethanol, the particles were rinsed three times with DMF and resuspended. The

nanoparticle suspension (20 mL) inside DMF was added dropwise into a flask containing 0.1 M succinic anhydrite dissolved in DMF (20 mL), while the mixture was constantly stirred with a magnetic stirrer. The system was then mixed at room temperature for another 24 h. After the functionalization was completed, nanoparticles were rinsed three times with DMF and three times with pure water.[55]

3.4 Preparation of Nanoparticle Adsorbed Polymers

To produce polymers templated from LC droplets, 72.5% 5CB was mixed with 25% RM257, 2.5% S811, and 1% photoinitiator DMPAP by weight in toluene. The mixture was then homogenized with a vortex mixer. After sufficient mixing, toluene was evaporated to obtain reactive mixtures of CLCs. 3 μL of this mixture was emulsified in the aqueous phase. After the formation of CLC droplets, the aqueous suspension of nanoparticles was added to the emulsion and mixed with a vortex mixer for another 4 min to ensure sufficient contact between the nanoparticles and LC droplets. The emulsion was equilibrated for an hour and later polymerized under a 365 nm UV Light source for 10 min. After the polymerization, free nanoparticles were carefully removed from the emulsion by rinsing with water at least four times (eight times when the nanoparticle concentration was high) to prevent adsorption after polymerization, especially during the drying. The droplets were collected from the bottom of the vial by natural sedimentation and the supernatant containing the free nanoparticles was replaced with fresh pure water. After that, the unreacted mesogens were extracted from the polymers by dissolving the LCs with absolute ethanol. To completely extract the mesogens, polymers were rinsed with absolute ethanol at least three times.

3.5 Preparation of Liquid Crystal Films

Glass surfaces were functionalized with either DMOAP (to induce homeotropic anchoring) or PVA (to induce planar anchoring). To functionalize the glass surfaces with DMOAP, clean glass slides were placed into a glass staining jar. The jar was filled with pure water and 1 vol% DMOAP volume was slowly added by a syringe. The jar was then placed into an ultrasonic bath and homogenized for 15 min. Excess DMOAP has washed away from the glass surface with pure water and the glass slides were dried with a flowing nitrogen stream. For PVA coating, clean glass slides were placed onto a spin coater, and 5 wt% PVA solution was spread onto the glass slides. Slides were rotated at 5000 rpm for 1 min. The cells were prepared by placing two coated glass slides on top of each other, while two spacers are placed in between. After the introduction of the LC, the cell has sealed with epoxy glue. For the dispersion of the nanoparticles in LC films, nanoparticles initially suspended in ethanol were introduced into nematic 5CB at room temperature. The absolute ethanol dissolved 5CB and then the nanoparticle suspension was homogenized using a vortex mixer. Finally, ethanol was evaporated, and the sample was introduced into the cell.

3.6 Optical Characterization of Liquid Crystal Films

Optical characterizations of the configurations of LC droplets and films were performed using an Olympus BX53 microscope equipped with crossed polarizers and a full-wave retardation plate. Analyses of the droplet size, defects, and pitch length were done using Fiji ImageJ.

3.7 Optical Characterization of Liquid Crystal Films

The polymers synthesized from LC templates were placed into 1 cm^2 glass slides dropwise and taped on SEM pins after drying. Samples were then coated with 95% Gold-5% Palladium alloy with a thickness of 4 nm with a Leica EM ACE200

Sputtering Device. Nanoscale surface imaging of the polymers was performed using a TESCAN Vega Scanning Electron Microscope equipped with a secondary electron detector and a four-quadrant backscatter detector.

3.8 Characterization of Nanoparticles

Concentration and zeta potential measurements were done by a ZetaSizer Ultra (Malvern Instruments Ltd., US) at room temperature. Nanoparticle size was also measured with the Multi-Angle Dynamic Light Scattering method of the ZetaSizer Ultra and the size measured was confirmed with SEM imaging. Measurements were done for at least three independent sets of experiments.

3.9 Zeta Potential Measurements

The procedure for the measurement of the zeta potential of the LC droplets is adapted from elsewhere. [12] Briefly, the LC emulsion is prepared by adding 10 μL of 5 CB into 990 μL pure water. The mixture is emulsified by a vortex mixer (1 min) and later sonicated with a tip sonicator for another minute, which resulted in a droplet size in the range of 300-400 nm. After that, the emulsion is diluted into the desired medium (10 μL 5CB-water emulsion into 990 μL desired medium). Zeta potential measurements were done by a ZetaSizer Ultra (Malvern Instruments Ltd., US) at room temperature

CHAPTER 4

RESULTS AND DISCUSSION

4.1 Cholesteric Liquid Crystal Droplets: The System of Interest

A room temperature cholesteric phase liquid crystal formed by doping 4-cyano-4'-penthylbiphenyl (5CB) with 2.5 wt% 4-(1-methylheptyloxycarbonyl)phenyl-4-hexyloxybenzoate (S811) was initially chosen to be the dispersed phase and it was emulsified in an aqueous phase with a vortex mixer to form spherically confined cholesteric liquid crystal (CLC) structures with diameters (*D*) between 5 to 100 μm **(Figure 4. 1**).

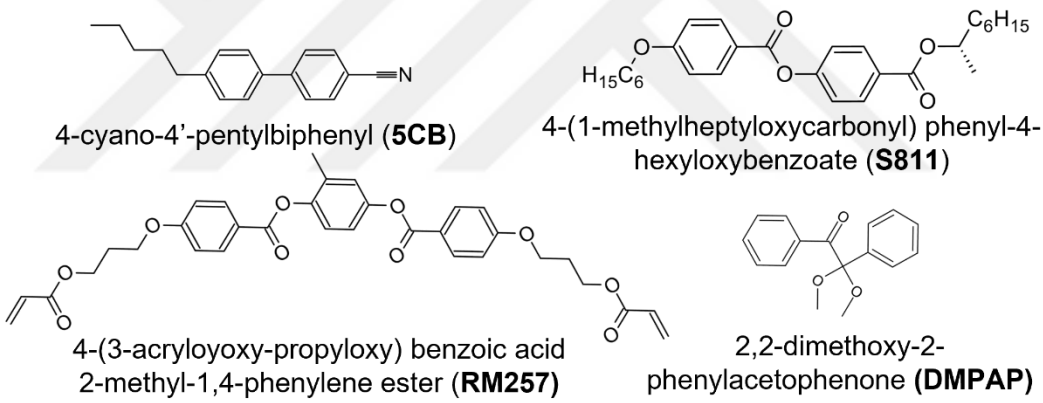

Figure 4. 1 Chemical structures of constituent molecules that are forming the dispersed phase of the emulsions are given: nematic liquid crystal (5CB), chiral dopant (S811), reactive mesogen (RM257), and photo-initiator (DMPAP).

Doping 5CB with 2.5 wt% S811 resulted in a cholesteric pitch length (*P*) of ~5 μm as we measured from droplets of the CLC mixture under polarized optical microscopy. Under these conditions, configurations of CLC droplets were characterized first under polarized optical microscopy and classified depending on

their chiral confinement coefficient (defined as $N = 2D/P$) and their interfacial anchoring. The dependence of configuration on N is given in

Table 4. 1 as a function of sodium dodecyl sulfate (SDS) concentration. It is known that 1 mM SDS causes a homeotropic anchoring at LC-aqueous interfaces whereas it causes tilted anchoring between 0 to 1 mM.[56]When the anchoring was planar (0 mM SDS), droplets with $N < 4$ primarily assumed a Twisted Bipolar Configuration (TBS). At higher N, the dominant configuration was observed to be the Radial Spherical Structure (RSS) which is consistent with the previous reports.[32–34] When the anchoring was homeotropic (at 1 mM SDS), droplets with $N < 1$ assumed Untwisted Radial Structures, which were similar to the nematic Radial Structures because of the unwinding of the chiral twist.[38–42] In droplets with intermediate N, Twisted Radial Structures and Link & Knot Structures (L&KS) were dominant.[36–41] Droplets with $N > 8$ resulted in the formation of Periodic Loop (PLS) and Concentric Loop Structures (CLS) (**Figure 4. 2**).[35,36,39,57] These configurations were consistent with the past literature on the configurations of droplets with homeotropic anchoring.[35–42] At intermediate SDS concentrations that result in tilted anchoring, we found the droplet configurations to assume a distribution that was dominant in configurations usually observed for homeotropic anchoring. Pure water (0 mM SDS) is known to mediate planar anchoring of LCs whereas 1 mM SDS is known to mediate homeotropic anchoring of LCs at their aqueous interfaces. The intermediate concentrations of SDS were chosen such that the LC interfacial anchoring was ~50° (0.4 mM SDS) and ~10° (0.8 mM SDS) with respect to the interface normal at the aqueous phase.[11,29]Brightfield and polarized optical microscopo images of the structures can be seen in the glossary in **Appendix A**.

Table 4. 1 . Dependence of droplet configurations to the chiral confinement coefficient and the anchoring of the mesogens at aqueous interfaces

	SDS Concentration															
	0 mM SDS				0.4 mM SDS				0.8 mM SDS				1 mM SDS			
	Chiral Confinement (N)				Chiral Confinement (N)				Chiral Confinement (N)				Chiral Confinement (N)			
	0-4	4-8	8-12	12+	0-4	4-8	8-12	12+	0-4	4-8	8-12	12+	0-4	4-8	8-12	12+
TBS	90%	6%	0%	0%	68%	0%	0%	0%	36%	0%	0%	0%	2%	0%	0%	0%
RS	0%	0%	0%	0%	5%	0%	0%	0%	31%	0%	0%	0%	19%	0%	0%	0%
TRS	0%	0%	0%	0%	0%	0%	0%	0%	3%	0%	0%	0%	45%	0%	0%	0%
L&K	0%	0%	0%	0%	0%	0%	0%	0%	0%	0%	0%	0%	17%	26%	0%	0%
CL&K	0%	0%	0%	0%	0%	0%	0%	0%	0%	0%	0%	0%	6%	13%	11%	0%
IS	0%	0%	0%	0%	21%	17%	6%	0%	20%	5%	0%	0%	0%	0%	0%	0%
PLS	0%	0%	0%	0%	6%	75%	53%	100%	10%	73%	86%	40%	11%	61%	78%	43%
RSS	10%	94%	100%	100%	0%	6%	24%	0%	0%	23%	14%	0%	0%	0%	0%	0%
CLS	0%	0%	0%	0%	0%	3%	18%	0%	0%	0%	0%	60%	0%	0%	11%	57%

TBS: Twisted Bipolar Structure IS: Intermediate Structures

RS: Radial Structure PLS: Periodic Loop Structure

TRS: Twisted Radial Structure RSS: Radial Spherical Structure

L&K: Link and Knot Structure CLS: Concentric Loop Structure

CL&K: Complex Link and Knot Structure

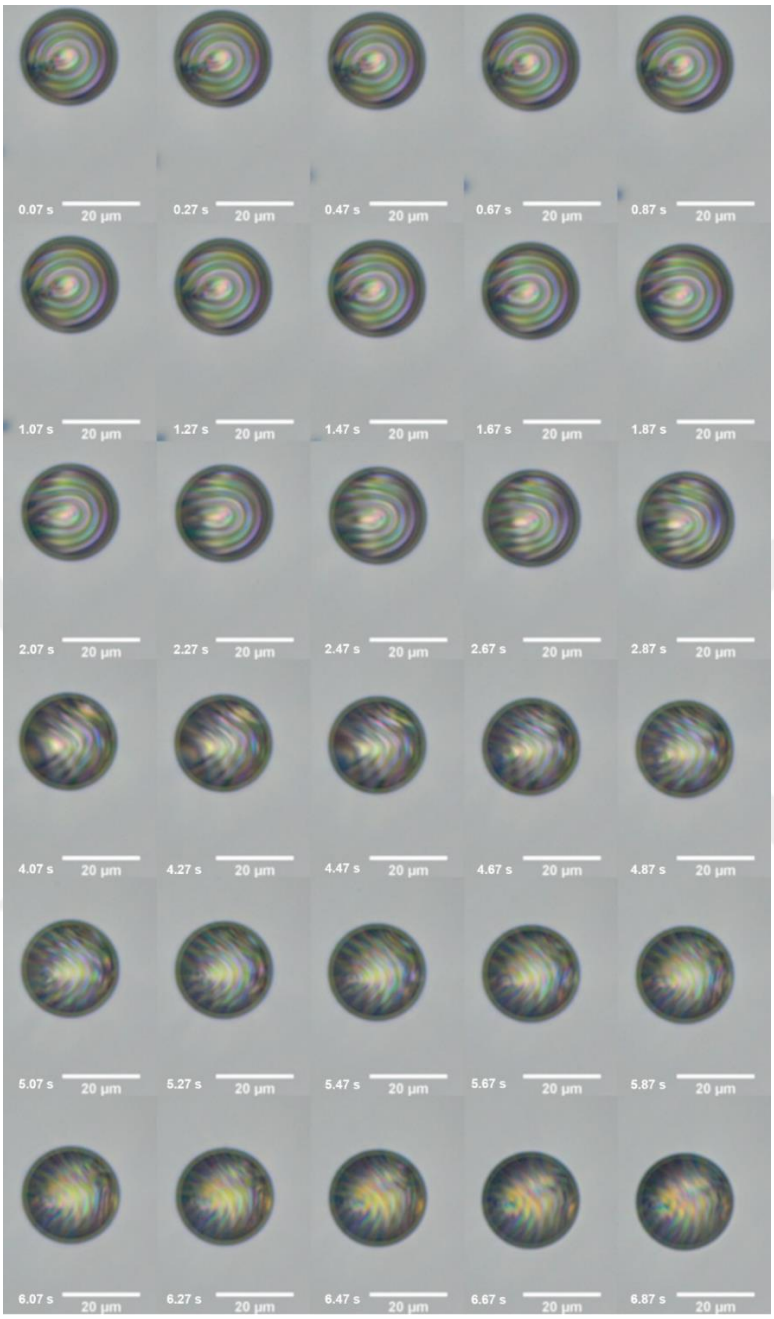

Figure 4. 2 Timescale Brightfield polarized optical microscopy imaging of a droplet with RSS configuration transforming to PLS structure upon addition of 5 mM SDS to the medium.

The most dominant configurations among these were PLS and CLS with the brightfield and polarized light images as shown in **Figure 4. 3a-d** below. The regular

fingerprint defect textures of the PLS that start from the two opposite poles of the droplet and the irregular concentric fingerprint textures of the CLS are the pronounced characteristics of the two structures depicted in the inset figures of the two structures (**Figure 4. 3a-d**). The LC-aqueous interfaces of the PLS and CLS are of utmost importance to us, as we reason that the defects that were shown to be positioned just below the interface in these structures create "favorable" interfacial regions for colloidal positioning. Such defects were also evident in the SEM images of the polymerized droplets that were formed via the polymerization of the mixtures of 5CB and S811 with the photoreactive mesogen 4-(3-acryloyoxy-propyloxy) benzoic acid 2-methyl-1,4-phenylene ester (RM257) followed by the extraction of the unreacted part (**Figure 4. 3e**). It is important to note that past studies showed that the anchoring properties change when 5CB is mixed with RM257, which shifts the planar anchoring of 5CB at interfaces with pure water to tilted anchoring.[47,58] The tilted interfacial anchoring due to mixing LC with reactive mesogen mostly resulted in structures equivalent to the droplets with homeotropic anchoring without using any surfactants. Thus, we concluded that the tilt angle of the mesogen mixtures at the interface of pure water is close to the perpendicular and it is possible to form disclination lines of PLS and CLS structures near the CLC-Water interface without using any surfactants.

Figure 4. 3e shows an SEM image of a polymerized droplet of 2.5 wt% S811, 25% RM257, and balance 5CB, where the periodic morphology resulting from the presence of the line defects is remarkable. We reasoned that the markedness of the defects is dependent on the amount of shrinkage the polymers experience after the extraction of the unreacted part.[47,58] **Figure 4. 3f** shows a sketch representing the possible director profile of the CLC mesogens at the interface that a line defect with a -1/2 twist with threefold symmetry positioned just below the interface as suggested in past studies.[36] Herein, we hypothesize that the deformation of the director due to the presence of the defect close to the interface is strong enough to affect the free

energy profile of the interfaces and create diverse interfacial energy landscapes for controlled patterning with colloidal particles.

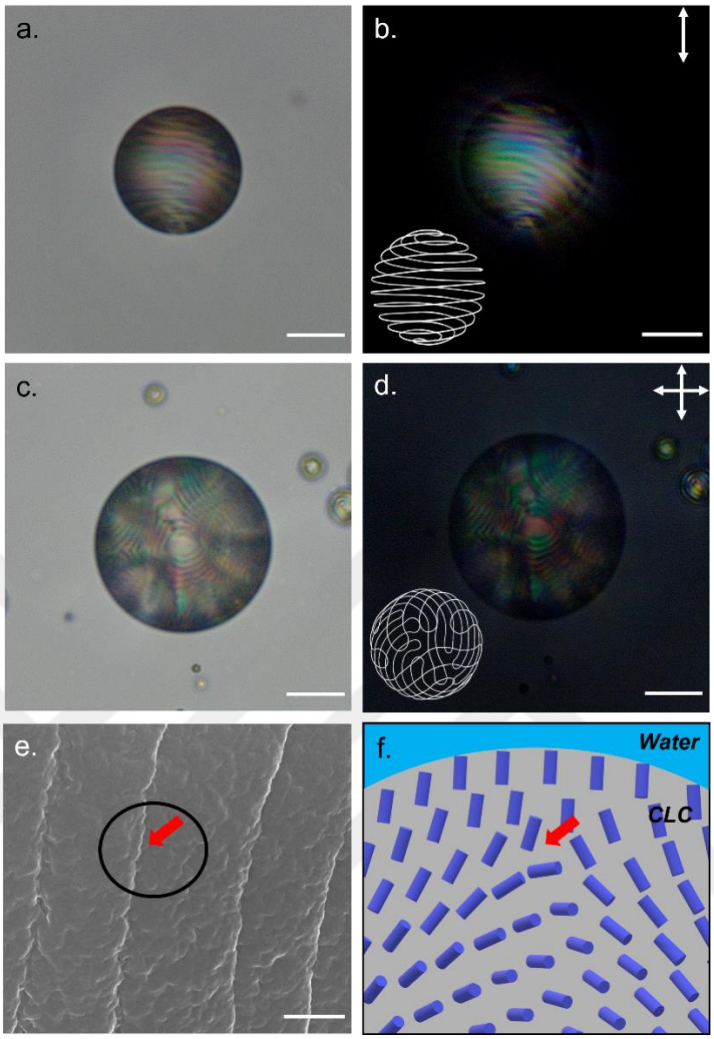

Figure 4. 3 a) b) Bright field and c) polarized images of the droplet with Periodic Loop Structure (PLS), N = 13. Scale bar: 15 µm. d) Bright field and e) polarized image of the droplet with Concentric Loop Structure (CLS), N = 18. The dispersed phases in these images are 2.5 wt% S811 in 5CB. f) SEM images of a polymerized droplet of 2.5% S811, 25% RM257, and 1% DMPAP in 5CB by weight forming Concentric Loop Structure (CLS) that evidences the presence of the concentric disclination line on its surface. Scale bars: (b-e) 15 µm, f) 1 µm. g) A schematic of the director profile around the near-surface defect. Red arrows show highly splayed regions.

Such shrinking characteristics of the particles are given in **Figure 4. 4**. The polymerized droplets were observed to shrink between 8 to 30% of their initial volume after extraction and drying. We observed no favorable axis during the shrinkage in either the planar, tilted, or homeotropic droplets consistent with the three-dimensional symmetry of the CLCs. However, the surfaces of the polymers synthesized from droplets with planar anchoring were smoother compared to those synthesized from tilted or homeotropic droplets, which we reasoned to arise from the radially symmetric director profile of the RSS and TBS compared to those resulted from homeotropic or tilted anchoring.

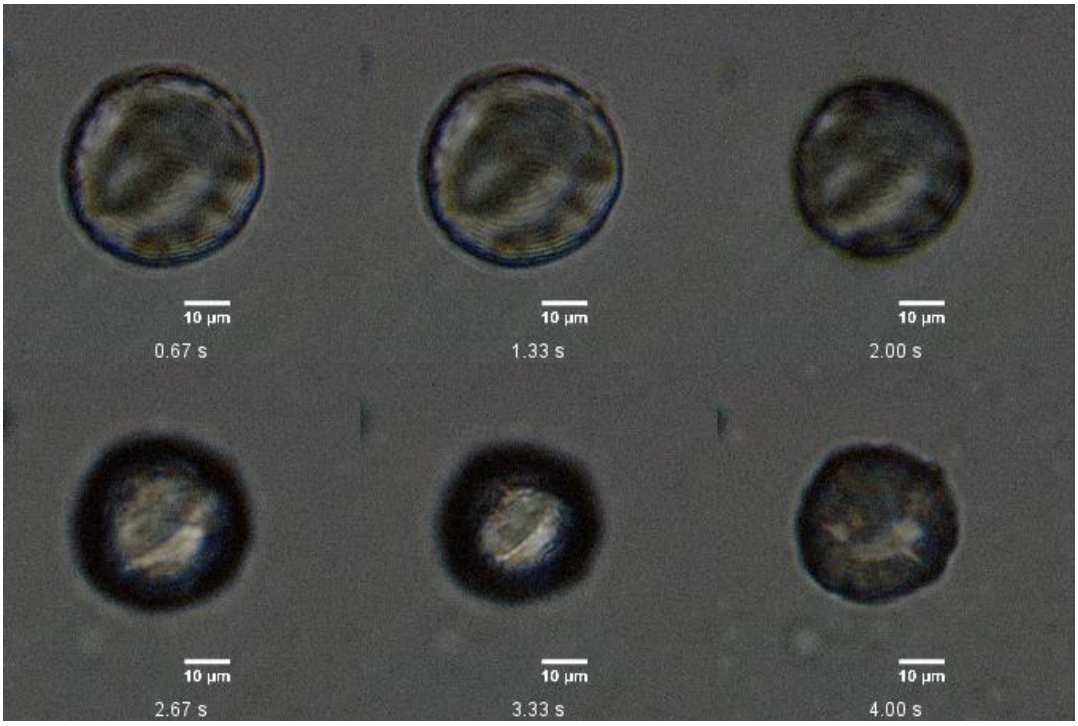

Figure 4. 4 Timescale brightfield imaging of a polymer particle synthesized from CLC droplets with tilted anchoring. After the extraction of CLC mesogens, droplets swelled with acetone and were imaged during the evaporation of acetone. The initial diameter of the droplet is 44 µm and the final diameter is 35 µm.

4.2 Characterization of the Director Profiles Around Nanoparticles

The effect of LC strain exerted by the nanoparticles was visualized by dispersing nanoparticles inside 5CB films and investigating the straining of LC in the vicinity of the particles under the polarized optical microscope. The LC films were sandwiched between glass slides that were functionalized with DMOAP to obtain a homogenous homeotropic surface anchoring along the nematic film. COOH silica nanoparticles induce planar anchoring of LCs, which are expected to induce two boojum defects at the two poles of nanoparticles (**Figure 4. 5g**). Optical micrographs of these dipolar defects created by 100 nm -COOH silica nanoparticles are given in **Figure 4. 5a-c**. For 100 nm particles, the strain exerted was so small that the singular particles can only be seen hardly in brightfield (**Figure 4. 5a**) but not much has been seen in polarized (**Figure 4. 5b**) or retarded polarized images (**Figure 4. 5c**). For 500 nm particles, the strain exerted was more evident. In brightfield images (**Figure 4. 5d**), the nanoparticles appeared as a blurred grey dot, however, in the polarized (**Figure 4. 5e**) and retarded polarized (**Figure 4. 5f**) images a four-petal structure can be seen. From such analysis, we concluded that the sketch in **Figure 4. 5g** captures the director profile around the nanoparticles.[51,59,60]

The results from these images coincided with the observations done regarding the adsorption characteristics of 100 nm and 500 nm -COOH silica nanoparticles. Large particles possessed more significant elastic deformations compared to smaller ones. Distortion of the ordering of the mesogens due to the planar anchoring inducing particles becomes more severe for the larger particles; hence the tendency to reduce it (what is defined as elastic quadrupolar interactions) becomes also larger which was the reason why the kinked chains and hexagonal formations emerged in the case of 500 nm particles opposed to the random adsorption of 100 nm particles (as discussed along with **Figure 4. 17**). For the smaller 100 nm particles, the elastic deformation possessed was not as significant as the larger to form chaining on nematic droplets.

Based on our observations with the polarized light microscopy, we sketched in **Figure 4. 5**h the possible director deformations around the nanoparticles when adsorbed to the LC-aqueous interfaces. We use such sketch and director profile to model the elastic interactions in Chapter 4.4 Equation 3.

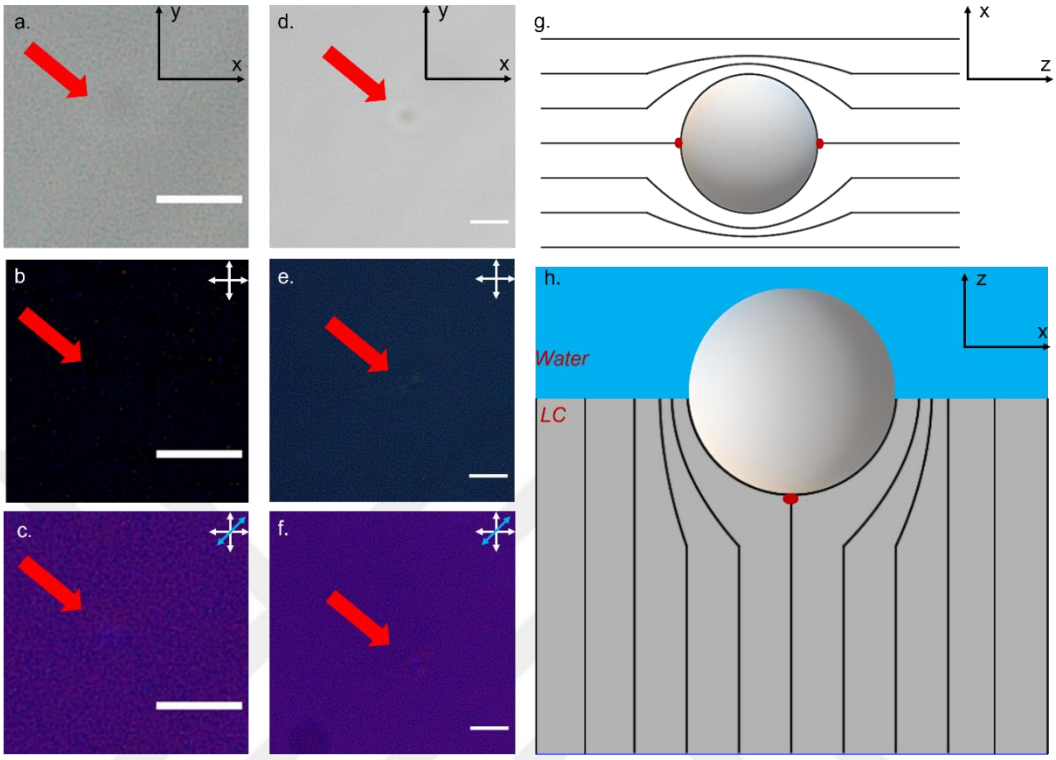

Figure 4. 5 Strain exerted by the nanoparticles can be observed under polarized microscopy depending on their size. 100 nm -COOH Silica nanoparticles inside nematic liquid crystal films optical micrographs collected under a) bright field, b) polarized light c) polarized light with retarder. Slightly more distinct strain images were collected from 500 nm -COOH Silica nanoparticle optical micrographs under d) bright field, e) polarized light, and f) polarized light with retarder. g) Schematic of a nanoparticle that induces planar anchoring inside LC bulk. Due to the particle, a quadrupolar symmetry and dipolar defects (shown as red dots) are created. h) Schematic of a nanoparticle that induces planar anchoring at the LC-Water interface. In the scheme, LC mesogens are positioned perpendicular at the interface (homeotropic anchoring). The quadrupolar symmetry is rotated 90° and one of the dipolar defects vanished. Scale bars: 1.5 μm.

4.3 Patterning of Liquid Crystal-Aqueous Interfaces

We hypothesized that the sub-interface line defects of the PLS and CLS droplets can be used to form long and complex colloidal assemblies. We built this hypothesis based on striking experimental evidence on the positioning of the nanoparticles at CLC droplet interfaces shown in **Figure 4. 6**. Different from the past examples that employed surfactants to tune the adsorption and surface properties of nanoparticles or preferentially saturate the CLC disclinations and physicochemically interact with the particle on the droplets[43], we did not use surfactants in our experiments in motivation to investigate the assembly characteristics of the colloidal species that are dictated by the interfacial and bulk properties purely with those of the colloids and LCs. In the experiments shown in **Figure 4. 6**, ~100 nm average-sized, carboxyl terminated silane functionalized spherical silica nanoparticles (-COOH silica, **Figure 4. 6a**), which induce planar anchoring [12], were adsorbed on the CLC droplets dispersed pure water. After the addition of the nanoparticles, the system was equilibrated for an hour which is necessary to ensure the adsorption of the nanoparticles on the defects and localization of the particles at the strained regions after the adsorption. After the equilibration, the reactive mesogens in the system were polymerized using UV-light to freeze the final structures. Details regarding the experimental methods are presented in Materials and Methods Section. In a previous report, we found the LC and the aqueous phase to almost wet equally the -COOH silica particles, thus, we expected the nanoparticles to be adsorbed significantly at the LC-aqueous interfaces.[12] Investigation of **Figure 4. 6** reveals that the adsorbed nanoparticles formed patterns at the interfaces of the CLC droplets that follow a fingerprint texture consistent with the cholesteric fingerprint structures of CLS droplets. The patterns covered the entire surface of the droplet forming paths of concentrated silica nanoparticle assemblies with periodic circle, line, and turn features observed in fingerprint textures (**Figure 4. 6**). The uniform thickness of the nanoparticle-rich assemblies was measured to be 336 ± 33 nm and the center-to-

center spacing was measured to be 1.42 ± 0.17 μm. Such measurements were correlated with the cholesteric pitch size expected from the droplets after shrinkage.

The patterning characteristics were significantly affected by the concentration of the nanoparticles. **Figure 4. 6b-e** shows the SEM images of the polymerized droplets after adsorption of -COOH silica nanoparticles at four different interfacial concentrations where the pH of the aqueous phase was set to 2. When the interfacial particle concentration was low (≈1 particle/μm^2, **Figure 4. 6c**), we observed a high fraction of the adsorbed particles positioned close to the defects. This result evidenced the presence of an elastic attraction of the particles toward the defects. This observation was remarkable as we did not readily expect a strong elastic deformation caused by the ~100 nm-sized particles to mediate elastic attraction towards defects, however, this result confirmed that it was indeed present in our system that was sufficient to position individual ~100 nm particles at defects. Consistently, although not strong, we have also observed a minor strain around the nanoparticles in our independent experiments when nanoparticles were dispersed in LC phases (**Figure 4. 5a-c**).

Increasing the nanoparticle concentration (or equilibration time) by an order of magnitude was enough to saturate the defects with aggregates of uniform thickness to form well-defined patterns as shown in **Figure 4. 6c-e**. As the nanoparticle concentration was increased over ≈30 particles/μm^2, nanoparticles on neighboring defects merged as shown in **Figure 4. 6d**. Above this concentration, the adsorbed nanoparticles filled in the regions between the defects, covering the patterns, increasing of which resulted in full coverage of the LC-aqueous interface. We did not observe a signature of cholesteric patterning at such concentrations (**Figure 4. 6**e). According to the findings reported in **Figure 4. 6**, we found the interparticle interactions are as important as the elastic interactions for the patterns to develop. More specifically, for example, when the concentration was low (**Figure 4. 6c**), we observed that some "free" particles were not located at the defects while the fraction of these "free" particles was much lower (almost none) at higher concentrations

(**Figure 4. 6b,d**). Equilibration time can also be tuned to define the thickness of the patterns. The less time pass the addition of the particles the fewer particles adsorb on the surface and localize on the defects. **Figure 4. 6f-g**, shows the polymerized droplets templated from CLS droplets with -COOH NPs adsorbed at the interface. According to the figure, the thickness of the particles increases as the time between NP adsorption and polymerization increases.

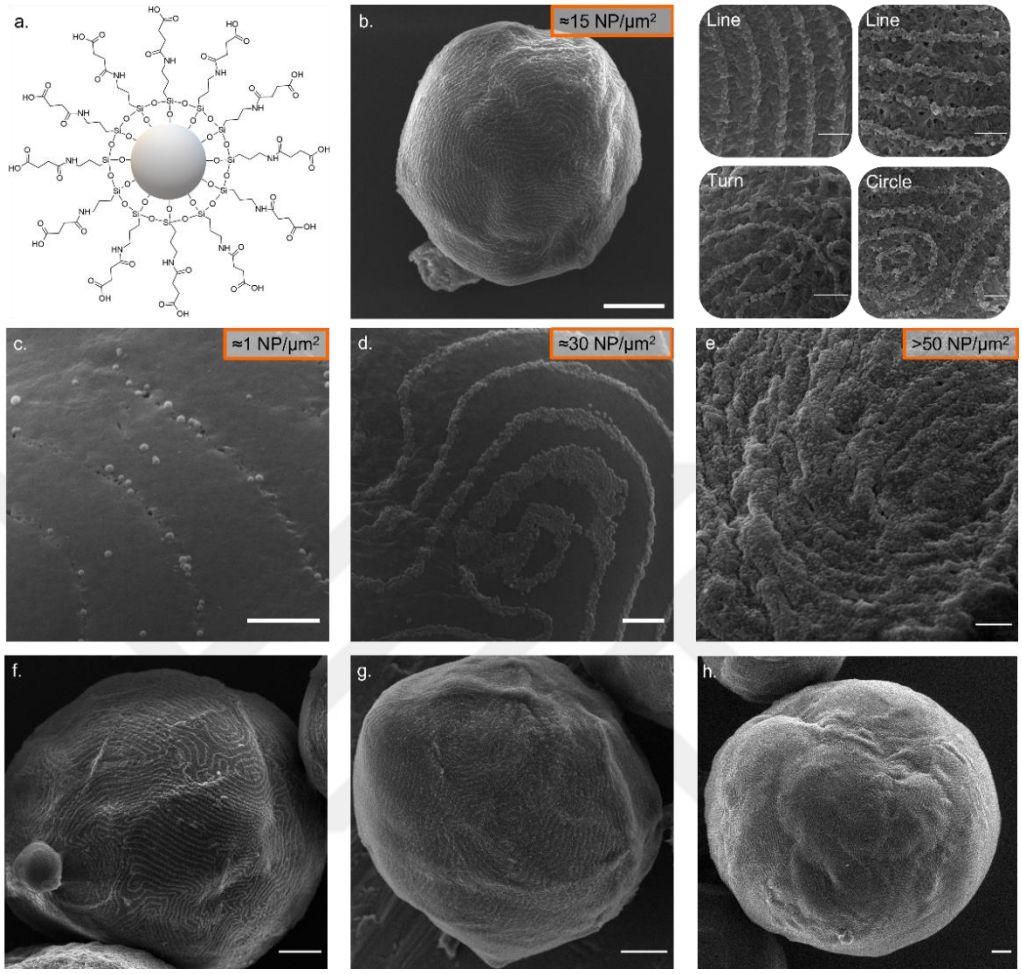

Figure 4. 6 a) A scheme representing the silica nanoparticles and their carboxyl-terminated silane surface groups. SEM images of the polymerized droplets adsorbed with ~100 nm -COOH silica nanoparticles with interfacial nanoparticle concentrations of b) ≈15, c) ≈1, d) ≈30, and e) >50 nanoparticles/μm^2. CLC droplets possess a CLS structure. Polymers were synthesized from CLC droplets with a composition of 2.5% S811, 25% RM257, and balance 5CB, by weight. The adsorption and polymerization were performed in a medium with pH=2. Scale bars: b) left, 15 μm, zoomed images, 1.5 μm, c-e) 1.5 μm. f-h) Example SEM images of polymers with total interface patterning

The distance between the defects can be adjusted by changing the chiral confinement coefficient of the droplets, allowing us to control the distance between the nanoparticle assemblies. **Figure 4. 7b-d** shows ~100 nm -COOH nanoparticles adsorbed on the CLS droplets with different chiral dopant loading. Decreasing the amount of chiral dopant increased the pitch length of the cholesteric twist and as a result, the distance between assemblies increased. By doing so, the ratio of area covered by nanoparticle-rich to nanoparticle-lean phases on the CLS interfaces can also be tuned. According to our measurements, the pitch length of the chiral twist is ~ 7 µm (**Figure 4. 7b**) when S811 concentration is 1 wt% and ~2 µm when it is 5 wt % (**Figure 4. 7d**).

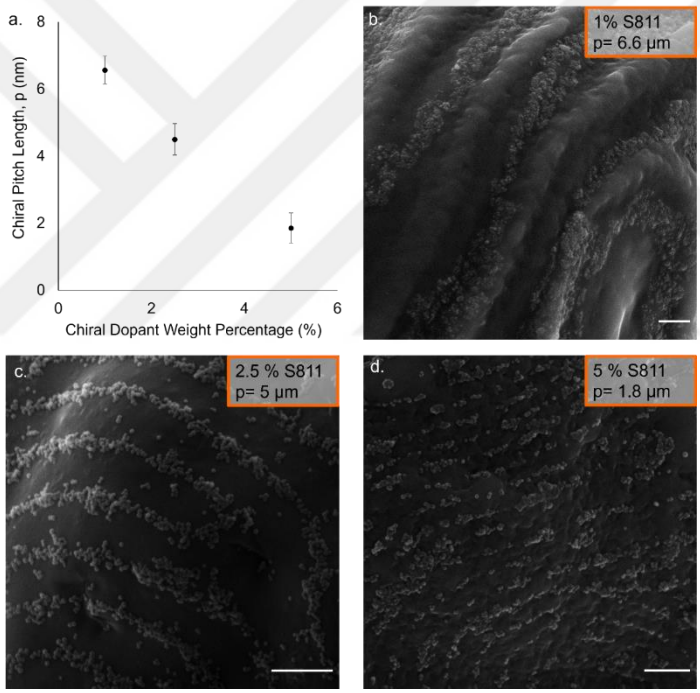

Figure 4. 7. a) Change of chiral pitch length with respect to the weight percentage of chiral dopant inside the LC mixture. SEM images were collected from polymers templated from b) 1%, c) 2.5%, and d) 5% S811, 25% RM257, and balance 5CB, by weight. The adsorption of 100 nm sized -COOH nanoparticles and polymerization were performed in a medium with pH = 3. Scale bars: 1.5 µm.

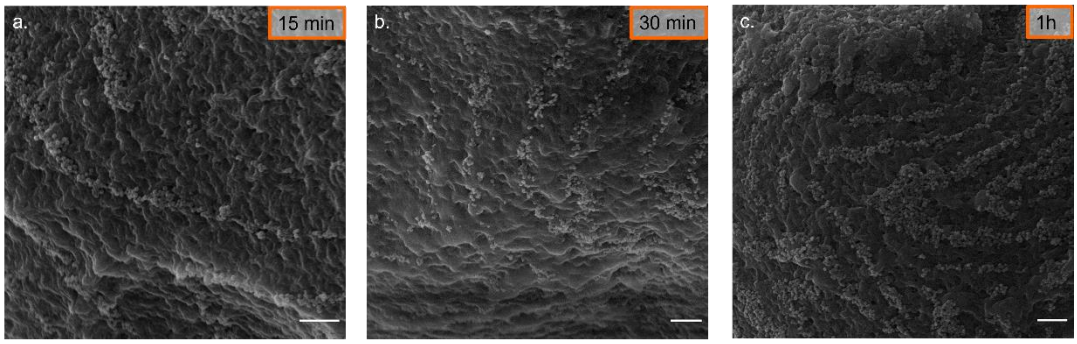

Figure 4. 8 a-c) Time-dependent adsorption of -COOH Silica Nanoparticles. CLC droplets are polymerized contacting with the particle after a) 15 min b) 30 min c) 1h. Polymers were templated from 2.5 wt% S811, 25 wt% RM257, and balance 5CB. The adsorption and polymerization were performed in a medium with pH = 3. Scale bars 1.5 µm..

We hypothesize that the heterogeneous elastic energy landscape at the interface of the droplet, influenced by the sub-interface disclinations of the PLS or CLS droplets, is essential for the patterning to occur. Thus, complex assemblies cannot be obtained for LC configurations with "homogeneous" interfacial energy landscapes. Moreover, the characteristics of patterning should be determined by the relative magnitudes of the interfacial elastic energy heterogeneity and the interparticle forces. These forces are considered van der Waals interactions, electrostatic double-layer forces, and the elastic interactions emerging between the nanoparticles due to the LC strain induced by the nanoparticles as discussed above. To this end, we have conducted a set of control experiments to test these hypotheses. These experiments can be classified into three sets namely the experiments to evaluate; (*i*) the influence of the presence of a diversified elastic energy landscape on the LC-aqueous interface, (*ii*) the effect of the LC strain induced by the particles, and (*iii*) the role of the particle-induced surface anchoring.

To evaluate the influence of surface elastic energy landscape, we first imaged the distribution of the adsorbed nanoparticles on nematic LC droplets. When the LC phase maintained nematic symmetry (non-chiral), droplet configurations (so-called

Bipolar, Pre-radial, and Radial) maintain mostly energetically "homogeneous" interfaces except on the boojum defects.[21,61] For these droplets, both the attractive splay energy exerted by the boojums or the near-surface hedgehogs as well as the interaction energy between the nanoparticles due to the strain created by the nanoparticles are estimated to be comparable to the Brownian energy (k_BT) for the 100 nm particles.[12,20,51,60,62] Hence, the nanoparticles were observed to assemble into random clusters on the interfaces of nematic Pre-radial (PRS) droplets (**Figure 4. 9a**) Second, to confirm the role of defects in chiral droplets, the positioning of nanoparticles on RSS droplets was investigated. In these experiments, 1% wt polyvinyl alcohol (PVA) was added to the aqueous phase to induce the planar anchoring necessary for RSS configuration after the formation of the nanoparticle assemblies on CLS droplets. With planar anchoring and the so-called "onion-like" layered structure, we consider the RSS droplets to provide energetically "homogenous" landscapes except for the two characteristic surface defects present. [32–34] Similar to nematic PRS droplets, the adsorbed -COOH silica nanoparticles on RSS droplets resulted in random clustering of the nanoparticles at the interfaces of RSS droplets (**Figure 4. 9b**). In a third experiment, we adsorbed the nanoparticles on CLS droplets and then heated the droplet to the isotropic phase and polymerized it before imaging. On isotropic droplets (**Figure 4. 9c**), we observed the vanishing patterns of the nanoparticles formed on CLS droplets (as in **Figure 4. 6**) and the presence of the random distribution of the particle clusters. Thus, experiments with PRS, RSS, and isotropic droplets confirmed that the patterning can only exist whilst the sub-interface line defects are present. Also, the observation with isotropic droplets confirmed that the patterning on the chiral defects is formed with reversible aggregates.

Second, to investigate the influence of the LC strain induced by the nanoparticles, ~500 nm average-sized -COOH silica nanoparticles were adsorbed on nematic PRS droplets (**Figure 4. 9d**). Hexagonal assemblies of such adsorbed nanoparticles were observed indicating the influence of elastic strain exerted by the

nanoparticles[31,48,51,60], but not resulting from the defect-driven self-assembly since particles did not localize at specific positions on the droplets. Instead, they formed "ordered" interfacial aggregates as a result of the elastic quadrupolar-quadrupolar interactions. To characterize the influence of the chirality in the LC phase, we imaged the distribution of the adsorbed, ~500 nm -COOH silica nanoparticles on RSS droplets (in an aqueous phase with 1% wt PVA). The initially present concentric disclinations disappeared upon the anchoring transition. Similarly, assemblies of ~500 nm particles on RSS droplets (**Figure 4. 9e**) did not show a sign of fingerprint patterning. Instead, hexagonal assemblies were formed (similar to the nematic counterparts). In this case, it was not possible to adsorb the particles on the liquid crystal interface because of the large electric double layer of the 500 nm nanoparticles and inhibition due to PVA-PVA interactions. Instead, the nanoparticles were adsorbed in pH=3 where the near-surface defects of the concentric configurations are present. After the adsorption and equilibration for an hour, the droplets were transferred into 1wt% PVA solution and left to equilibrate for another hour. In this case, with the changing of the configuration, the defect type and position are also changed. No sign of arrest of the assemblies was also observed after the anchoring transition, demonstrating the reversibility of the aggregates. It is important to note that the addition of PVA also changes the electrostatic interactions in the system. The zeta potential measurements of both the nanoparticles and CLC became -5.4 mV and -11.7 mV, respectively, upon the addition of *PVA*. The zeta potential measurements of different dispersed phases in media with different additives is given in **Appendix B**. Additionally, we observed the disappearance of the ~500 nm particle assemblies on CLS droplets after the removal of the LC phase upon heating into the isotropic phase as shown in **Figure 4. 9f**. We suspect that only the aggregates resulting from the van der Waals and electrical double-layer interactions were present, similar to the ~100 nm-sized counterparts as shown in **Figure 4. 9c**.

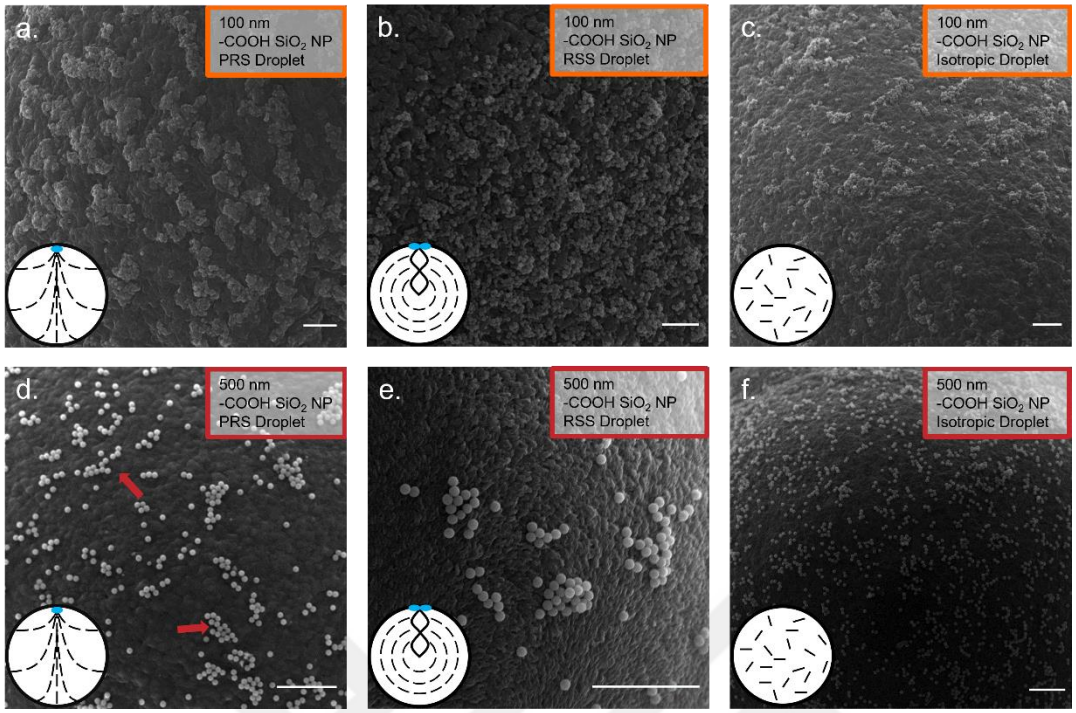

Figure 4. 9 SEM micrographs of the polymeric samples prepared from ~100 nm -COOH silica particles adsorbed on a) nematic liquid crystal droplets with Pre-radial Configuration, b) cholesteric liquid crystal droplets with Radial Spherical Structures (*N*~40), and c) isotropic droplets. SEM micrographs of the polymeric samples prepared from ~500 nm -COOH silica particles adsorbed on d) nematic liquid crystal droplets with PRS configuration, e) cholesteric liquid crystal droplets with RSS (N~20), and f) isotropic droplets. Scale bars: 1.5 µm. Droplets were prepared using a mixture of 2.5% S811, 25% RM257, and a balance 5CB by weight. For the continuous phase, water with pH=3 was chosen for a-f. However, for b and e, the media were changed to 1% wt PVA after the adsorption to induce planar anchoring. For g-i, the continuous phase was UP water. All the experiments were conducted at room temperature except for the isotropic droplets where the temperature of the media was raised to 50°C after the adsorption.

The third set of control experiments was conducted to question the generality of the patterning process regarding the surface properties of the particles. Silica nanoparticles functionalized with DMOAP were adsorbed on the CLC Droplets.

DMOAP functionalization is known to make the nanoparticles hydrophobic and induce homeotropic anchoring of LCs.[12,20] SEM images of the polymerized CLS droplets **Figure 4. 10a**) showed that the patterning was also achieved using the ~100 nm-sized DMOAP silica nanoparticles. In this case, however, the aggregates on the nanoparticles assumed a denser packing when compared to the -COOH counterparts potentially because of their hydrophobicity and possibly because of the ionic partitioning at the LC-aqueous interface which we explain below. Although there are minor differences in the packing of the DMOAP silica particles when compared to the -COOH-terminated counterparts, we note that both types of particles were observed to localize at the positions forming fingerprint textures corresponding to the line features at the droplet interfaces. This observation is important as it highlights the critical role of the strain in directing nanoparticles with distinct surface anchoring symmetries. In addition, this observation also distinguishes the patterning mechanism of our system when compared to the examples in the literature where nanoparticle patterning was governed by the localized anchoring heterogeneities at the interfaces of LC droplets. [43,44]

Lastly, a convincing demonstration of the dependence of adsorption characteristics on elastic energy heterogeneity can be done by investigating the interfacial distribution of nanoparticles when adsorbed on CLC droplets possessing "chiral finger" structures. Thorough discussion of these structures is given in the following section. In summary, the structure is reported to consist of two different phases in a single droplet; a twisted chiral and an untwisted nematic phase dispersed in adjoining regions.[63] In this structure, we observed that in the regions far from the "fingers" (**Figure 4. 10b**, highlighted as a dashed region), the DMOAP-functionalized nanoparticles assumed a random distribution. However, near the "fingers" (**Figure 4. 10b,c**, green arrows), nanoparticles were arranged precisely at the borders of the fingers. This is independent of the nanoparticle-induced anchoring since assembly

of the same type was observed with ~100 nm -COOH silica nanoparticles ((**Figure 4. 11 d-f**).

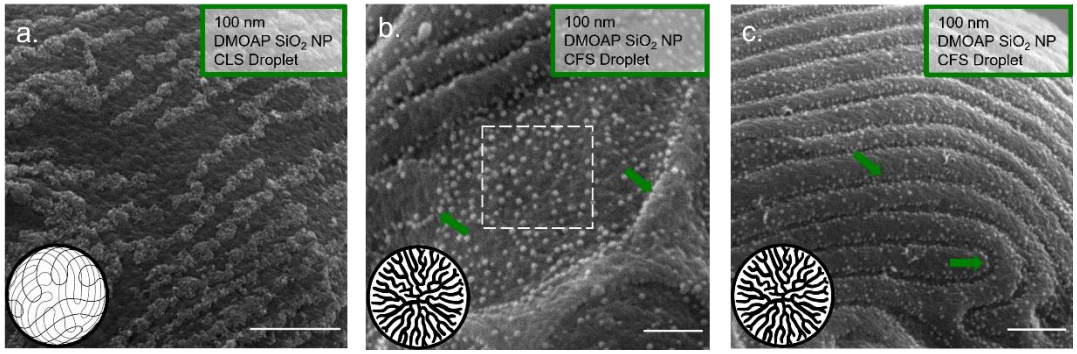

Figure 4. 10 SEM micrographs of the polymeric samples prepared from ~100 nm DMOAP silica particles adsorbed on cholesteric liquid crystal droplets with a) CLS, and b, c) "chiral finger" structures. Insets show the representative sketches of the droplet configurations. Scale bars: 1.5 μm. Droplets were prepared using a mixture of 2.5% S811, 25% RM257, and a balance 5CB by weight.

Cholesteric fingers are structures occurring in cholesteric liquid crystals under confinement with homeotropic anchoring. Under finite confinement, liquid crystals with homeotropic anchoring cannot sustain its chiral twist and the anchoring boundary conditions at the same time. If external stress is applied to them, they cannot sustain their helical twist and unwind to assume a nematic form. However, under certain confinement ratios, the elastic energy of the nematic phase become equal to the elastic energy of the cholesteric phase and a variety of structures arise. The external stress applied to achieve this phase change is usually electrical, magnetic, or mechanical.[63,64] Previously, the growth of this structure has been researched under different geometries such as sandwich cells[63,64] or W-O-W double emulsions (also known as liquid crystal shells)[43,65]. However, the processes to obtain the chiral finger structures have complex procedures. In our experiments, the methodology of preparing the droplets is very simple and only requires a simple vortex mixer with a mixing capacity of 3000 rpm. So, it is still uncertain how these structures are produced. The most plausible explanation is that during the mixing

part, some water just slips inside the CLC droplets. This explanation is plausible because; even though it is rare, the fingers are observed inside pure water, without the addition of any additives. We observed such droplet structures to be stable for more than an hour. Moreover, the number of observed finger structures, increased substantially in media with pH over 4 when -COOH silica nanoparticles are adsorbed on the surface. Hence, we believe that the adsorption of nanoparticles might have a great importance on the formation of fingers. It might be due to the anchoring boundary condition at the CLC-nanoparticle interface when the concentration of the nanoparticles is sufficient. A previous report by our group showed that the nanoparticles can induce anchoring transition on nematic LC droplets.[12] The difference in frequency of observation might be related to the aggregation of nanoparticles on the defects. The fingers might also grow because of the excess electrical charge introduced to the CLC interface by nanoparticles. While, at pH 6 -COOH SiO_2 nanoparticles are highly negatively charged, at below pH 4 it is positively charged. The increase in the negative charge at the interface might be the reason, but it does not explain the formation of fingers when DMOAP nanoparticles (which are positively charged). The formation might be promoted by the nanoparticles adsorbed on the defects that repel each other due to electric double layer forces.

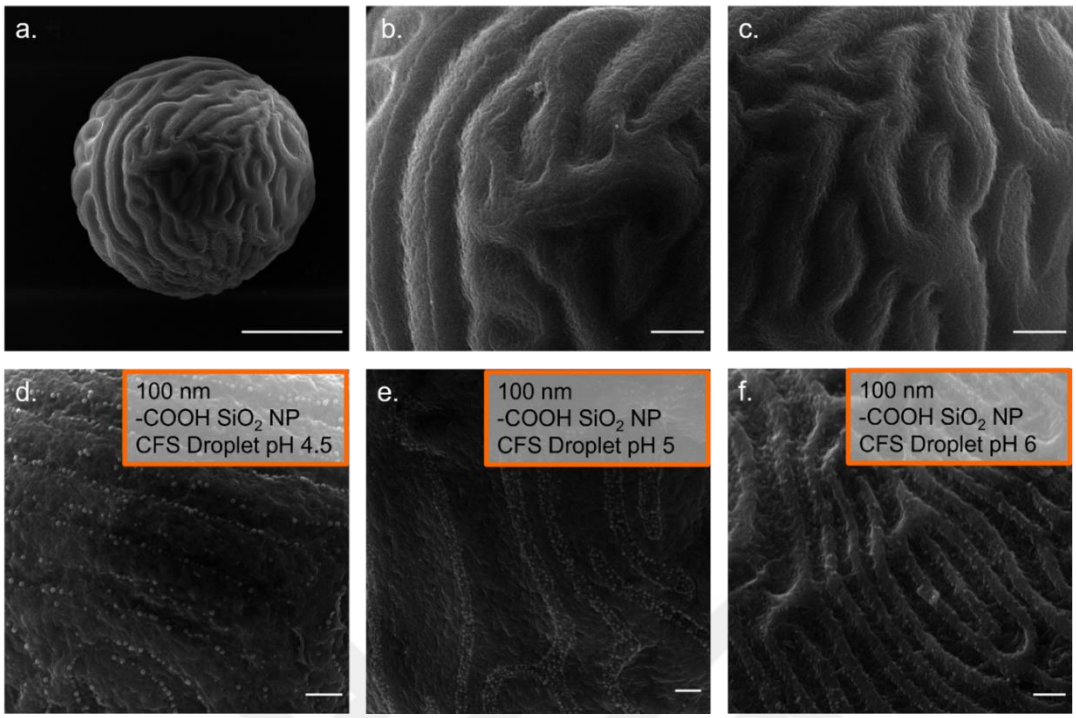

Figure 4. 11 SEM images of the CLC droplets possessing Cholesteric Fingers Structures (CFS) (a-c) with no nanoparticles added and with 100 nm sized -COOH silica nanoparticles adsorbed at d) pH= 4.5, e) pH = 5 f) pH = 6. Polymers were templated from 2.5 wt% S811, 25 wt% RM257, and balance 5CB. Scale bars a) 15 µm, b,c) 2.5 µm, (d-f) 1.5 µm.

4.4 Controlling the Assemblies by Adjusting the Elastic and Electrostatic Interactions.

We showed that an interfacial heterogeneous elastic energy landscape of the CLC droplets is a necessity for the assembly of the particles. However, as was also briefly discussed above, elastic interactions may not fully define the total interparticle interactions in this complex system. The characteristics of the formation nanoparticle assemblies at the LC interfaces are determined by multiple interactions, which we suspect to be van der Waals, electrical double layer, and elastic interactions.[51] Among these, electrical double layer interactions are usually more significant as

shown in micrometer-sized colloidal adsorbates previously.[51] Since the charging of the -COOH silica nanoparticles can be modified by varying the pH of the aqueous phase due to the dissociation of the carboxyl groups at the nanoparticle surfaces (**Figure 4. 12**),[66,67] we showed how the assemblies of the particles on the LC droplets are influenced by the charging of the nanoparticles.

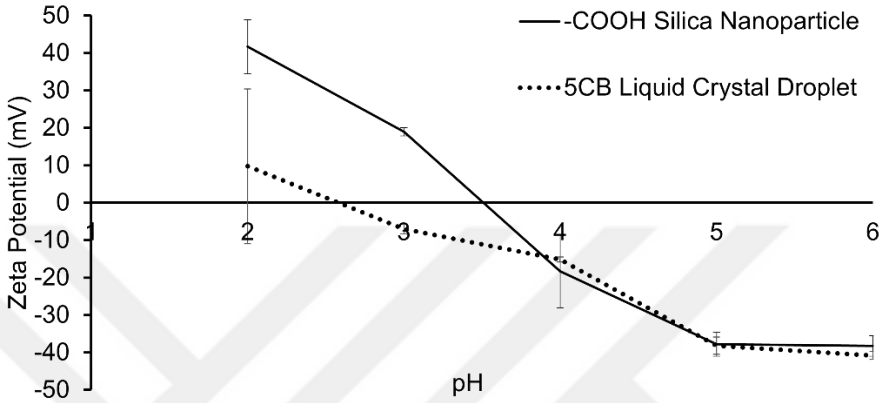

Figure 4. 12 Zeta potential of ~100 nm-sized -COOH silica nanoparticles and 5CB droplets as a function of pH of the adsorption medium

Error! Reference source not found.**a-e** shows the SEM micrographs of polymers emplated from 100 nm -COOH silica nanoparticle adsorbed CLS droplets in water with pH values between 2 to 6, respectively, **Figure 4. 13f-j** shows the polymers templated from their nematic (PRS) counterparts.

In **Figure 4. 13a,f** nanoparticle (100 nm -COOH silica) adsorption on cholesteric and nematic LC droplets dispersed in a medium of pH=2 can be seen with similar structures of similar experimental counterparts discussed above. Increasing the pH of the medium resulted in the dispersion of the nanoparticles at the CLS droplet interfaces as evident in the SEM micrographs provided in Error! Reference source ot found.**a-e**. In pH=2-4 medium (**Figure 4. 12 a-c**), the nanoparticles at CLS droplet interfaces were observed to maintain cholesteric fingerprint assemblies. However, increasing the pH above 4 resulted in the separation of the nanoparticles and led to

their almost uniform distribution at the interface when pH=6, resulting in the destruction of the fingerprint patterns (although the careful investigation still reveals a minority of the particles to position on the defects due to elastic attractions). On nematic droplets in pH=3 medium (Error! Reference source not found.**g**), nanoparticles were observed to form "patches" with separated nanoparticle aggregates. Increasing the pH of the medium over this range resulted in the singular dispersion of the nanoparticles at the interfaces of the nematic droplets, which was possibly enabled by the significant electrostatic repulsion to overcome the attractive interparticle forces (**Figure 4. 13c-e, h-j**)

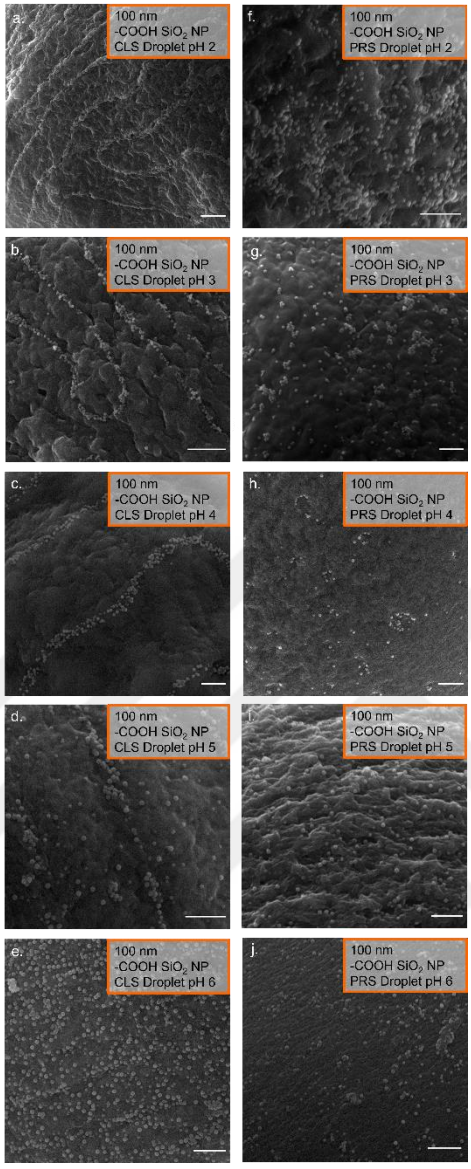

Figure 4. 13 a-e) SEM micrographs of polymers templated from ~100 nm -COOH silica nanoparticle adsorbed CLC droplets (CLS) in mediums of pH=2 to 6, respectively. f-i) SEM micrographs of polymers templated from ~100 nm -COOH silica nanoparticle adsorbed nematic droplets (PRS) in mediums of pH=2 to 6, respectively. Polymers were templated from 2.5 wt% S811, 25 wt% RM257, and balance 5CB. Scale bars: 1.5 µm.

These observations showed the significance of the electrical double layer interactions on the formation of the fingerprint assemblies of the nanoparticles at droplet interfaces. However, the results do not readily explain the assembly characteristics of the nanoparticles. More specifically, the measurements of the zeta potential of the nanoparticles at pH=2 and 3 revealed a significant charging of the nanoparticles which were measured to be +42 ± 7 mV and +19 ± 1 mV, respectively. Such potentials would in general be expected to result in the dispersion of the nanoparticles, however, such was not the case in our experimental observations. Instead, we observed a significant aggregation (and also patterning) of nanoparticles at droplet interfaces, although different average separations between the nanoparticles were also observed **(Figure 4. 14**).

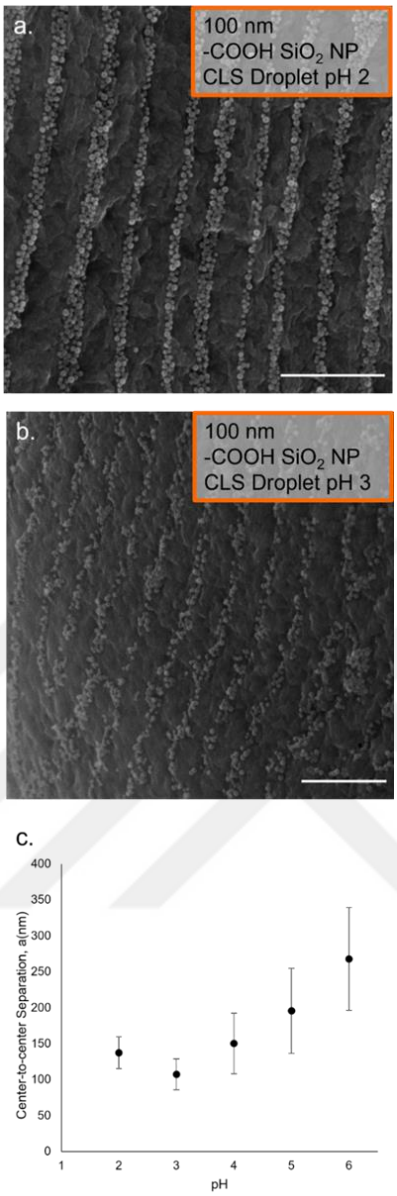

Figure 4. 14 a) Adsorption of nanoparticles on a droplet with CLS configuration in medium with pH value 2. b) Adsorption of nanoparticles on a droplet with CLS configuration in medium with pH value 3. c) Center-to-center separation measurements of nanoparticles adsorbed at a CLC-water interface with different pH values. Polymers were templated from a 2.5 wt% 25 wt% RM257, and balance 5CB. Scale bars: 2.5 μm.

On the other hand, with similar magnitudes but opposite zeta potentials at pH=5 and 6 (-38 ± 3 mV and -39 ± 3 mV, respectively) than pH=2 medium, we observed dispersion of the nanoparticles at the interfaces of the droplets. We hypothesized that this result was due to the screening of the electrostatic repulsions by the partitioned negatively charged ions at the interfaces of the droplets, which we discuss in more detail in the next section along with the modeling of the nanoparticle interactions. We have recently reported that the pH of the medium does not affect the nematic LC in a previous study.[12] To observe whether the ionic strength of the medium affects the anchoring of the LC, and hence changes the assembly characteristics in our system, we observed the configuration distribution of nematic LC droplets mixed with reactive mesogen. In our system, we emulsified the droplets in mediums with different pH and equilibrated them for 1h. After 1h, the droplets are polymerized with UV light and observed with polarized optical microscopy. The configuration distribution presented in **Figure 4. 15**, clearly shows that medium pH does not have a strong effect on the anchoring of LC.

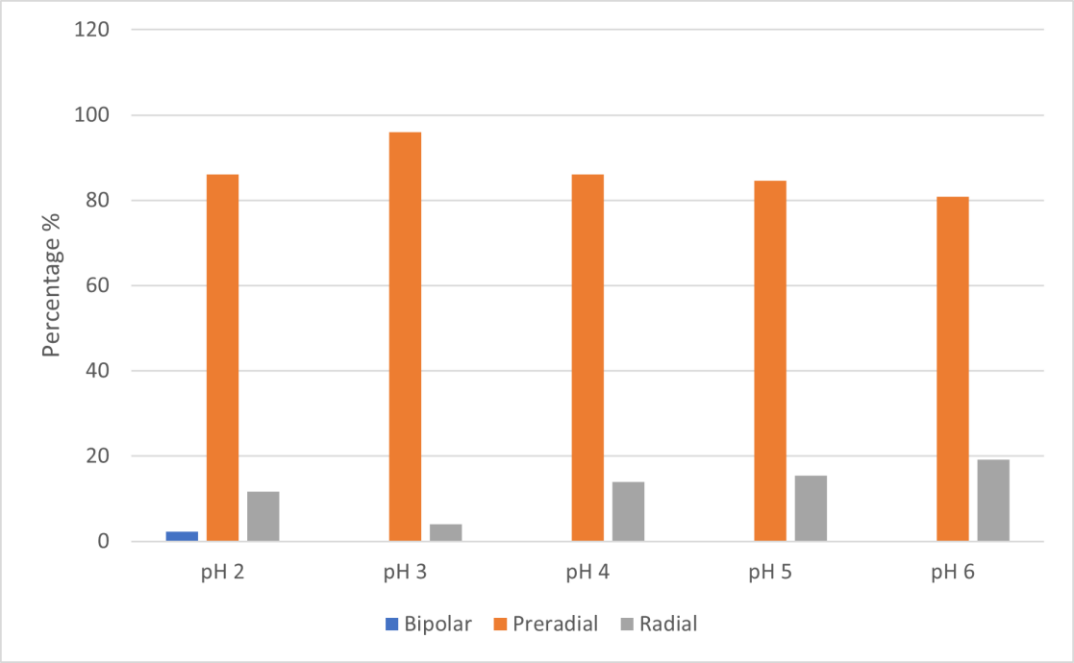

Figure 4. 15 The effect of pH on the LC anchoring is presented. In this experiment, nematic LC reactive mesogen mixtures are emulsified in mediums with different pH. Droplets are prepared by vortex mixing and equilibrated for 1h. After equilibration, reactive mesogens are polymerized with UV light and observed with POM. Because of the reactive mesogen in the mixture, the dominant LC anchoring is observed to be tilted. No significant change is observed with different mediums. The mixture consists of 25 wt% RM257, and balance 5CB.

The formation of the interfacial assemblies on defects was not limited to ~100 nm-sized particles. **Figure 4. 16a,b** shows the SEM images of the polymers synthesized from ~50 nm and ~500 nm average-sized nanoparticles-adsorbed CLS droplets, respectively. In a medium of pH=3, ~50 nm-sized particles were positioned on the defects after equilibration for 1h. It was observed that some of the particles formed aggregates with sizes ranging between 100-500 nm (shown with arrows) though singly dispersed particles were also present on the defects. For ~500 nm particles on CLS droplets, we observed the formation of the colloidal fingerprint aggregates. However, considering the results presented in **Figure 4. 5d-f** along with the

hexagonal packing of the nanoparticle aggregates evident in **Figure 4. 16b**, we concluded that the elastic interactions induced by the ~500 nm-sized particles were significant in the assembly characteristics of the nanoparticle aggregates. Such symmetry was not present in the interfacial assemblies formed either by ~50 nm or ~100 nm-sized nanoparticles. This conclusion was also revisited in the next section on the modeling of nanoparticle interactions.

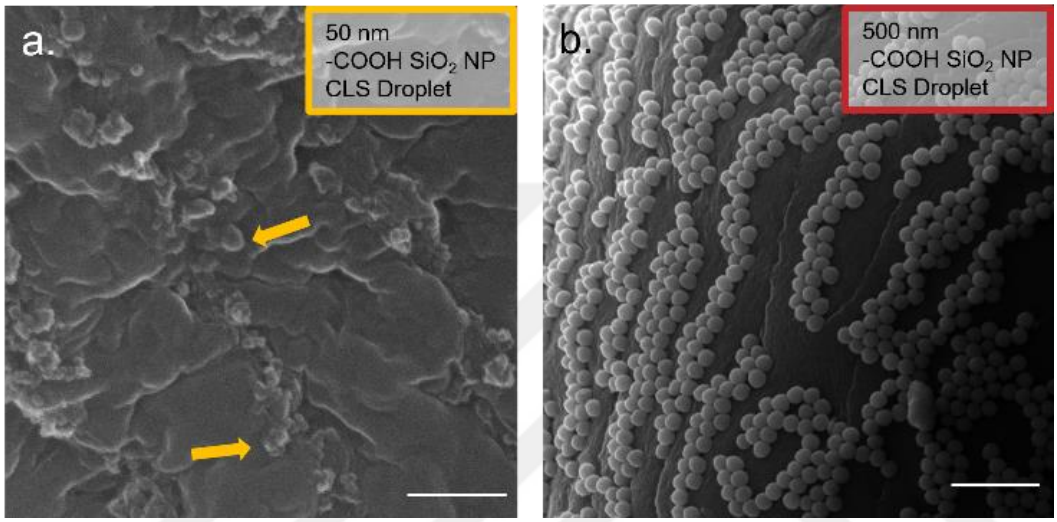

Figure 4. 16 SEM micrographs of the polymers synthesized from a) ~50 nm and b) ~500 nm-sized -COOH silica nanoparticle-adsorbed CLS droplets in a medium with pH=3. Polymers were templated from 2.5% S811, 25% RM257, and balance 5CB by weight. Scale bars: a) 0.5 µm, b) 2.5 µm.

4.5 Modeling the Assemblies

To provide insight into the assembly characteristics of the particles at defects, we modeled the interactions by calculating the binary energy of interaction between two nanoparticles, one of which is located on the defect. In this calculation, four different energy contributors were taken into account which were elastic attraction exerted by the defect, elastic interaction between two nanoparticles caused by elastic deformations on the LC (the so-called quadrupolar-quadrupolar interactions), the

van der Waals interactions, and the electric double layer interactions of the nanoparticles. Thus, the total can be written as;

$$E_{total} = E_{splay} + E_{quadrupolar} + E_{vdW} + E_{EDL} \quad \text{Equation 1}$$

The attractive splay energy exerted on the nanoparticles by the defect is given by;[51]

$$E_{splay} = -\frac{8}{3}\pi K \frac{a^3}{d^2} \quad \text{Equation 2}$$

where K is the splay elastic constant estimated as K = 6.4 pN, [68] a is the radius of the nanoparticles and d is the center-to-center distance between the two particles one of which is located on the defect. The quadrupolar interaction energy caused by the elastic strain induced by nanoparticles at the homeotropic LC-water interface is given by;[59,69]

$$E_{quadrupolar} = \frac{4\pi K a^4}{d^3} \quad \text{Equation 3}$$

The equation used for the van der Waals (*vdW*) interaction energy is; [70]

$$E_{vdW} = -\frac{H}{12d} a \quad \text{Equation 4}$$

where H is the Hamaker constant for silica nanoparticles which is 2.1 $\times 10^{-21}$ J.[71] Lastly, the electrical double layer (*EDL*) interaction energy contribution to the interaction between the two particles at the water-oil interface is used as,[51,72]

$$E_{EDL} = \frac{2\varepsilon_{5CB}\pi\alpha_w^2\sigma^2 a^2 \sin^2\gamma}{\varepsilon_0\varepsilon_w^2\kappa^4 d^4} \quad \text{Equation 5}$$

where ε_{5CB} is the dielectric constant of 5CB used as 11,[51] α_w is the degree of dissociation of the carboxyl groups at the surface and it was calculated separately for each pH, γ is the contact angle at the 5CB-water interface (estimated as 90°), ε_w is the dielectric constant of water (78), κ is the Debye Hückel parameter, and σ is the surface charge density of the nanoparticles calculated with;[51]

$$\sigma = \frac{2\varepsilon_0\varepsilon_w k_B T \kappa}{ze} \sinh\left(\frac{ze\zeta}{2k_B T}\right)\left[1 + \frac{1}{\kappa a \cosh^2\left(\frac{ze\zeta}{4kT}\right)}\right] \qquad \text{Equation 6}$$

where the unit of σ is Cm^{-2}. ε_0 is the permittivity of the vacuum, T is the temperature (298 K), k_B is the Boltzmann constant, z is the valence number of the ions, e is the electronic charge, and ζ is the zeta potential (measured).[51] The equation for the Debye-Hückel parameter was;[70]

$$\kappa = \sqrt{\frac{2\rho_\infty e^2}{\varepsilon_0\varepsilon_w k_B T}} \qquad \text{Equation 7}$$

the ρ_∞ is the number density of the ions in the bulk medium, and e is the electric charge. MATHCAD script used for calculation of the electrostatic interaction terms is presented in **Appendix C.**

Each energy term in Equation 1 was calculated separately and plotted with respect to center-to-center separation between particles, where a representative calculation for pH=5 is given in **Figure 4. 17a** and for other pHs in **Appendix D**. In this case, the attractive van der Waals term was relatively insignificant compared to the other energy contributors. Since the magnitudes of attractive energy of the defect and the repulsion of the electrical double layer and repulsive elastic energy were close to each other, the calculated total interaction energy minimum on the nanoparticle was close to a few k_BT (≈7 k_BT at ~200 nm separation) as shown in **Figure 4. 17b** (for pH=5). This result indicates a reversible interaction of the particles with those that are located at the defects. This result is important as it is consistent with our experimental observations where we observed a distribution of the particles free from the defects at pH=5 (**Figure 4. 13**).

Figure 4. 17b shows that the total interaction energy between particles is strongly dependent on the medium pH. The calculations suggested that at pH≤4, the attraction of the defect dominated the electrostatic repulsion. An energy minimum in the order of ≈40 k_BT was calculated in this range, which explained the finely defined patterns

with the absence of the particles freed from defects (see Figure 4b-d for equivalent experiments). We hypothesize this observation to result from the screening of the electrostatic interactions with the higher ionic strength at low pH. However, the model does not predict well the experimentally observed difference between the assemblies formed at pH=2 and pH=3 medium, where the SEM images clearly showed that the nanoparticles were more prone to aggregation in a medium of pH=3 compared to their more uniform thickness in pH=2 (**Figure 4. 14**). We speculate that this difference in the nanoparticle structuring at defects results from three contributors. First is the elastic repulsive force due to strain caused by nanoparticles that we estimated using Eqn. 3, which were adopted from the studies where micrometer-sized colloidal particles were used. With such adoption, the influence of the competition of elasticity and surface anchoring was not incorporated accurately. Second, the line defects in CLS droplets are located at the sub-interface and the nanoparticles may not be positioned within the defects. Thus, the calculations may include a variation in the exact estimation of the elastic interactions. The third and possibly more significant effect would be the ion partitioning and the influence of the pH-dependent charging at the LC-water interface.[73–75] Specifically, our measurements, consistent with the literature, revealed that the charging at the LC-water interface shifted towards positive values as the pH of the medium was decreased to 2 (**Figure 4. 12**). This positive interfacial charging may result in a loss of the magnitudes of the screening of the electrostatic interactions of the positively charged -COOH silica particles at pH=2 that may result in a repulsive barrier when the particles were close to each other. The ion partitioning is also consistent with the aggregation characteristics of DMOAP silica particles on the interface of the CLC droplets although they possess significant charging.[12]

At higher pH, our model revealed the dominancy of the repulsive forces that resulted in >10 $k_B T$ of repulsive energy even up to 600 nm of separation. This calculation explained our experimental observation of the interfacial dispersion and the absence of a significant patterning of the nanoparticles in the mediums with pH>5.

Figure 4. 17c shows the effect of the particle size on the assembling. In the model, total interaction energy on particles with sizes 50 nm, 100 nm, and 500 nm were calculated in a pH=3 solution, in which the experiments were conducted in **Figure 4. 16** and **Figure 4. 16**. All the interactions in the calculations were affected by the particle size substantially. Our calculations showed that the electrostatic repulsions increased with the decreasing particle size whereas all the elastic effects decreased because the elastic attractions scale with a third-order polynomial dependency of the radius whereas electrostatic repulsion scales with a second-order. However, in each size, the significance of the electrostatic effects was diminished by the strong ionic medium at pH=3. Furthermore, the quadrupolar-quadrupolar interaction energy and the elastic defect attraction were substantially increased for 500 nm nanoparticles which was expected since we know that the distortion created by the 500 nm nanoparticles is apparent even under optical microscopy (**Figure 4. 5d-f**). The deep energy minimum at ~100 nm separation indicates the positioning of particles at defects, which we observed for both the high and low nanoparticle concentrations.

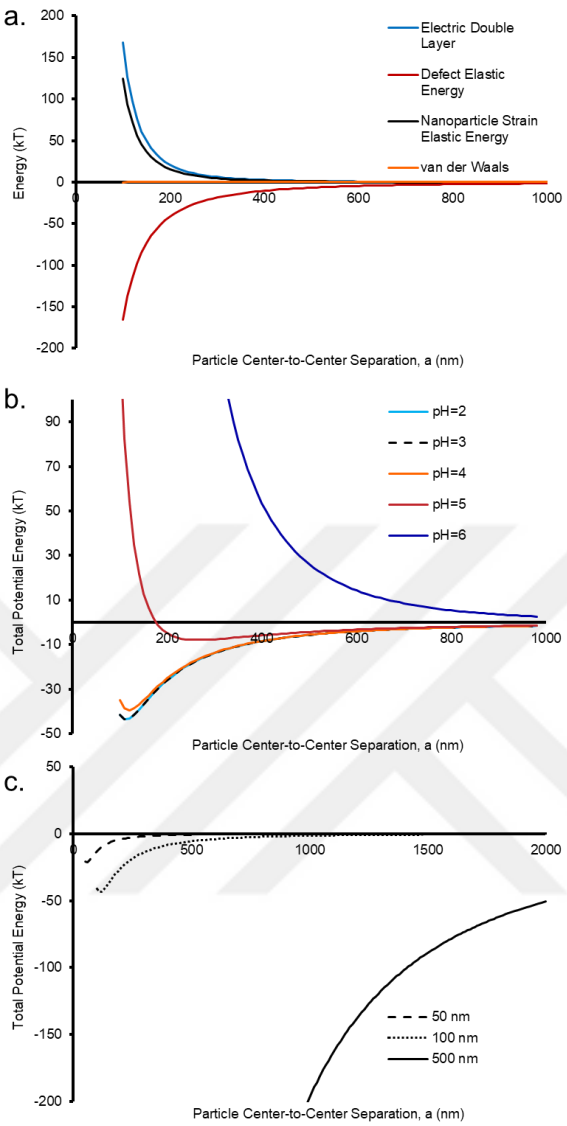

Figure 4. 17 a) Calculated individual contributors of the total energy indicated in Equation 1 as a function of the center-to-center separation of the particles at the interface. Calculations were performed for ~100 nm particles at pH=5. b) Calculated total energies as a function of center-to-center separation at different pH values. c) Calculated interaction energies of particles of sizes 50, 100 to 500 nm at pH=3. The calculated energy values were normalized to k_BT to compare them with thermal energy.

It is important to note that the model is very rough, and it does not explain every characteristic of the assembly completely but accounts for the general trends of our experimental observations as mentioned above. In the last part of the study, we discuss the control experiments and additional support experiments for the predictions we made in the above calculations. As a control experiment to completely screen the electrostatic interactions, 100 mM NaCl was added to the medium. Zeta potential measurements of 100 nm -COOH nanoparticles is given in **Table 4. 2.** Value of the zate potential gradually decreased with increasing NaCl concentration. Total screening of the electric-double layer is observed as the salt concentration reached to 100 mM.

Table 4. 2 Zeta potential measurements of 100 nm -COOH nanoparticles in different pH and NaCl salt concentrations

	Zeta Potential	
NaCl Salt Concentration	**Medium pH**	
	pH 2	pH 6
0 mM	29.3 mV	-37.6 mV
1 mM	23.8 mV	-31.6 mV
10 mM	17.2 mV	-26.1 mV
100 mM	-	-

In the experiments shown in **Figure 4. 18**a, nanoparticles were initially adsorbed on the CLC droplet surface at pH=6. In this condition, where the images are shown on the left, particles in the dispersed phase were observed which was due to the large electrostatic barrier. The addition of 100 mM NaCl to the medium screened the

electrostatic double layer and eliminated the electrostatic repulsion, which resulted in the formation of the patterned assemblies on the defects even at pH=6 (**Figure 4. 18a**, right). In this case, we also observed the particles that were not close to defects to assemble into random clusters away from the defects, as an indication of the screening of the electrostatic interactions. On the other hand, the particle assemblies in the medium of pH=2 were only slightly changed with changing ionic strength. Specifically, **Figure 4. 18b** (left) shows the experiment conducted at pH=2, where the nanoparticles formed lines with similar thickness when the defects were saturated. When the adsorption was performed in 100 mM NaCl and pH=2, we did not observe a significant change in the final assembly characteristics of the nanoparticles, but the uniformity of the thickness was slightly influenced negatively (**Figure 4. 18b**, right). The effect of salt was not as significant as in the case of pH=6 because the electrostatic double layer of the nanoparticles in the pH=2 solution was already compressed.

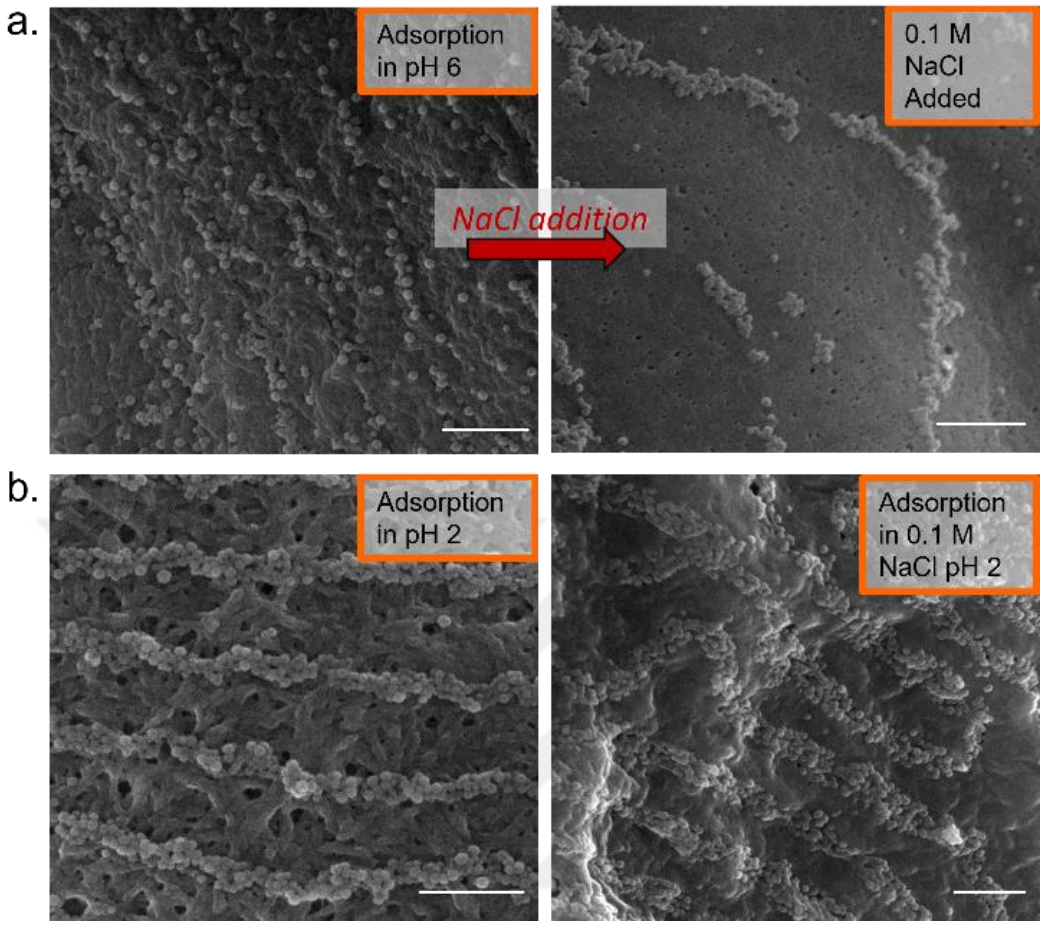

Figure 4. 18 a) SEM images of the polymerized CLS droplets before (left) and after (right) the addition of 100 mM NaCl at pH=6. NaCl was added to the emulsions after 1 h of equilibration and polymerized after an additional 1 h of equilibration and imaged. b) SEM images of the polymerized CLS droplets at pH=2 without (left) and with (right) the presence of 100 mM NaCl. Polymers were templated from 2.5% S811, 25% RM257, and balance 5CB by weight. Scale bars: 1.5 μm

The model on the interaction of -COOH silica nanoparticles was confirmed by experimental estimation of the local minima in the interaction energy. The particle distribution observed in experiments allowed us to calculate the total interaction energy of particles by using Boltzmann Distribution. The Boltzmann equation that relates the particle probability to the particle potential is given in Equation 8. For the Boltzmann equation it is assumed that the particle concentration is constant, they are

classical particles and all the particles are in thermal equilibrium with each other. Φ_m is the probability of finding a particle at a reference point, ϕ is the probability of finding a particle at the position x. ψ(x) is the potential energy of the particle at the position x and $\psi(x_m)$ is the potential energy of a particle at the reference point, T is the temperature, k_B is the Boltzmann constant.[76–78]

$$\frac{\Psi(x) - \Psi(x_m)}{k_B T} = \ln\left(\frac{\Phi_m}{\Phi}\right) \qquad \text{Equation 8}$$

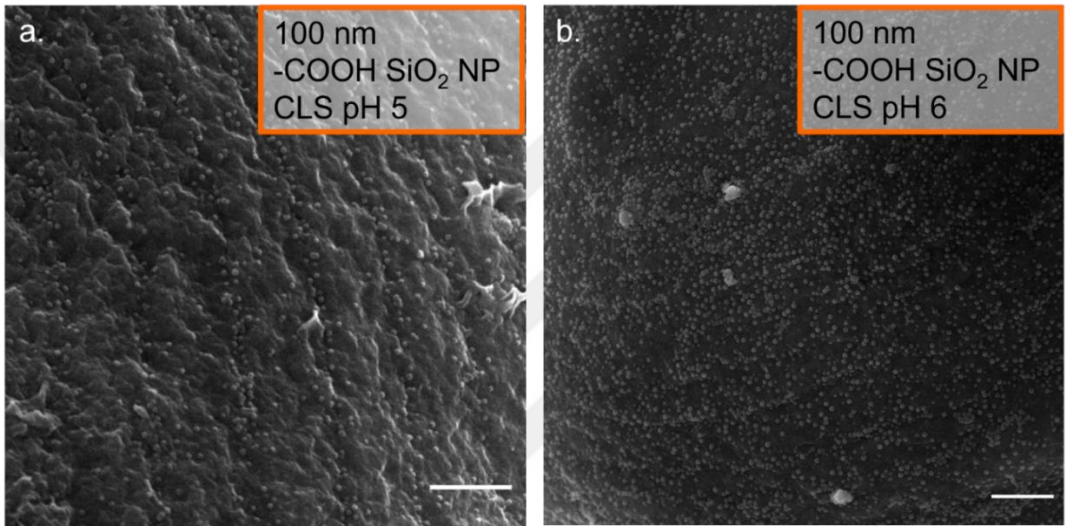

Figure 4. 19 100 nm -COOH silica Nanoparticle Adsorption on the Surface of a CLC Droplet inside a) pH=5 b) pH=6. Polymers were templated from 2.5 wt% S811, 25 wt% RM257, and balance 5CB. Scale bars: 2.5 μm.

The equilibrium distribution can be related to the potential energy of the particles *via* the Boltzmann Equation.[20] **Figure 4. 20a** shows the probability distribution of the nanoparticles on CLS droplets at pH=5 and 6. A disclination center was chosen to be the reference point (x=0) and the droplet interface was separated into 200 nm-wide "bins". The minimum distance between the center of the particle and the defect was measured from SEM micrographs (**Figure 4. 19**) and distribution was obtained to calculate the probability of finding a particle in each "bin". In **Figure 4. 20a**, the localization of the nanoparticles at defects is evident (shown with dark arrows) for

pH=5 whereas the dispersion is seen in the pH=6 case. When interaction energies were calculated based on these distributions using the Boltzmann equation, an energy well around ≈3 k_BT was present at the defect positions in pH=5 (**Figure 4. 20**b,) which was comparable to the thermal energy, and more importantly, supporting the calculations done in **Figure 4. 17b** where we found the interaction energy for pH=5 as ≈7 k_BT. The depth of the wells can also be tuned by adjusting the charging of the particles (hence changing the electrostatic repulsion). **Figure 4. 20a** also shows the probability distribution of particles adsorbed on a CLC in a pH=6 medium. The probability distribution in pH=6 medium suggests that the concentration of the particles present at the defects is not different from the concentration of the particles away from the defects. No preferential positioning was present due to the strong repulsive barrier, which is in favor of the scattered phase of the nanoparticles revealing an average total interaction energy less than k_BT, supporting our calculations. Lastly, **Figure 4. 20a** shows the probability distribution of the particles at pH=4, where there is a sharp increase in the probability at the defect locations. The probability distribution for pH=4 suggests an energy that is significantly larger than k_BT. This result coincides with our calculations in **Figure 4. 17**, where the energy well is calculated to be much larger than k_BT, and also our observations in **Figure 4. 12** where particles specifically located on defects below pH=4

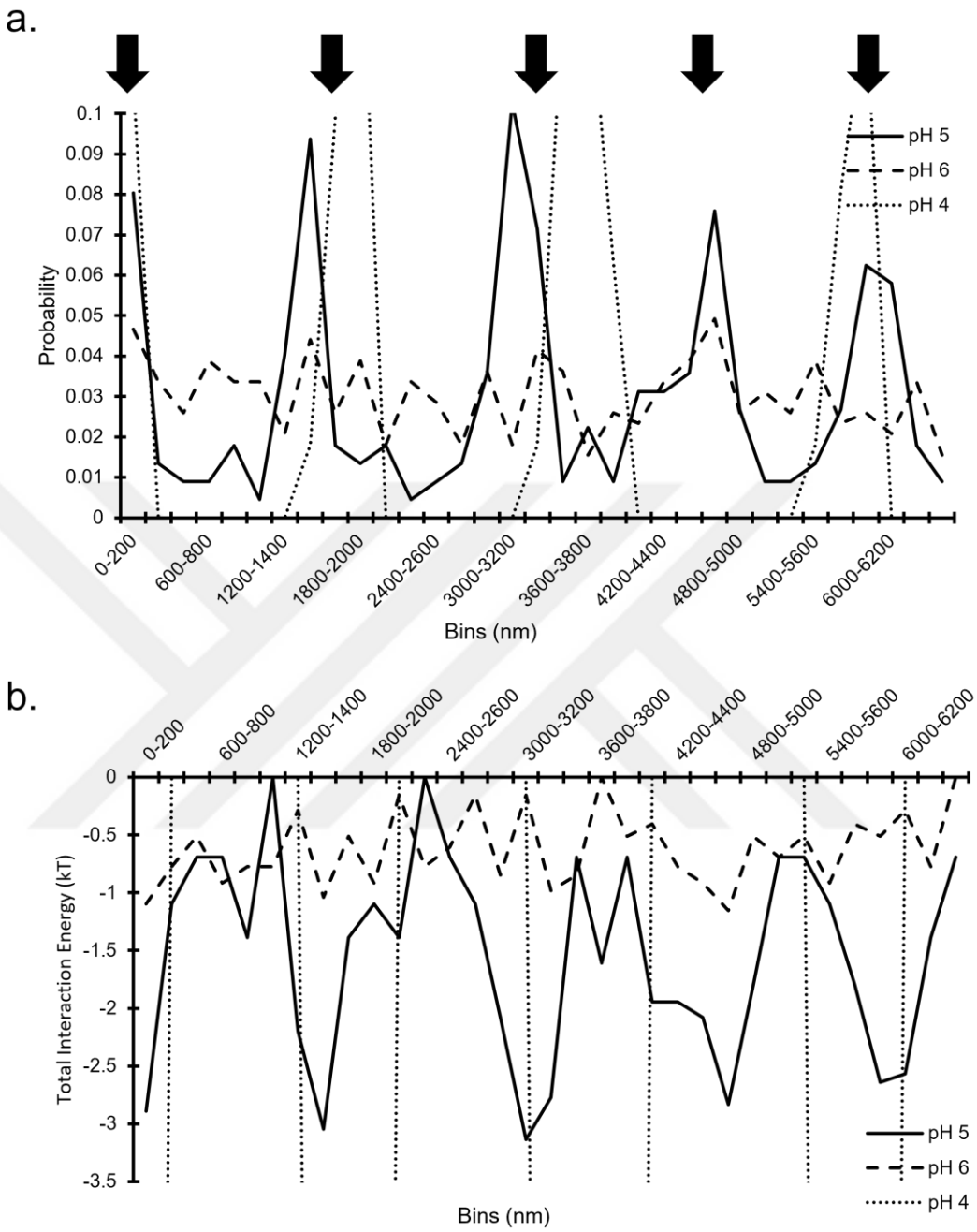

Figure 4. 20 a) Probability plot of finding a nanoparticle at a distance away from the defect for pH=4, pH=5, and pH=6. b) The total interaction energy is calculated from the probability distributions for pH=4, pH=5, and pH=6.

4.6 Patterning of CLCs Confined in Different Geometries

The patterning of the CLC-aqueous interface is not limited to the spherical confinements. To test the patterning in different geometries we investigated the liquid crystal films. **Figure 4. 21a,b** shows the brightfield and polarized optical microscopy images of the CLC films placed in 20 μm gold electron microscopy grids supported on DMOAP functionalized glass slides. DMOAP functionalized glass slides induce homeotropic anchoring on the bottom face of the CLC. <0.5 μL is deposited on the film. To achieve homogeneous thickness across the grid, excess CLC is removed from the top with a micropipette. Glass slide is inserted into a cuvette that is filled with water with desired pH. The DMOAP-functionalized glass slide is hydrophobic, so the film and the CLC inside it stay intact during the insertion of the film and CLC. The CLC is equilibrated for 1h, to minimize the effects of shear that occurred during the insertion. After 1h, 100 nm -COOH nanoparticles are introduced into the system. However, in these systems, we observed that the nanoparticle concentration should be increased at least 100 times compared to the emulsions. The reason is that 100 nm nanoparticles do not precipitate and are left hanging in the medium. The emulsions receive more contact with the particles whereas, films located at the bottom of the cuvette do not receive as much. After equilibrating the system again for the particles to locate and position on the defects, reactive mesogens are polymerized with 365 nm UV light for 10 min. The system was rinsed at least 10 times with fresh continuous phase to remove the excess nanoparticles and 4 times to remove the CLC. Brightfield and polarized images of the polymeric film are presented in **Figure 4. 21c,d**. SEM imaging of the films showed that the polymers templated from mixtures of CLC with 25 v% reactive mesogens rupture during the shrinking. To reduce the amount of shrinking, the concentration of the reactive mesogen is increased to 30 v%.

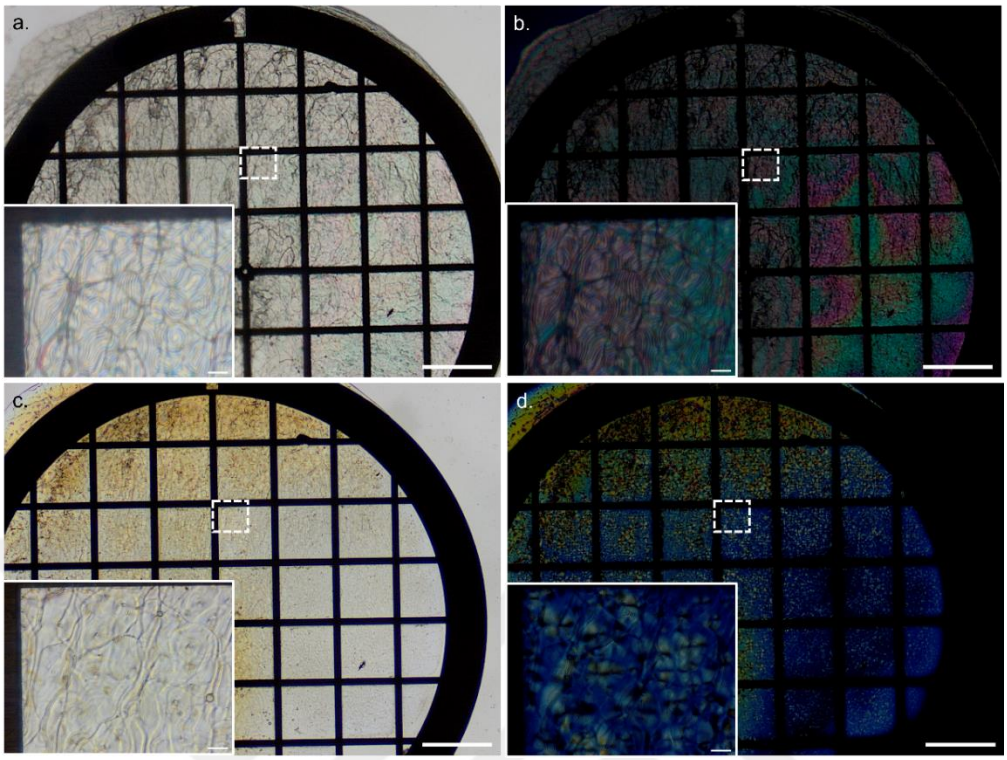

Figure 4. 21 Cholesteric liquid crystals confined in 20 μm thick gold electron microscopy grids supported on DMOAP-coated glasses. a) Brightfield and b) Polarized optical microscopy images of the CLC film just after the addition of the nanoparticles into the system (Scale Bar is 200 μm). Close-up images of the dashed area is given in the left bottom corner of the images (Scale Bar is 10 μm). c) Brightfield and d) polarized optical microscopy images of the films after the polymerization of the reactive mesogens and extraction of liquid crystals. (system (Scale Bar is 200 μm). Close-up images of the dashed area are given in the left bottom corner of the images (Scale Bar is 10 μm). Polymers were templated from 2.5 wt% S811, 30 wt% RM257, and balance 5CB. Medium pH=3.

SEM images of the films that are equilibrated for 2h 3 min after nanoparticle addition are presented in

Figure 4. 22. In pH=2, a high amount of nanoparticle adsorption is observed in the surfaces of the polymers. Nanoparticles completely covered the surface of the polymers. The most plausible explanation for this case is the high ionic strength of

the particles screen the electrostatic repulsion and particles easily adsorbed to the interface (

Figure 4. 22a). When the medium pH is increased to pH=3, fingerprint patterns, that are characteristic of cholesterics) are observed. An example of the complex patterns generated is presented in

Figure 4. 22b. As the pH of the system increased over pH=4, no particles are observed on the surfaces of the films (

Figure 4. 22c,d). Yet again, the electrostatic repulsion (in this case not screened enough) had probably kept the nanoparticles away from the interface.

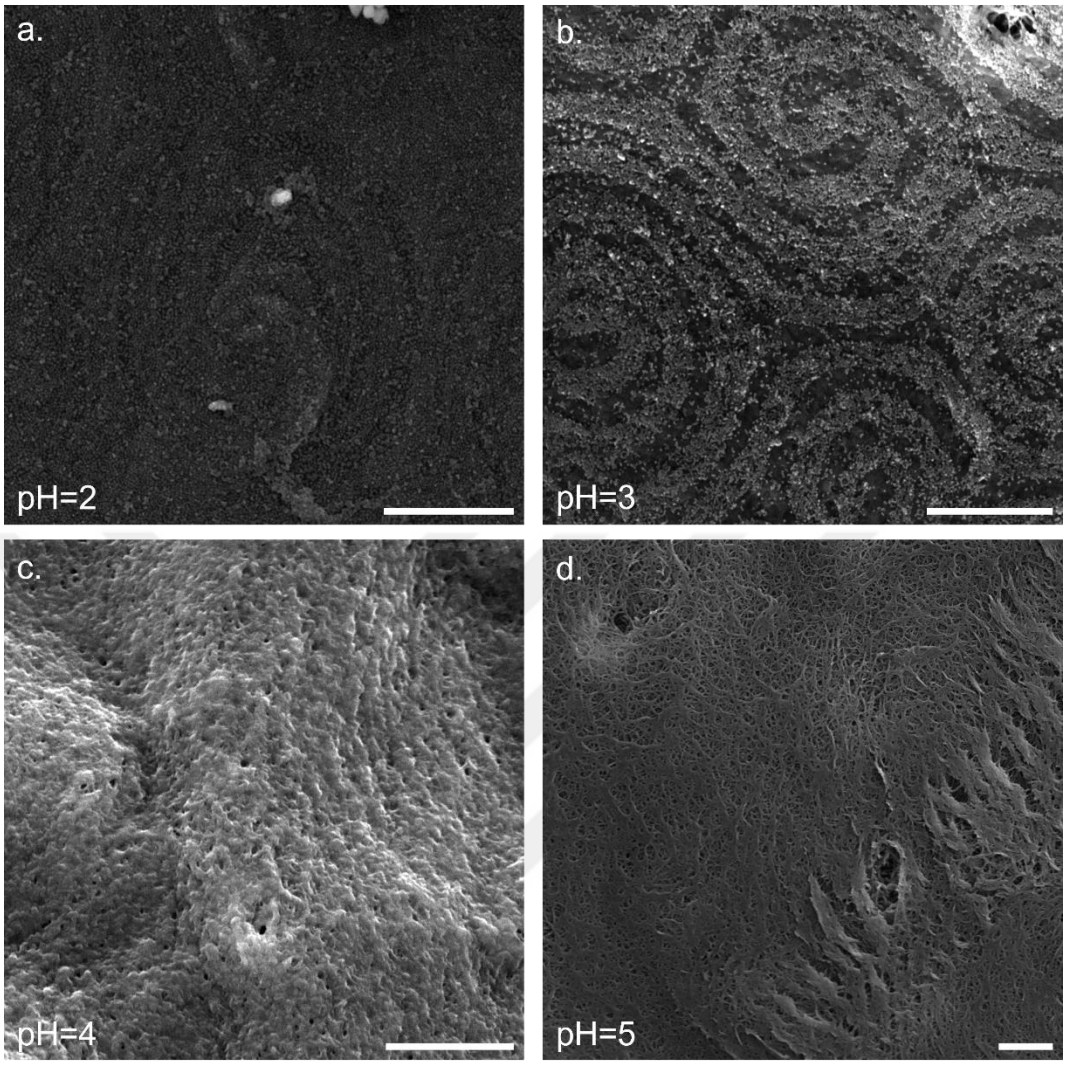

Figure 4. 22 SEM imaging of the polymeric films templated from the CLC films in different mediums. a) pH=2, b) pH=3, c) pH=4, d) pH=5. The systems are equilibrated for 2h and 30 min after 100 nm -COOH NP addition. Polymers were templated from 2.5 wt% S811, 30 wt% RM257, and balance 5CB. Scale Bars: 5 μm.

We also observed that the curvature of the patterns formed also differs in regions with different thicknesses. This suggests that the shapes of the patterns depend on the ratio of the size of the confinement and the pitch size of the cholesteric liquid crystal. To investigate the effect of chiral confinement on the curvature of the patterns, we observed films templated from CLCs with different chiral dopant

concentrations. SEM imaging of the films is presented in **Figure 4. 23**. When the chiral dopant concentration is increased to 5 wt% the pitch size of the chiral twist is measured to be ~ 1.8 μm. SEM images of the films that are templated from CLC with 5 wt% S811, the distance between the patterns are measured to be ~ 800 nm which is close to the half-pitch. In this case, we observed that the patterns complete multiple turns around a center to form concentric circles (**Figure 4. 23a**). As the pitch size increased with the decreasing chiral dopant concentration, the circles started to flatten (**Figure 4. 23b**). When the chiral dopant concentration is decreased to 1.4 wt%, straight lines with lengths in the scale of millimeters(with a thickness in the range of nanometers) are formed. In this case, the two lines that are in the vicinity of each other are always separated by a distance of ~ 5 μm (**Figure 4. 23c**). Hence, it is understood that the separation and the curvature of the lines can be changed by changing either the cell thickness or the chiral pitch.

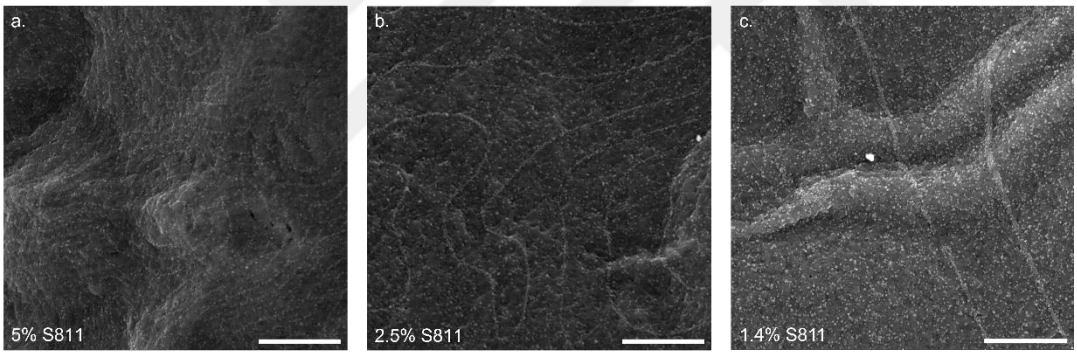

Figure 4. 23 SEM imaging of the polymeric films templated from the CLC films with different chiral dopant concentrations. Polymers were templated from a) 5 wt%, b)2.5 wt%, c) 1.4 wt%, S811, 30 wt% RM257, and balance 5CB. Scale Bars: 5 μm. Medium pH=2

CHAPTER 5

CONCLUSION

We experimentally investigated the assembly of the nanoparticles at interfaces mediating elastic interactions. Our experimental findings were consistent with our calculations based on the energy of interparticle interactions. Specifically, we found the elastic interactions caused by strained interfaces and particles, and electrical double layer forces were the key, dominant interactions between the particles, the tuning of which resulted in the formation of fingerprint assemblies dictated by the sub-interface defects of the cholesteric liquid crystal droplets. These findings also revealed the importance of ion partitioning at the oil-water interfaces on nanoparticle interactions.Thus, the nanoparticle structuring reported herein was shown to successfully probe the energetical and chemical heterogeneities at the interfaces highlighting the impact of the findings in two potential fields. First, the nanoparticles in assemblies in this work could be enriched in multiple sizes and materials (metallic, polymeric, conductive, magnetic or optically active among others) that could be used further as the basis for the hierarchical assembly of more complex, composite structures with added functionality. Second, the dependency of the nanoparticle assemblies on the fine interfacial details can further be employed to probe the nanoscopic structuring at the interfaces. Thus, future studies can be devoted to designing functional materials that can be employed in sensors, photonics, and electronic devices as well as multifunctional materials towards integrated or intensified chemical handling approaches.

REFERENCES

1. Qi, F., Meng, Z., Xue, M. & Qiu, L. Recent advances in self-assemblies and sensing applications of colloidal photonic crystals. *Anal Chim Acta* **1123**, 91–112 (2020).

2. Wang, K. *et al.* Self-Assembled Colloidal Nanopatterns toward Unnatural Optical Meta-Materials. *Adv Funct Mater* **31**, 2008246 (2021).

3. Liu, M. *et al.* Colloidal quantum dot electronics. *Nature Electronics* vol. 4 548–558 Preprint at https://doi.org/10.1038/s41928-021-00632-7 (2021).

4. Li, Z., Fan, Q. & Yin, Y. Colloidal Self-Assembly Approaches to Smart Nanostructured Materials. *Chemical Reviews* vol. 122 4976–5067 Preprint at https://doi.org/10.1021/acs.chemrev.1c00482 (2022).

5. Dijkstra, M. & Luijten, E. From predictive modelling to machine learning and reverse engineering of colloidal self-assembly. *Nature Materials* vol. 20 762–773 Preprint at https://doi.org/10.1038/s41563-021-01014-2 (2021).

6. Ai, B., Möhwald, H., Wang, D. & Zhang, G. Advanced Colloidal Lithography Beyond Surface Patterning. *Advanced Materials Interfaces* vol. 4 1600271 Preprint at https://doi.org/10.1002/admi.201600271 (2017).

7. McGorty, R., Fung, J., Kaz, D. & Manoharan, V. N. Colloidal self-assembly at an interface. *Materials Today* vol. 13 34–42 Preprint at https://doi.org/10.1016/S1369-7021(10)70107-3 (2010).

8. van Dommelen, R., Fanzio, P. & Sasso, L. Surface self-assembly of colloidal crystals for micro- and nano-patterning. *Advances in Colloid and Interface Science* vol. 251 97–114 Preprint at https://doi.org/10.1016/j.cis.2017.10.007 (2018).

9. Khazaei, M. A., Bastani, D., Mohammadi, A. & Kordzadeh, A. Adsorption Dynamics of Surface-Modified Silica Nanoparticles at Solid–Liquid Interfaces. *Langmuir* **38**, 12421–12431 (2022).

10. Bukusoglu, E., Pantoja, M. B., Mushenheim, P. C., Wang, X. & Abbott, N. L. Design of Responsive and Active (Soft) Materials Using Liquid Crystals. *Annu Rev Chem Biomol Eng* **7**, 163–196 (2016).

11. Kurt, E. & Bukusoglu, E. Liquid crystal microcapillary-based sensors for affordable analytical applications. *Soft Matter* **18**, 4009–4016 (2022).

12. Şengül, S., Aydoğan, N. & Bukusoglu, E. Nanoparticle adsorption induced configurations of nematic liquid crystal droplets. *J Colloid Interface Sci* **608**, 2310–2320 (2022).

13. Batir, O., Bat, E. & Bukusoglu, E. Strain-enhanced sensitivity of polymeric sensors templated from cholesteric liquid crystals. *Soft Matter* **16**, 6794–6802 (2020).

14. Avşar, D. I. & Bukusoglu, E. Chameleon skin-inspired polymeric particles for the detection of toluene vapor. *Soft Matter* **16**, 8683–8691 (2020).

15. Jacobs, S. D. *et al.* Liquid-crystal laser optics: design, fabrication, and performance. *J. Opt. Soc. Am. B* **5**, 1962–1979 (1988).

16. Maune, B. *et al.* Liquid-crystal electric tuning of a photonic crystal laser. *Appl Phys Lett* **85**, 360–362 (2004).

17. Muševič, I. Integrated and topological liquid crystal photonics. *Liq Cryst* **41**, 418–429 (2014).

18. Poulin, P., Stark, H., Lubensky, T. C. & Weitz, D. A. Novel colloidal interactions in anisotropic fluids. *Science (1979)* **275**, 1770–1773 (1997).

19. Lin, I. H., Koenig, G. M., de Pablo, J. J. & Abbott, N. L. Ordering of solid microparticles at liquid crystal-water interfaces. *Journal of Physical Chemistry B* **112**, 16552–16558 (2008).

20. Koenig, G. M., De Pablo, J. J. & Abbott, N. L. Characterization of the reversible interaction of pairs of nanoparticles dispersed in nematic liquid crystals. *Langmuir* **25**, 13318–13321 (2009).

21. Lin, I. H. *et al.* Endotoxin-induced structural transformations in liquid crystalline droplets. *Science (1979)* **332**, 1297–1300 (2011).

22. Muševič, I., Škarabot, M., Tkalec, U., Ravnik, M. & Žumer, S. Two-dimensional nematic colloidal crystals self-assembled by topological defects. *Science (1979)* **313**, 954–958 (2006).

23. Wang, X., Miller, D. S., Bukusoglu, E., De Pablo, J. J. & Abbott, N. L. Topological defects in liquid crystals as templates for molecular self-assembly. *Nat Mater* **15**, 106–112 (2016).

24. Hijnen, N., Wood, T. A., Wilson, D. & Clegg, P. S. Self-organization of particles with planar surface anchoring in a cholesteric liquid crystal. *Langmuir* **26**, 13502–13510 (2010).

25. Lintuvuori, J. S. *et al.* Colloidal Templating at a Cholesteric-Oil Interface: Assembly Guided by an Array of Disclination Lines. *Phys Rev Lett* **110**, 187801 (2013).

26. Pawsey, A. C. *et al.* Colloidal particles at the interface between an isotropic liquid and a chiral liquid crystal. *Soft Matter* **8**, 8422–8428 (2012).

27. Li, X. *et al.* Directed Self-Assembly of Colloidal Particles onto Nematic Liquid Crystalline Defects Engineered by Chemically Patterned Surfaces. *ACS Nano* **11**, 6492–6501 (2017).

28. Jeridi, H. *et al.* Unique orientation of 1D and 2D nanoparticle assemblies confined in smectic topological defects. *Soft Matter* **18**, 4792–4802 (2022).

29. Lockwood, N. A., Gupta, J. K. & Abbott, N. L. Self-assembly of amphiphiles, polymers and proteins at interfaces between thermotropic liquid crystals and aqueous phases. *Surface Science Reports* vol. 63 255–293 Preprint at https://doi.org/10.1016/j.surfrep.2008.02.002 (2008).

30. Gharbi, I. *et al.* Liquid Crystal Films as Active Substrates for Nanoparticle Control. *ACS Appl Nano Mater* **4**, 6700–6708 (2021).

31. Rahimi, M. *et al.* Nanoparticle self-assembly at the interface of liquid crystal droplets. *Proc Natl Acad Sci U S A* **112**, 5297–302 (2015).

32. Seč, D., Porenta, T., Ravnik, M. & Žumer, S. Geometrical frustration of chiral ordering in cholesteric droplets. *Soft Matter* **8**, 11982–11988 (2012).

33. Zhou, Y. *et al.* Structural Transitions in Cholesteric Liquid Crystal Droplets. *ACS Nano* **10**, 6484–6490 (2016).

34. Bukusoglu, E. *et al.* Positioning colloids at the surfaces of cholesteric liquid crystal droplets. *Soft Matter* **12**, 8781–8789 (2016).

35. Bouligand, Y., Livolant, F., The, F. L. & Physique, J. de. The organization of cholesteric spherulites. *Journal de Physique* **45**, 1899–1923 (1984).

36. Seč, D., Čopar, S. & Žumer, S. Topological zoo of free-standing knots in confined chiral nematic fluids. *Nat Commun* **5**, 3057 (2014).

37. Posnjak, G., Čopar, S. & Muševič, I. Hidden topological constellations and polyvalent charges in chiral nematic droplets. *Nat Commun* **8**, 14594–14603 (2017).

38. Posnjak, G., Čopar, S. & Muševič, I. Points, skyrmions and torons in chiral nematic droplets. *Sci Rep* **6**, 26361–27370 (2016).

39. Orlova, T., Aßhoff, S. J., Yamaguchi, T., Katsonis, N. & Brasselet, E. Creation and manipulation of topological states in chiral nematic microspheres. *Nat Commun* **6**, 7603 (2015).

40. Gardymova, A. P., Krakhalev, M. N. & Zyryanov, V. Y. Optical textures and orientational structures in cholesteric droplets with conical boundary conditions. *Molecules* **25**, 31–33 (2020).

41. Krakhalev, M. N. *et al.* Orientational structures in cholesteric droplets with homeotropic surface anchoring. *Soft Matter* **15**, 5554–5561 (2019).

42. Krakhalev, M. N., Gardymova, A. P., Emel'yanenko, A. v., Liu, J. H. & Zyryanov, V. Y. Untwisting of the helical structure of cholesteric droplets with homeotropic surface anchoring. *JETP Lett* **105**, 51–54 (2017).

43. Tran, L. & Bishop, K. J. M. Swelling Cholesteric Liquid Crystal Shells to Direct the Assembly of Particles at the Interface. *ACS Nano* **14**, 5459–5467 (2020).

44. Tran, L. *et al.* Shaping nanoparticle fingerprints at the interface of cholesteric droplets. *Sci Adv* **4**, 8597 (2018).

45. Bitar, R., Agez, G. & Mitov, M. Cholesteric liquid crystal self-organization of gold nanoparticles. *Soft Matter* **7**, 8198–8206 (2011).

46. Moreno-Razo, J. A., Sambriski, E. J., Abbott, N. L., Hernández-Ortiz, J. P. & de Pablo, J. J. Liquid-crystal-mediated self-assembly at nanodroplet interfaces. *Nature* **485**, 86–89 (2012).

47. Wang, X. *et al.* Synthesis of Optically Complex, Porous, and Anisometric Polymeric Microparticles by Templating from Liquid Crystalline Droplets. *Adv Funct Mater* **26**, 7343–7351 (2016).

48. Koenig, G. M., Lin, I. H. & Abbott, N. L. Chemoresponsive assemblies of microparticles at liquid crystalline interfaces. *Proc Natl Acad Sci U S A* **107**, 3998–4003 (2010).

49. Loudet, J.-C., Barois, P. & Poulin, P. Colloidal ordering from phase separation in a liquid-crystalline continuous phase. *Nature* **407**, 611–613 (2000).

50. Mondiot, F., Wang, X., De Pablo, J. J. & Abbott, N. L. Liquid crystal-based emulsions for synthesis of spherical and non-spherical particles with chemical patches. *J Am Chem Soc* **135**, 9972–9975 (2013).

51. Wang, X., Miller, D. S., De Pablo, J. J. & Abbott, N. L. Organized assemblies of colloids formed at the poles of micrometer-sized droplets of liquid crystal. *Soft Matter* **10**, 8821–8828 (2014).

52. Tran, L. *et al.* Change in stripes for cholesteric shells via anchoring in moderation. *Phys Rev X* **7**, (2017).

53. Stober, W., Fink, A. & Ernst Bohn, D. Controlled Growth of Monodisperse Silica Spheres in the Micron Size Range 1. *J Colloid Interface Sci* **26**, 62–69 (1968).

54. Topuz, B., Şimşek, D. & Çiftçioɨlu, M. Preparation of monodisperse silica spheres and determination of their densification behaviour. *Ceram Int* **41**, 43–52 (2015).

55. An, Y., Chen, M., Xue, Q. & Liu, W. Preparation and self-assembly of carboxylic acid-functionalized silica. *J Colloid Interface Sci* **311**, 507–513 (2007).

56. Miller, D. S., Wang, X. & Abbott, N. L. Design of functional materials based on liquid crystalline droplets. *Chemistry of Materials* **26**, 496–506 (2014).

57. Yoshioka, J. & Araoka, F. Topology-dependent self-structure mediation and efficient energy conversion in heat-flux-driven rotors of cholesteric droplets. *Nat Commun* **9**, 432 (2018).

58. Wang, X., Bukusoglu, E. & Abbott, N. L. A practical guide to the preparation of liquid crystal-templated microparticles. *Chemistry of Materials* **29**, 53–61 (2017).

59. Smalyukh, I. I. *et al.* Ordered droplet structures at the liquid crystal surface and elastic-capillary colloidal interactions. *Phys Rev Lett* **93**, 117801 (2004).

60. Smalyukh, I. I., Lavrentovich, O. D., Kuzmin, A. N., Kachynski, A. v. & Prasad, P. N. Elasticity-mediated self-organization and colloidal interactions of solid spheres with tangential anchoring in a nematic liquid crystal. *Phys Rev Lett* **95**, (2005).

61. Xu, F., Kitzerow, H.-S. & Crooker, P. P. Director configurations of nematic-liquid-crystal droplets: Negative dielectric anisotropy and parallel surface anchoring. *Phys Rev E* **49**, 3061–3068 (1994).

62. Škarabot, M., Ryzhkova, A. v. & Muševič, I. Interactions of single nanoparticles in nematic liquid crystal. *J Mol Liq* **267**, 384–389 (2018).

63. Baudry, J., Pirkl, S. & Oswald, P. Topological properties of singular fingers in frustrated cholesteric liquid crystals. *Phys Rev E* **57**, 3038–3049 (1998).

64. Oswald, P., Baudry, J. & Pirkl, S. Static and dynamic properties of cholesteric fingers in electric field. *Physics Report* vol. 337 67–96 Preprint at https://doi.org/10.1016/S0370-1573(00)00056-9 (2000).

65. Durey, G. *et al.* Topological solitons, cholesteric fingers and singular defect lines in Janus liquid crystal shells. *Soft Matter* **16**, 2669–2682 (2020).

66. Schiestel, T., Brunner, H. & Tovar, G. E. M. Controlled surface functionalization of silica nanospheres by covalent conjugation reactions and preparation of high density streptavidin nanoparticles. *J Nanosci Nanotechnol* **4**, 504–511 (2004).

67. Shah, R. R. & Abbott, N. L. Using liquid crystals to image reactants and products of acid-base reactions on surfaces with micrometer resolution. *J Am Chem Soc* **121**, 11300–11310 (1999).

68. Kleman, M. & Lavrentovich, O. D. *Soft Matter Physics: An Introduction*. (Springer, 2003). doi:doi.org/10.1007/b97416.

69. Poulin, P., Cabuil, V. & Weitz, D. A. Direct Measurement of Colloidal Forces in an Anisotropic Solvent. *Phys Rev Lett* **79**, 4862–4865 (1997).

70. Israelachvili, J. N. *Intermolecular and Surface Forces*. vol. 3 (Academic Press, 2011).

71. Valmacco, V. *et al.* Dispersion forces acting between silica particles across water: Influence of nanoscale roughness. *Nanoscale Horiz* **1**, 325–330 (2016).

72. Aveyard, R. *et al.* Measurement of long-range repulsive forces between charged particles at an oil-water interface. *Phys Rev Lett* **88**, 2461021–2461024 (2002).

73. Leuniissen, M. E., Zwanikken, J., van Roji, R., Chaikin, P. M. & van Blaaderen, A. Ion partitioning at the oil–water interface as a source of tunable electrostatic effects in emulsions with colloids. *Physical Chemistry Chemical Physics* **9**, 6405–6414 (2007).

74. Carlton, R. J., Gupta, J. K., Swift, C. L. & Abbott, N. L. Influence of simple electrolytes on the orientational ordering of thermotropic liquid crystals at aqueous interfaces. *Langmuir* **28**, 31–36 (2012).

75. Carlton, R. J., Ma, C. D., Gupta, J. K. & Abbott, N. L. Influence of specific anions on the orientational ordering of thermotropic liquid crystals at aqueous interfaces. *Langmuir* **28**, 12796–12805 (2012).

76. Cao, F., Wu, J., Li, Y. & Ngai, T. Measurements of Particle-Surface Interactions in Both Equilibrium and Nonequilibrium Systems. *Langmuir* **35**, 8910–8920 (2019).

77. Prieve, D. C., Luo, F. & Lanni, F. Brownian Motion of a Hydrosol Particle in a Colloidal Force Field. *Faraday Discuss Chem Soc* **83**, 297–307 (1987).

78. Prieve, D. C. Measurement of colloidal forces with TIRM. *Adv Colloid Interface Sci* **82**, 93–125 (1999).

APPENDICES

A. Structural Glossary of the CLC Structures

Bipolar Structure:

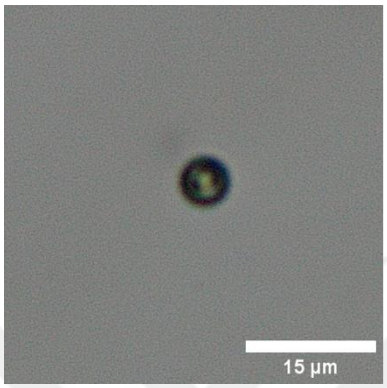

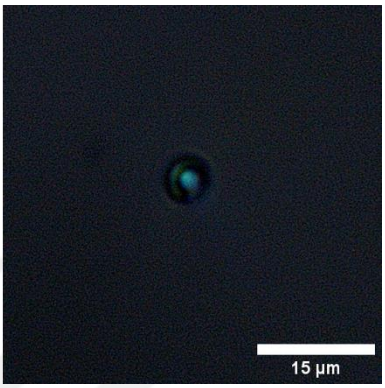

Radial Structure:

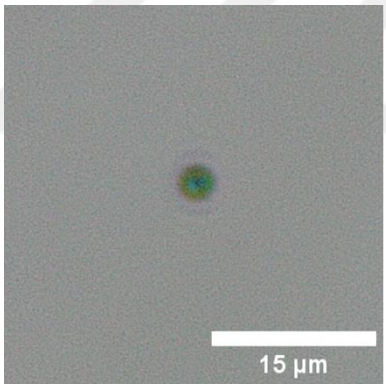

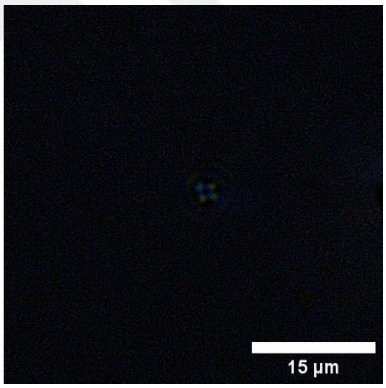

Twisted Radial Structure:

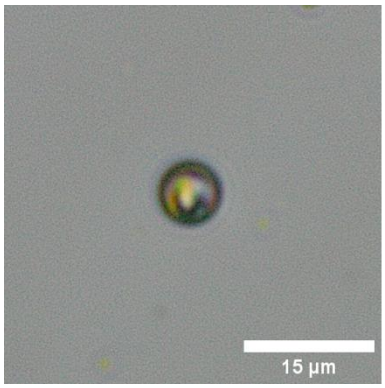

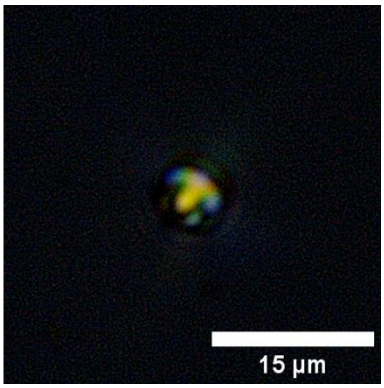

Link and Knot Structure:

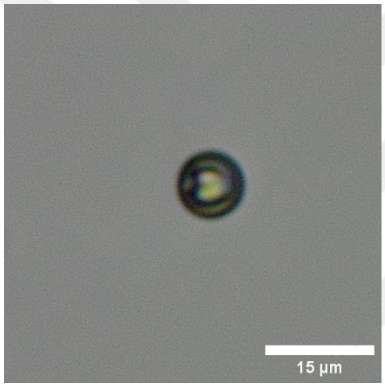

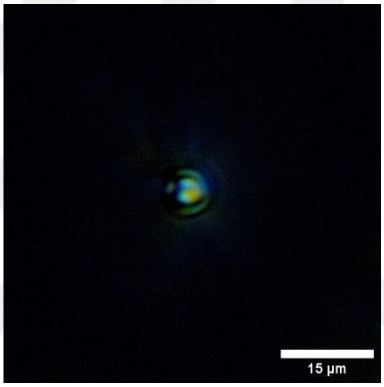

Complex Link and Knot Structure:

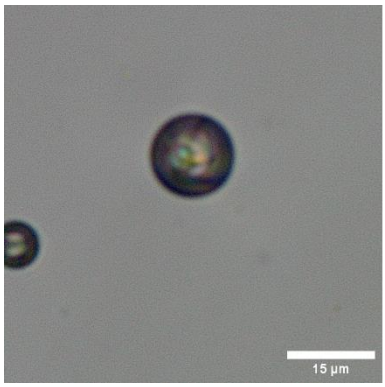

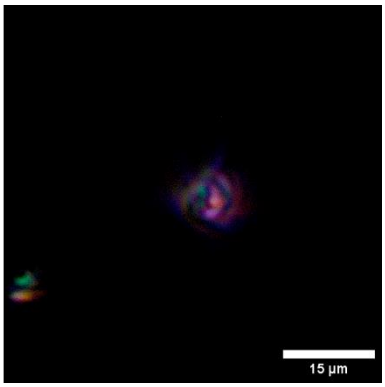

Intermediate Structure:

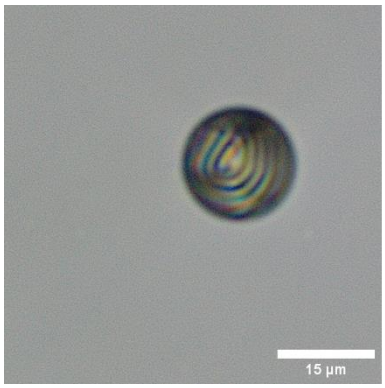

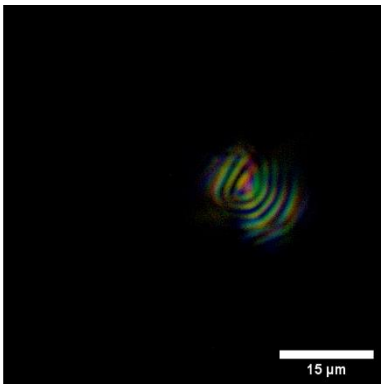

Periodic Loop Structure:

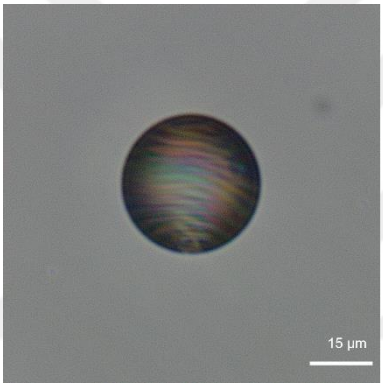

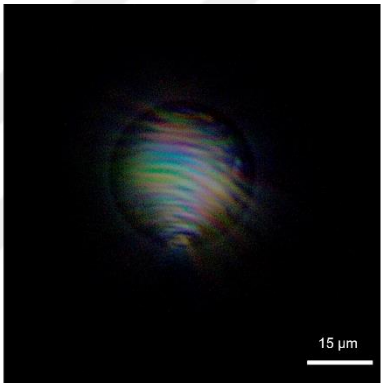

Radial Spherical Structure:

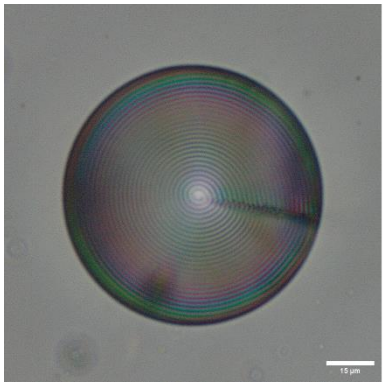

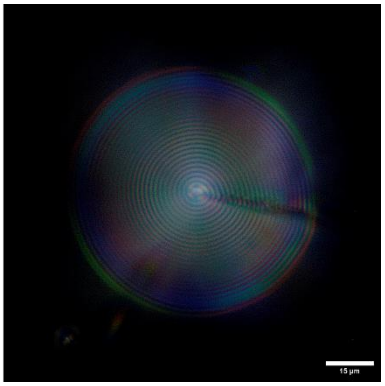

Concentric Loop Structure:

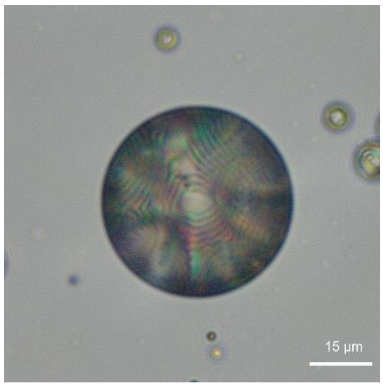

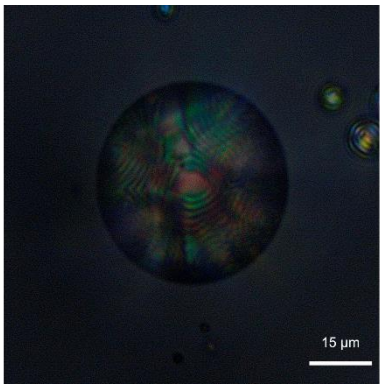

B. Effect of Medium to the Zeta Potential of Different Dispersed Phases

Dispersed Phase	Zeta Potential Continious Phase		
	1 wt% PVA	UP Water	1 mM SDS
DMOAP Silica	-10 mV	+56 mV	-65 mV
-COOH Silica	-5 mV	-32 mV	-44 mV
5CB/RM257	-11 mV	-40 mV	-61 mV

C. MATHCAD Script for Calculating Electrostatic Properties

%Constants

$k := 1.38064910^{-23}$

$\frac{J}{K}$

$T := 298.1$

K

$\varepsilon := 78$

$\varepsilon 0 := 8.8510^{-12}$

$\frac{C^2}{Jm}$

$e := 1.60217663310^{-19}$

C

$\frac{number}{(mol \cdot m)^3}$ ▮

$navg := 6.02210^{26}$

Concentration Calculations

$Salt := 0 \cdot 10^{-3}$

M

$pH := 5.$

$pOH := 14 - pH = 9$

$H := 10^{-pH} = 1 \times 10^{-5}$

M

$OH := 10^{-pOH} = 1 \times 10^{-9}$

M

$Cl := Salt + H = 1 \times 10^{-5}$

$Na := Salt = 0$

Number Density #/m^3

$\rho_1 := Cl \cdot navg \cdot 0 = 0$

$\rho_2 := H \cdot navg = 6.022 \times 10^{21}$

$\rho_3 := OH \cdot navg = 6.022 \times 10^{17}$

$\rho_4 := Na \cdot navg = 0$

$\kappa :=$

$\rho := \sum_{i=1}^{4} \rho_i = 6.023 \times 10^{21}$

Debye-Huckel Constant

m^{-1}

$$\kappa := \sqrt{\frac{e^2 \cdot \rho}{\varepsilon \cdot T \cdot k \cdot \varepsilon 0}} = 7.376 \times 10^{6}$$

$$\frac{1}{\kappa} = 1.356 \times 10^{-7}$$

m

Zeta Potential

$$\zeta := 20 \cdot 10^{-3}$$

V

Particle Radius

$$a := 50 \cdot 10^{-9}$$

m

$$\sigma := \frac{2 \cdot \varepsilon 0 \cdot \varepsilon \cdot \kappa \cdot k \cdot T}{e} \cdot \sinh\left(\frac{e \cdot \zeta}{2 \cdot k \cdot T}\right) \cdot \left(1 + \frac{1}{\kappa \cdot a} \cdot \frac{1}{\cosh\left(\frac{e \cdot \zeta}{4 \cdot k \cdot T}\right)^2}\right) = 3.771 \times 10^{-4}$$

$$\sigma - \varepsilon 0 \cdot \varepsilon \cdot \kappa \cdot x = 0 \text{ solve} \rightarrow 0.074063904298330502$$

$$\psi 0 := \frac{\sigma}{\varepsilon \cdot \varepsilon 0 \cdot \kappa} = 0.074$$

$$\psi 0 := 51.4 \cdot \operatorname{asinh}\left[\frac{\sigma}{0.117 \cdot (Cl)^{0.5}}\right] = 45.999$$

D. Energy Balances in Mediums with Different Ionic Strength

pH=2

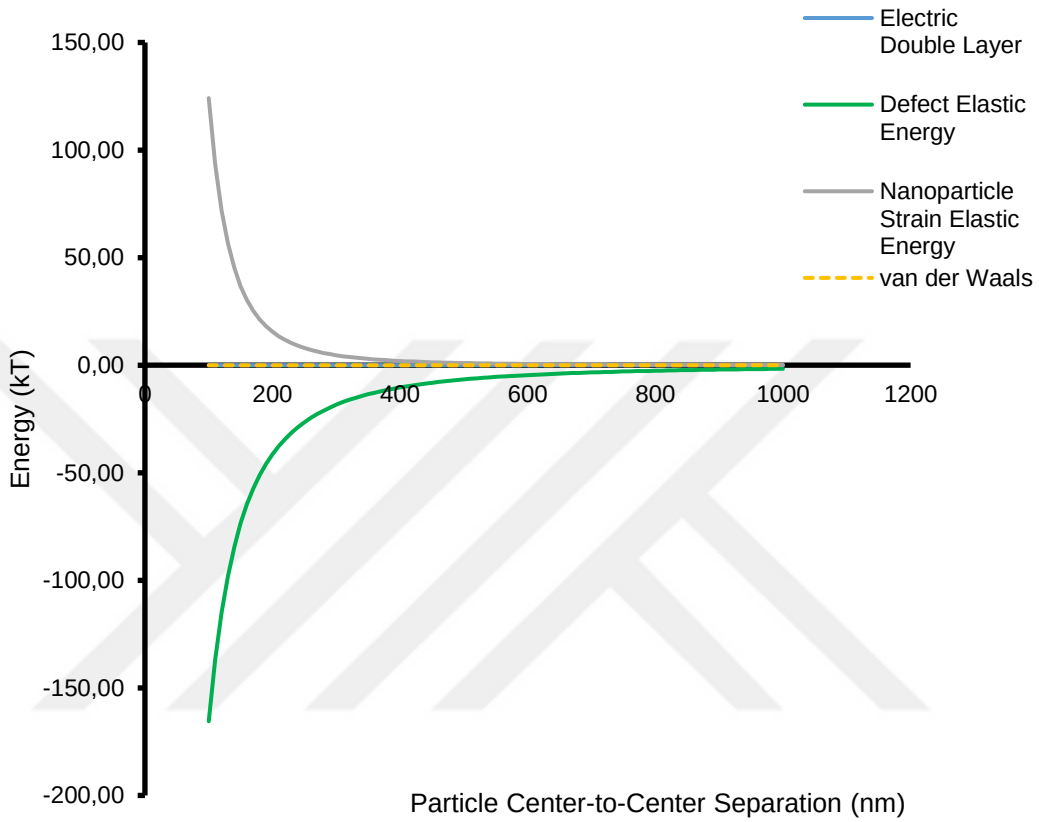

Appendix D. 1 Calculated individual contributors of the total energy indicated in Equation 1 as a function of the center-to-center separation of the particles at the interface. Calculations were performed for ~100 nm particles at pH=2

pH=3

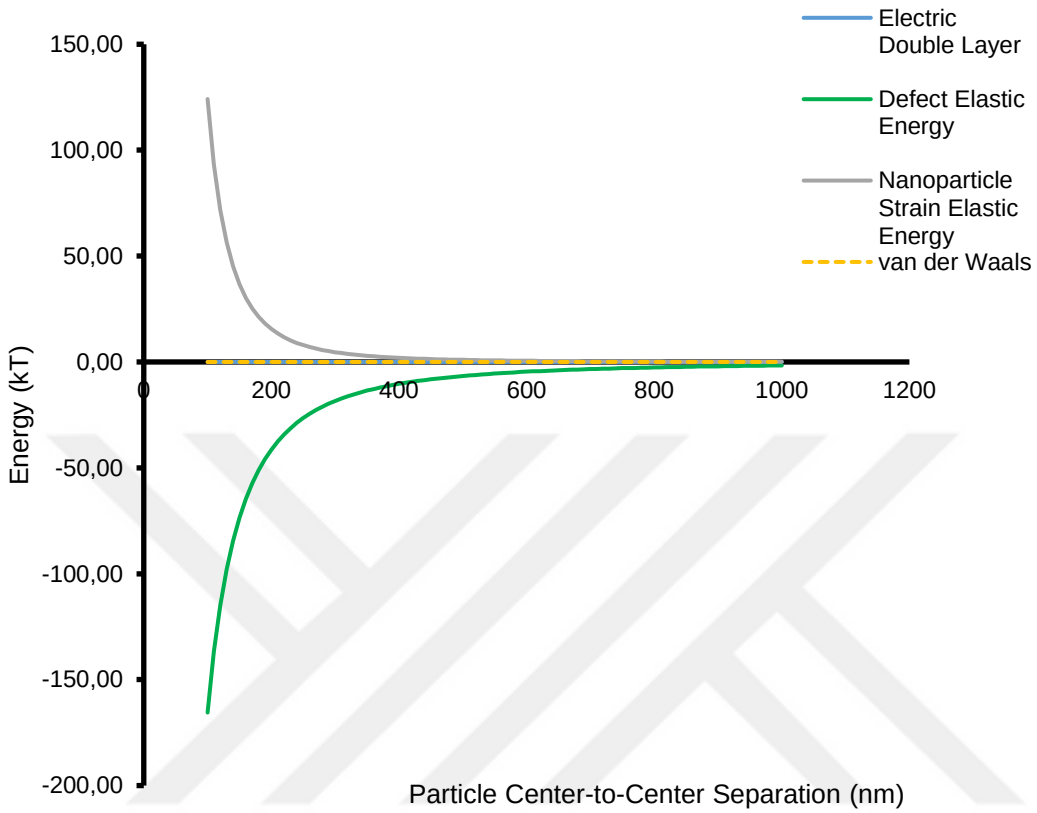

Appendix D. 2 Calculated individual contributors of the total energy indicated in Equation 1 as a function of the center-to-center separation of the particles at the interface. Calculations were performed for ~100 nm particles at pH=3

pH=4

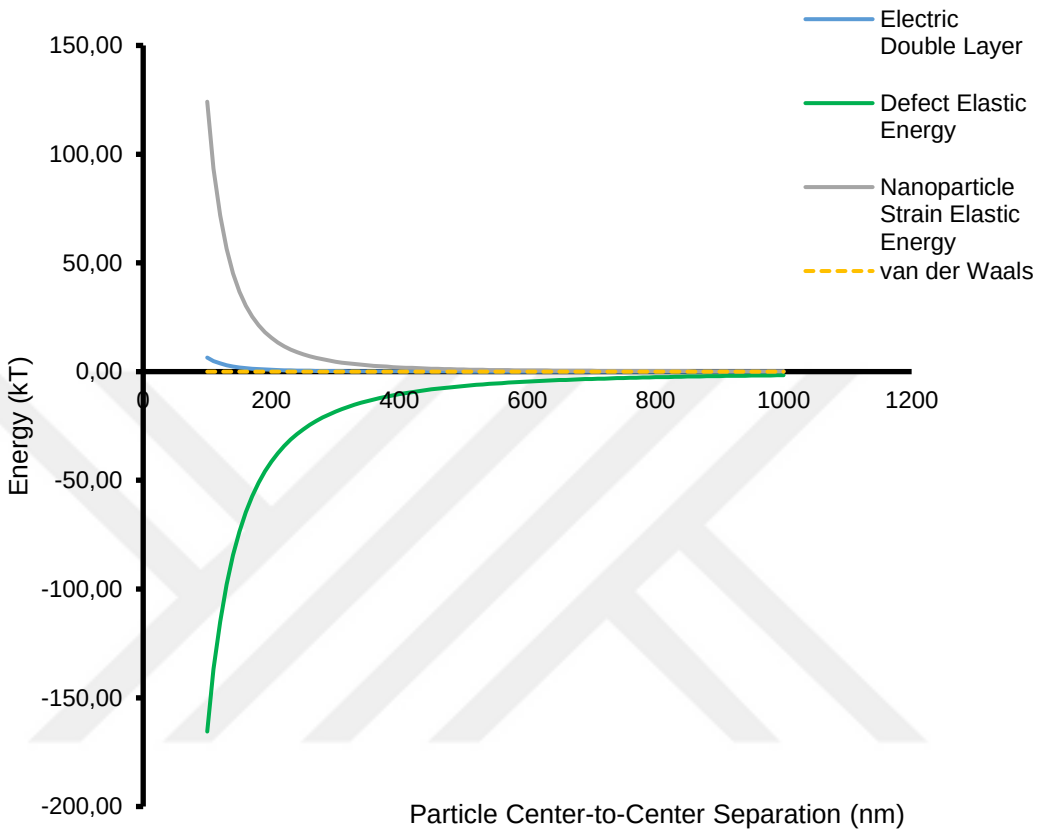

Appendix D. 3 Calculated individual contributors of the total energy indicated in Equation 1 as a function of the center-to-center separation of the particles at the interface. Calculations were performed for ~100 nm particles at pH=4

pH=6

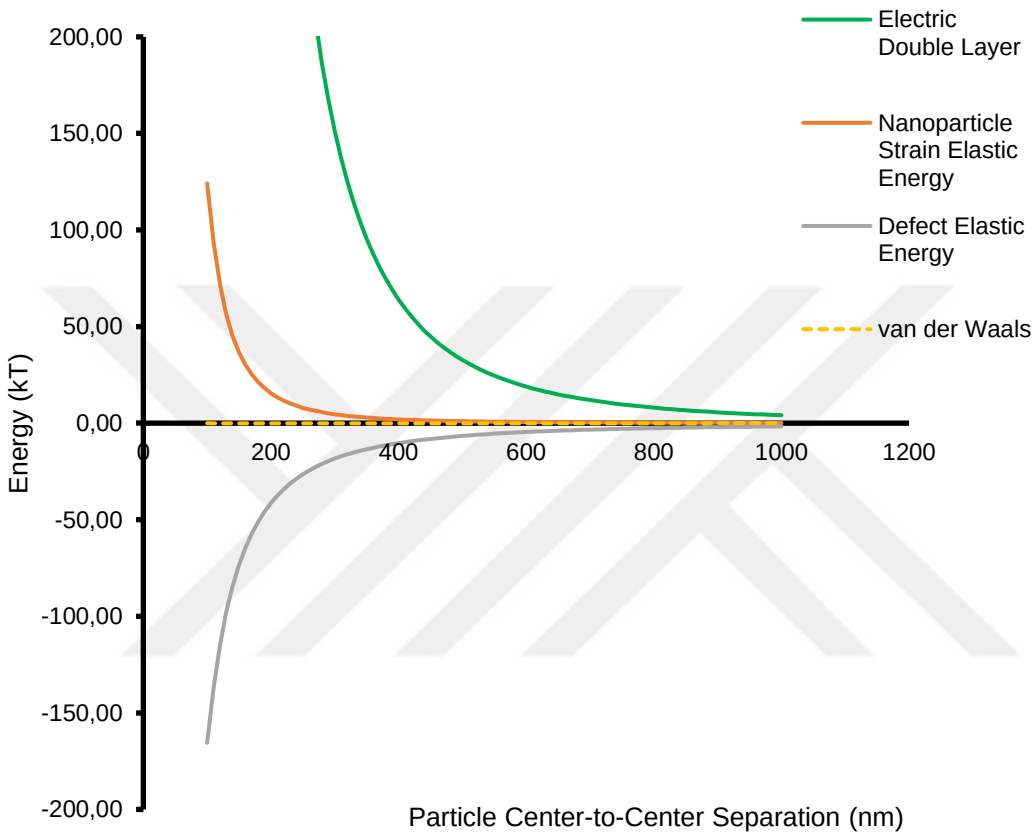

Appendix D. 4 Calculated individual contributors of the total energy indicated in Equation 1 as a function of the center-to-center separation of the particles at the interface. Calculations were performed for ~100 nm particles at pH=6